Virtual Design of Modular 3D Printed Ankle Foot Orthoses

Virtueel ontwerp van modulaire 3D-geprinte enkel-voet-orthesen

Alessio Ielapi

Promotoren: prof. dr. ir. W. Van Paepegem, dr. ir. M. De Beule
Proefschrift ingediend tot het behalen van de graad van
Doctor in de ingenieurswetenschappen: biomedische ingenieurstechnieken

Vakgroep Materialen, Textiel en Chemische Proceskunde
Voorzitter: prof. dr. P. Kiekens
Faculteit Ingenieurswetenschappen en Architectuur
Academiejaar 2018 - 2019

UNIVERSITEIT
GENT

ISBN 978-94-6355-260-8
NUR 954
Wettelijk depot: D/2019/10.500/68

Supervisors:

Prof. dr. ir. Wim Van Paepegem
Dr. ir. Matthieu De Beule

Research lab:

Institute Biomedical Technology
Biofluid, Tissue and Solid Mechanics for Medical Applications (bioMMeda)
Ghent University
Corneel Heymanslaan 10 - Blok B (entrance 36)
B–9000 Gent
BELGIUM

Members of the exam committee:

Chairman:	
Ereprof. dr. ir. Ronny Verhoeven	Faculty of Engineering and Architecture, UGent
Secretary:	
Prof. dr. ir. Malcolm Forward	Faculty of Engineering and Architecture, UGent
Reading committee:	
Prof. dr. ir. Jan Belis	Faculty of Engineering and Architecture, UGent
Prof. dr. ir. Patrick Segers	Faculty of Engineering and Architecture, UGent
Dr. ir. Michele Conti	Università degli studi di Pavia, Italy
Prof. dr. ir. Bernardo Innocenti	Université libre de Bruxelles

This research was funded by VLAIO (Flanders Innovation & Entrepreneurship) and the A_STREAM_AFO project (Applied Structural Engineering of AM Materials for Ankle Foot Orthosis; project numbers: 140164 & 140165) under the SIM (Strategic Initiative Materials in Flanders) research program STREAM (STRuctural Engineering materials through Additive Manufacturing)

Un vincitore è
un sognatore che non
si arrende mai.

A winner is
a dreamer who
never gives up.

Nelson Mandela

TABLE OF CONTENTS

II Experimental tests on AFOs 65

III Finite element analysis of AFOs 101

List of Figures

LIST OF TABLES

ABBREVIATIONS

The following list summarizes the most commonly used abbreviations in this thesis.

Abbreviations

3D	Three-dimensional
ABS	Acrylonitrate butadiene styrene
AFO	Ankle foot orthosis
ALS	Amyotrophic lateral sclerosis
AM	Additive manufacturing
C3D4	Four-node tetrahedral element
C3D8R	Eight-node brick element with reduced integration
CAD	Computer-Aided Design
CF	Carbon fibre
CFRP	Carbon fiber reinforced composite
CMT	Charcot-Marie-Tooth
CNC	Computer numerical control
CPO	Certified prosthetic orthotist
CT	Computed tomography
DL	Dorsiflexion loading
DU	Dorsiflexion unloading
EVA	Ethylene-vinyl acetate
FDM	Fused deposition modeling
FE	Finite element
ICC	Intraclass correlation coefficient
MAFO	Molded ankle foot orthosis
MDF	Medium-density fibreboard
MTP	Metatarsophalangeal
PA	Polyamide
PC	Polycarbonate
PE	Polyethylene
PL	Plantarflexion loading

PLA	Polylactic acid
PP	Polypropilene
PRF	Parallel rheological framework
PU	Plantarflexion unloading
ROM	Range of motion
S4R	Four-node shell element with reduced integration
SD	Standard deviation
SDD	Smallest detectable difference
SEM	Standard error of measurement
SLA	Stereolithography
SLS	Selective laser sintering
STL	Standard Triangulation Language
TM	Melting temperature
UV	Ultraviolet
VFP	Virtual functional prototyping process

ACKNOWLEDGEMENTS

First of all, I would like to express my sincere gratitude to my supervisors Prof. Wim Van Paepegem and Dr. Matthieu De Beule for the continuous support, patience and knowledge. Their valuable guidance helped me during the development of the research project and the writing of this dissertation. It was a big priviledge to work with them and I can say that without their contribution, the achievement of this goal would have not been possible. Besides my supervisors, I would like to thank Prof. Malcolm Forward for his insightful comments, encouragement and the clinical guidance, which allowed to widen my research from various perspectives.

I would also like to thank Miguel Vermandel and Jan Deckers, who provided me an opportunity to join the R&D team at V!GO, and the necessary guidance for the design and development of the experimental setup. I would also like to thank Nicolas Lammens for the precious advices during the development of the finite element models of the AFOs and Egle Vasiliauskaite for the realization of the post-processing code for the experimental results and the useful parameters obtained from the gait assessment on the patients. I thank all my colleagues for the stimulating discussions and for all the fun we have had in the last four years, especially with the football team.

Last but not the least, I would like to thank my parents, my brother and sister for the unconditional love and for always being there for me. A special thanks goes to my friends who have been on my side during these last few years, giving me the motivation and support to succeed on this goal.

The work developed in this thesis was funded by VLAIO (Flanders Innovation & Entrepreneurship) and the A_STREAM_AFO project (Applied Structural Engineering of AM Materials for Ankle Foot Orthosis; project numbers: 140164 & 140165) under the SIM (Strategic Initiative Materials in Flanders) research program STREAM (STRuctural Engineering materials through Additive Manufacturing).

SAMENVATTING

DEEL I - INLEIDING

Hoofdstuk 1 - 3D-geprinte enkel-voet-orthesen

Enkel-voet-orthesen (EVOs) zijn externe medische hulpmiddelen die aangebracht worden rond het enkelgewricht en zowel de voet als de kuit omvatten. EVOs worden gebruikt om een natuurlijker looppatroon te verkrijgen bij patiënten die lijden aan neurologische en/of musculoskeletale aandoeningen. Het gebruik van een EVO kan als succesvol worden beschouwd als de orthese in staat is om alle gewenste functies te bieden binnen de verwachte tijd en zonder ongemak voor de patiënt. Dit hangt sterk af van het ontwerp en de mechanische eigenschappen van de EVOs, wat betekent dat EVOs dienen aangepast te worden aan de noden van de patiënt. Het meest gebruikte productieproces voor EVOs is momenteel thermovormen, waarbij de op maat gemaakte gegoten-thermoplastische EVOs het meest voorkomen. De prestaties van EVOs hangen sterk af van de vaardigheden van de vakmannen die de ortheses meestal manueel vervaardigen, wat leidt tot een tijdrovend productieproces. Bovendien biedt dit proces geen mogelijkheid tot modificatie of evaluatie van de EVO-eigenschappen voor hun eigenlijke fysieke realisatie. Dit zou nochtans een groot potentieel voordeel kunnen zijn om de productie-efficiëntie te verhogen en de productietijd in te korten. Additieve fabricagetechnieken zouden de mogelijkheid kunnen bieden om deze aspecten te implementeren en tegelijkertijd de consistentie van vorm en functionaliteit te garanderen. Deze technologieën zijn gebaseerd op het gebruik van STL-bestanden die alle benodigde geometrische informatie bevatten om de EVOs te kunnen printen. Na enkele verfijningen kunnen deze STL-bestanden worden gebruikt voor computationele simulaties om het mechanische gedrag van de orthesen te voorspellen. Om als betrouwbaar te worden beschouwd vereisen computationele modellen een uitgebreide validatie door middel van experimentele testen op een specifiek ontworpen testopstelling voor deze toepassing.

De bovengenoemde zaken worden toegepast voor de evaluatie van de mechanische eigenschappen van de 3D-geprinte EVOs die in dit proefschrift worden geanalyseerd, zowel op experimenteel als computationeel vlak. Hoofdstuk 1 geeft een korte inleiding over deze aspecten, alsook over de anatomie van het onderste ledemaat, het looppatroon, de bijhorende pathologieën, de verschillende soorten EVOs, additieve fabricagetechnologieën en PA 12, en het materiaal dat wordt gebruikt voor het produceren van de gebruikte EVOs.

Hoofdstuk 2 - Experimentele opstellingen & computationele modellen van EVOs

Alvorens de beste strategie te bepalen voor de evaluatie van 3D-geprinte EVOs werd een literatuuronderzoek uitgevoerd om een overzicht te geven van de benaderingen door verschillende onderzoeksgroepen wereldwijd. Een totaal van 46 artikelen werd geïdentificeerd en opgedeeld in drie subcategorieën afhankelijk van de gebruikte methodes, zijnde experimenteel onderzoek, computationeel onderzoek, of allebei. Dit onderzoek bracht aan het licht hoe het gebruik van computationele methoden (gevalideerd door middel van experimentele testen) de meest efficiënte benadering vormt voor de evaluatie van deze orthopedische hulpmiddelen. Deze informatie (zie hoofdstuk 2) resulteert in een beter begrip en het verwerven van de kennis die aan de basis van dit onderzoek ligt.

DEEL II - EXPERIMENTELE TESTS OP EVOS

Hoofdstuk 3 - Ontwerp van de experimentele opstelling

De beschrijving van het ontwerp voor de opstelling van de experimentele evaluatie van de 3D geprinte EVOs wordt gegeven in hoofdstuk 3. Deze opstelling, ontwikkeld in nauwe samenwerking met het bedrijf V!GO NV (Wetteren, België), actief in orthopedische hulpmiddelen, liet toe om de enkelstijfheid van verschillende patiënt-specifieke EVOs te kwantificeren in het sagittale vlak tijdens de volcontact-fase. De belangrijkste kenmerken van de testopstelling zijn de mogelijkheid om de EVOs uit te lijnen met hun anatomische enkelgewricht over een maximale bewegingsuitslag van +/- 25 graden in dorsiflexie en plantarflexie, en om de apparaten op een niet-destructieve manier te testen. In het bijzonder werd het bewegingsbereik, gebruikt voor het testen van de EVOs in dit onderzoek, gebaseerd op eerdere ganganalyse van de patiënten, terwijl ze met hun EVOs liepen. Patiënt-specifieke MDF-blokken, die de locatie van de anatomische punten van de patiënten bevatten, werden gebruikt voor de fixatie en voor het overbrengen van de bewegingen naar de EVOs in de opstelling. Bovendien werd de betrouwbaarheid van de opstelling zelf geëvalueerd: de herhaalbaarheid van de test alsook de intra-tester en inter-tester variabiliteit toonde aan hoe de setup toepasbaar is voor de kwantificering van de enkelstijfheid van 3D-geprinte EVOs , alsook uitbreidbaar naar de evaluatie van andere typologieën van EVOs. Verder werd de validiteit van de opstelling ook bewezen door de resultaten ervan te vergelijken met het testen van de buigstijfheid van een inox-staalplaat d.m.v. een tweede experimentele testmachine. Andere relevante parameters werden ook onderzocht, zoals de nauwkeurigheid tussen cycli en de hersteltijd tussen opeenvolgende tests.

DEEL III - EINDIGE ELEMENTENMODELLEN VAN EVOS

Hoofdstuk 4 - Realisatie van de computermodellen

Hoofdstuk 4 beschrijft uitgebreid de strategie voor het maken van verschillende patiënt-specifieke computermodellen van EVOs, die gebruikt werden voor de voorspelling van hun enkelstijfheid en spanningsverdeling in het sagittale vlak tijdens de volcontact-fase. Zoals geanticipeerd vormen de STL-bestanden voor het 3D printen van de ortheses – na enkele manipulaties – de basis voor de computermodellen. Hiertoe werd een algoritme ontworpen in het open-sourceprogramma pyformex voor het berekenen van verschillende meshes van de orthesen. Een mesh-sensitiviteitsstudie a.d.h.v. verscheidene EVO-meshes, gemaakt van verschillende element-types (hexahedrische versus quadrilaterale volume-elementen) en met verschillende meshdensiteiten van het rooster, liet toe om het meest geschikte meshtype te identificeren voor de analyses. De computationele analyse vereiste ook het gebruik van een geavanceerd materiaalmodel, nl. het parallel-reologisch-framework (PRF)-model, dat de statische analyse van het orthesegedrag mogelijk maakte door de visco-elasto-plastische eigenschappen te beschrijven. De parameters voor het model werden verkregen uit een eerdere experimentele analyse op monsters van PA 12, gebruikt om de EVOs te vervaardigen. De rand- en belastingsvoorwaarden van de EVOs werden bepaald a.d.h.v. de experimentele tests beschreven in hoofdstuk 3. Er werden meerbepaald drie verschillende methodologieën gebruikt voor het beschrijven van de randvoorwaarden om zo de meest efficiënte procedure te identificeren voor de kwantificatie van de EVO-eigenschappen. De eerste benadering vereiste de totale fixatie van de geometrie van de EVOs tot op de hoogte van de MDF-blokken gebruikt in de experimentele opstelling. De tweede benadering vereiste enkel de totale fixatie van de EVO-zool en het contact van de EVO met de virtuele representatie van de MDF-blokken. De derde benadering hanteerde dezelfde randvoorwaarden als de tweede benadering, maar zonder de virtuele representatie van de MDF-blokken. Het onderzoek naar de spanningsdistributie op de EVOs liet ook toe om de meest kritieke onderdelen van de EVOs en de verschillen tussen de verschillende benaderingen te identificeren.

DEEL IV - CONCLUSIES EN TOEKOMSTIGE WERK

Hoofdstuk 5 - Conclusies en toekomstige werk

Het laatste hoofdstuk 5 van dit proefschrift bevat de algemene conclusies van deze scriptie. Daarnaast rapporteert het de belangrijkste resultaten en stelt het nieuwe strategieën voor die kunnen geïmplementeerd worden in de toekomst. Dit doctoraatsproject stelt een numeriek kader voor waarbij experimentele en computationele methoden gebruikt werden om het mechanisch gedrag van verschillende patiënt-specifieke 3D-geprinte EVO's te evalueren in het sagittale vlak tijdens de vol contact-fase. De experimentele methode vereiste het opzetten van een semi-geautomatiseerde experimentele opstelling voor het bepalen van de stijfheid van 3D-geprinte apparaten rond een as die uitgelijnd is met het enkelgewricht terwijl patiënt-specifieke bewegingen beschouwd werden. De locatie van het anatomische enkelgewricht en de verschillende bereiken van bewegingen werden rechtstreeks verkregen op basis van de ganganalyse van de patiënten. De experimentele grens en belastingscondities werden vervolgens nagebootst in de simulaties waarbij verschillende patiënt-specifieke eindige elementenmodellen gevalideerd werden. Dit onderzoek heeft bijgedragen tot een algemeen beter begrip van het mechanisch gedrag van 3D-geprinte EVO's. Bovendien levert het bijkomende informatie en middelen voor de toekomstige ontwikkeling van 3D-geprinte EVO's zodat het productieproces en de klinische toepassing kan verbeterd worden. De resultaten van het voorgestelde numeriek kader kunnen in de toekomst gebruikt worden in combinatie met optimalisatie-algoritmen om het ontwerp van 3D-geprinte EVO's te verbeteren en effectievere 3D-geprinte EVO's te realiseren. De resultaten van dit onderzoek kunnen eveneens dienen om de impact van andere pathologische aandoeningen te bestuderen.

SUMMARY

PART I - INTRODUCTION

Chapter 1 - 3D printed ankle foot orthoses (AFOs)

Ankle foot orthoses (AFOs) are external medical devices, applied around the ankle joint and encompassing the foot and the calf, used to restore and provide a more natural gait pattern to patients, which can be affected by neurological and/or musculoskeletal disorders. The application of an AFO can be considered successful if it is able to provide all the desired functions for the expected amount of time, without causing discomfort to the patients. This is directly depending on the design and the mechanical properties of the AFOs, which need to be customized with respect to the benefits required by each individual patient. Currently, the most used manufacturing process for AFOs is thermoforming with custom molded-thermoplastic AFOs being the most employed. Because of this production process, their performance directly depends on the skills of the craftsmen who manufacture the devices, in a process which is mostly manual and time consuming. In addition, this process does not allow modifications of the AFO properties or their evaluation before their physical realization, which could be a huge advantage in order to increase the production efficiency and minimize the timeline. Therefore, additive manufacturing technologies could provide the means for implementing all these aspects, guaranteeing at the same time consistency of shape and functionality. These technologies are based on the use of STL files which contain all the geometric information of the devices to be printed; after some refinements, they can be used for computational simulations in order to predict the mechanical behavior of the AFOs. To be considered reliable, computational models require further validation through dedicated experimental tests, i.e. carried out from specifically designed test rigs.

All these features are applied for the evaluation of the mechanical properties of the 3D printed AFOs analyzed in this dissertation both from an experimental and from a computational point of view. Chapter 1 provides a brief introduction on these aspects, including further information on the anatomy of the lower limb, the gait and related pathologies, different types of AFOs, additive manufacturing technologies and PA 12, the material used for fabricating the used AFOs.

Chapter 2 - Experimental setups & Computational models of AFOs

Before deciding upon the best strategy to adopt for the evaluation of the 3D printed AFOs, a literature study was performed for understanding which were the approaches employed by other research groups worldwide. A total of 46 articles was identified and divided into three sub-categories whether they used experimental, computational or a combination of both methods. This investigation highlighted how the use of computational methods, which were validated through experimental tests, represent the most efficient approach for the evaluation of these orthopedic devices. This information, included in Chapter 2, will provide the means for better understanding and acquiring the knowledge at the basis of this research.

PART II - EXPERIMENTAL TESTS ON AFOs

Chapter 3 - Design of the experimental setup

The description of the design of the setup used for the experimental evaluation of the 3D printed AFOs is provided in Chapter 3. This setup, developed in close collaboration with the orthopedic device company V!GO NV (Wetteren, Belgium), allowed the quantification of the ankle stiffness of several patient-specific AFOs in the sagittal plane during the stance phase of gait. The main features of the test rig are the possibility of aligning the AFOs to their anatomical ankle joint over a maximum range of motion of +/- 25 degrees in dorsiflexion and plantarflexion and to test the devices in a non-destructive way. In particular, the ranges of motion used for testing the AFOs in this study were acquired from a previous gait assessment of the patients, while they walked with their AFOs. Patient-specific medium-density fibreboard (MDF) blocks, containing the location of the anatomical points of the patients, were used for the fixation and for providing the movements to the AFOs in the setup. Moreover, the reliability of the setup was evaluated: the test-retest repeatability, the intra-tester and inter-tester variability showed how the setup is applicable for the quantification of the ankle stiffness of the 3D printed AFOs and extendable to the evaluation of any topology of AFOs. In addition, the validity of the setup was further proven by comparing its outcomes, when testing the bending stiffness of an inox steel sheet, with a second experimental testing machine. Other parameters are also investigated such as the accuracy between cycles and the recovery time between subsequent tests.

Part III - Finite element analysis of AFOs

Chapter 4 - Realization of the computational models

Chapter 4 extensively describes the strategy used for the development of several patient-specific finite element models of the AFOs, which were used for the prediction of their ankle stiffness and stress distribution in the sagittal plane during the stance phase of gait. As previously anticipated, the starting point is represented by the STL files of the devices used for 3D printing, which undergo some refinements before being usable. For this purpose, a dedicated algorithm was created in the open-source program pyFormex, which allowed to create several meshes of the devices. After performing a mesh sensitivity analysis by using AFO meshes made of different elements (3D solid vs. 3D shell) or with a different density of the elements in the grid, it was possible to identify the suitable mesh type and number to be employed in the analysis. The computational analysis also required the utilization of an advanced material model called as parallel rheological framework (PRF) model, which allowed the static analysis of the behavior of the devices, by describing the visco-elasto-plastic properties of the 3D printable material used to manufacture the AFOs (PA 12). The parameters of the model were obtained from a previous experimental analysis on samples of PA 12. The boundary and loading conditions were applied on the AFOs according to the experimental tests described in Chapter 3. In particular, three different methodologies were identified for expressing the boundary conditions in order to find the most efficient procedure for obtaining a quantification of the AFO properties and validate them: the first approach required the total fixation of the geometry of the AFOs till the height of the MDF blocks used within the experimental setup, the second approach only required the total fixation of the AFO sole and the contact between the AFO and the virtual representation of the MDF blocks while the third approach required the same boundary conditions of the second approach, but without including the virtual representation of the MDF blocks. The investigation of the stress acting on the AFOs also allowed to identify the most critical parts on the AFOs and the differences between the different approaches.

Part IV - Conclusions and future work

Chapter 5 - Conclusions and future work

The final chapter 5 of this dissertation includes the general conclusions of this thesis, reporting the main achievements, limitations and proposing new strategies to be implemented in the future.

In particular, this PhD project presented the creation of a numerical framework where the combination of experimental and computational methods

allowed the evaluation of the mechanical behavior of several patient-specific 3D printed AFOs in the sagittal plane during the stance phase of gait. The experimental methods required the construction of a semi-automated experimental setup, which enabled the quantification of the stiffness of the 3D printed devices around an axis aligned to the anatomical ankle joint over a patient-specific range of motion; the location of the anatomical ankle joint and the different ranges of motion were directly acquired from the gait assessment of the patients. The experimental boundary and loading conditions were then mimicked in the computational environment where the different patient-specific finite element models were validated.

The research presented in this thesis has contributed to increase the general understanding of the mechanical behavior of the 3D printed AFOs and to provide more information to allow their future development and improve their manufacturing process and clinical application. In particular, the outcomes obtained from this numerical framework have the potential to be used in combination with optimization algorithms in order to ameliorate the design and realization of more effective 3D printed AFOs and be extended to study the impact of other pathologic conditions.

I

Introduction

Chapters

CHAPTER 1

3D PRINTED ANKLE FOOT ORTHOSES (AFOs)

This chapter gives a general introduction on the application of ankle foot orthoses (AFOs), starting from a brief description of the anatomy of the lower limbs with a particular focus on the ankle joint complex, the gait cycle and related disabilities in section 1.1 to 1.4. Section 1.5 describes the different types of AFOs, while section 1.6 introduces the main concepts of additive manufacturing technologies, together with the description of the 3D printable material used for the realization of the AFOs described in this dissertation. The context and the objectives of this PhD are respectively described in sections 1.7 and 1.8, while an overview of the dissertation is provided in section 1.9.

1.1 ANATOMICAL PLANES

When describing the movement of a human body in space, it is important to use a specific anatomical terminology. In Figure 1, the anatomical planes that will be used throughout the chapters of this thesis to describe specific movements or landmarks of the human body are depicted. As we can see, there are three commonly used anatomical planes: the sagittal plane, dividing the body in a left and a right part, the coronal (or frontal) plane, dividing the body in an anterior and posterior part and the transverse (or horizontal) plane, dividing the body in a superior and inferior part.

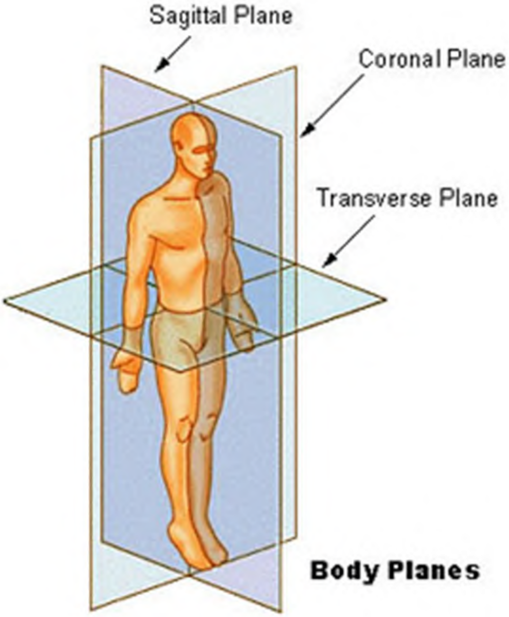

Figure 1.1: Anatomical planes (adapted from:https://www.quinticsports.com).

1.2 Anatomy of the lower limbs

The lower limb consists of three regions: the thigh, the leg and the foot (figure 1.2). The thigh is the region located between the hip and the knee joints and contains a single bone called femur (figure 1.3 a-b), which is the longest bone of the body. The proximal end is called head of the femur and it is connected with the coxal bone to form the hip joint. The medial side of the femoral head contains a minor indentation, which serves as site of attachment for the ligament of the head of the femur and one of its main functions is to carry an important artery that supplies it.

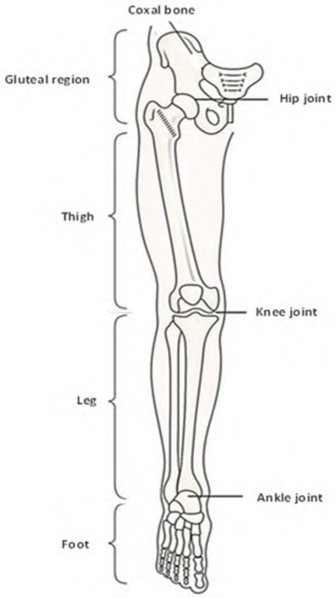

Figure 1.2: Anterior view of the gluteal region and the right lower limb, which is divided in three regions: the thigh, located between the hip and the knee joints, the leg, located between the knee and the ankle joints and the foot, located distally to the ankle joint (adapted from: https://www.earthslab.com).

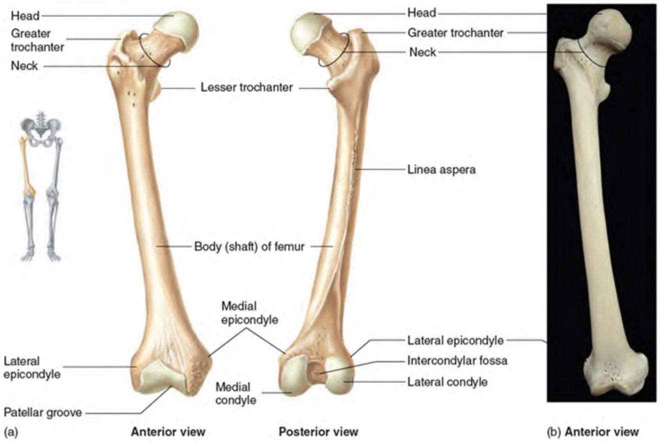

Figure 1.3: Right femur (a) and anterior view of the right femur (b) (adapted from [1]).

The neck of the femur is the narrowed region below the head and joins the shaft with an angle of about 125 degrees. The trochanters are zones for tendons attachment which originate at the junction of the neck to the shaft:

the greater trochanter is located above the base of the neck and provides additional leverage to the muscles that act across the hip joint. The lesser trochanter, instead, lies on the medial aspect of the femur, just below the neck. The shaft of the femur has a slight anterior curvature, while posteriorly it has the gluteal tuberosity, a roughened area extending from the greater trochanter. More inferiorly, the gluteal tuberosity becomes continuous with the linea aspera, a zone along which the tendons of multiple muscles of the hip and thigh regions attach to the femur. At the distal end of the femur, the medial and lateral condyles articulate with the tibia to form the knee joint. The epicondyles, located medially and laterally to the condyles, provide attachment for tendons and support the ligaments of the knee. Posteriorly, the intercondylar fossa separates the medial and lateral condyles while anteriorly, the condyles join together to form the throclear groove, which provides for articulation with the patella. The patella, also known as kneecap, is a large sesamoid bone located within the tendon of the quadriceps femoris, a group of anterior thigh muscles that allows the movement of the knee. The patella articulates with the throclear groove of the distal anterior femur forming the patella-femoral joint, which main purpose is to serve as a mechanical pulley for the quadriceps muscles as the patella changes the direction of the extension force throughout knee range of motion ([2]). It also prevents excessive friction between the muscle tendon and the distal femur.
The leg, in the human anatomy, is the region between the knee and the ankle joints and contains two bones: the tibia and the fibula (figure 1.4).

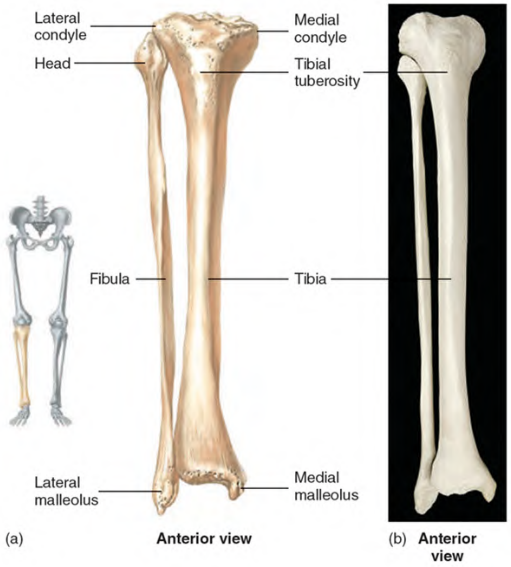

Figure 1.4: Anterior views of the right tibia and fibula (adapted from [1]).

The tibia is the large medial bone of the leg: the anterior surface of the tibia presents an irregular area called tibial tuberosity, where the tendons of the anterior thigh muscles are attached and that can be easily felt through the skin. As it approaches the ankle joint, the tibia widens and we can find the medial malleolus, which provides medial support for the ankle joint. Parallel to the lateral border of the tibia, there is the fibula, whose head articulates with the lateral tibial condyle. It mainly serves as a site for the attachment of the muscles tendons and the ligaments that regulate the movements of the foot. The distal end of the fibula extends to the ankle joint through the lateral malleolus, which provides lateral stability to the ankle. The posterior half of the foot (figure 1.5) consists of seven tarsal bones: the talus, the calcaneus, the cuboid, the navicular and the medial, intermediate and lateral cuneiforms.

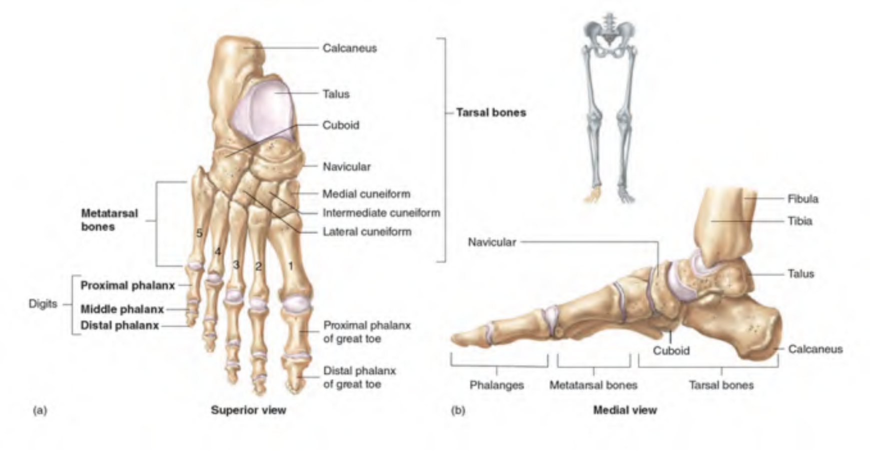

Figure 1.5: Superior (a) and medial (b) views of the right foot (adapted from [1]).

The talus articulates with the tibia and the fibula to form the ankle joint and transmits the weight of the body from the tibia towards the toes. Inferiorly the talus is connected to the calcaneus, the largest of the tarsal bones, which form the heel. The posterior part of the calcaneus serves as attachment site for the Achilles tendon, which arises at strong calf muscles. The anterior surface of the calcaneus articulates with the cuboid bone, while the anterior talus articulates with the navicular bone, which is connected to the three cuneiform bones. The distal surfaces of the cuboid bones articulate with the metatarsal bones, which form the anterior half of the foot. The metatarsal bones are numbered 1–5, starting from the medial side of the foot. Proximally, the first till the third metatarsal bones articulate with the cuneiform bones, while the other two articulate with the cuboid bone. Distally, each metatarsal bone articulates with a different proximal phalanx. The hallux, or great toe, has two phalanges (proximal and distal), while the other toes have three phalanges (proximal, middle and distal).

1.2.1 The ankle joint complex

The ankle joint, also called talocrural or tibiotalar joint is part of a complex together with the subtalar (talocalcaneal) and the transversal-tarsal (Chopart) joints ([3],[4],[5]). It is formed by the surfaces of the tibial and fibular distal epiphysis and the superior, lateral and medial aspects of the talus. In particular, the talus is firmly held in position by the lateral malleolus of the fibula and the medial malleolus of the tibia, which form a mortise for receiving the talus (figure 1.6 a-b). This connection is a complex triplanar synovial joint, with two axes of motion that allow for the movements of the foot in the space, as shown in figure 1.7,figure 1.8 ([6]).

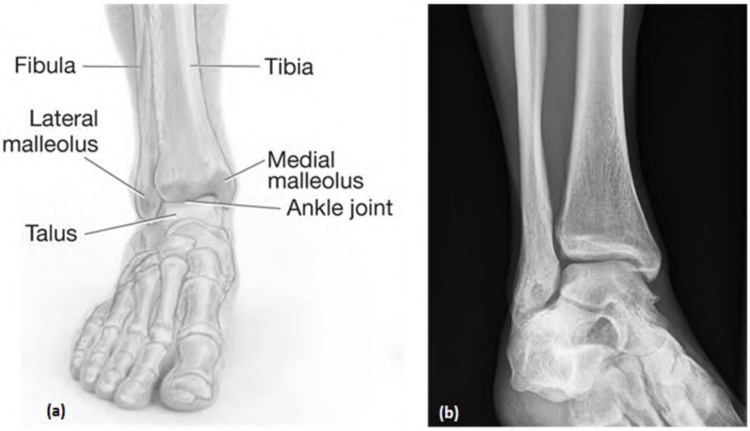

Figure 1.6: Anterior (a) view and radiography (b) of the ankle joint complex (adapted from: http://www.alphaanklearthroplasty.com).

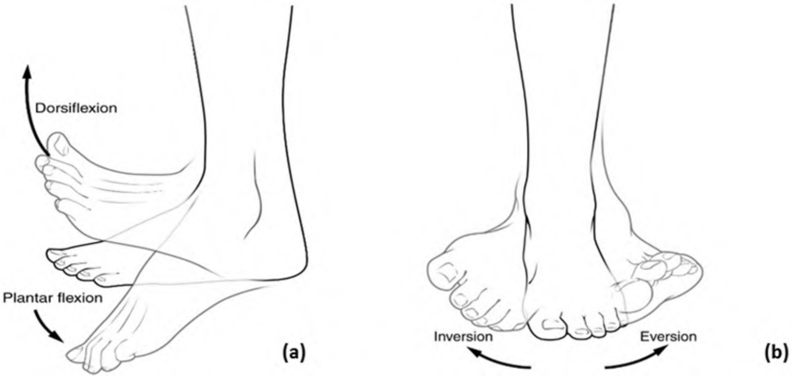

Figure 1.7: (a) Dorsiflexion and plantarflexion of the foot in the sagittal plane; (b) Inversion and eversion of the foot in the frontal plane (adapted from: http://wyrhrf.weebly.com).

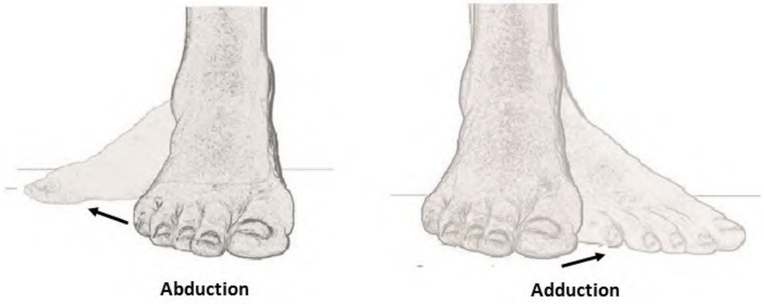

Figure 1.8: Abduction and adduction of the foot in the transverse plane (adapted from: https://www.orthoticshop.com).

A synovial joint is a type of joint surrounded by a structure made of fibrous connective tissue called articular capsule, which defines a cavity filled with synovial fluid (figure 1.9). The articular cartilage, a thin layer of hyaline cartilage which covers the articulating surface of each bone, reduces friction and contact pressure and keep a constant temperature within the joint. This allows the bones to move smoothly against each other, increasing the joint mobility. The friction is further reduced by the synovial fluid.

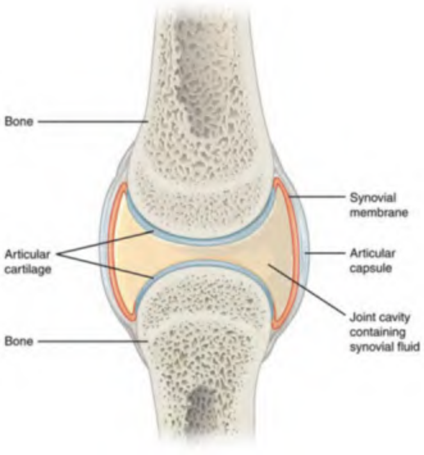

Figure 1.9: Detail of a synovial joint (adapted from [7]).

The subtalar joint is a triplanar joint formed by the calcaneus and the talus, which is mainly responsible for the inversion and eversion movements in the frontal plane (figure 1.7 b)[5]. The transversal-tarsal joint, instead, is formed by the connection between the talus and the navicular and the calcaneocuboid joint (joint between calcaneus and cuboid) and also contributes to the inversion-eversion motion of the foot ([5], [8]). The combination of these joints determines a multi-axial motion, which occurs simultaneously to facilitate the human gait.

1.2.2 Biomechanics of the ankle

When evaluating the motion at the ankle joint complex, ankle and subtalar joints are principally considered ([6]).Their combined movement was initially assumed as a simple rotation around a fixed axis. Multiple studies have reported how the instantaneous axis of rotation translates and rotates during passive plantarflexion ([6],[9],[10]), indicating that the hinge joint concept is an oversimplification. In particular, a shift of the contact area during flexion was visible at both the trochlea tali and the tibial mortise ([11]). The triplanar movements are supported by a minimal change in length of the calcaneofibular (CaFi) and the tibiocalcaneal (TiCa) ligaments ([9],[12]), while the other ligament fibres are tightened only at the limits of motion. A representation of these structures can be seen in figure 1.10.

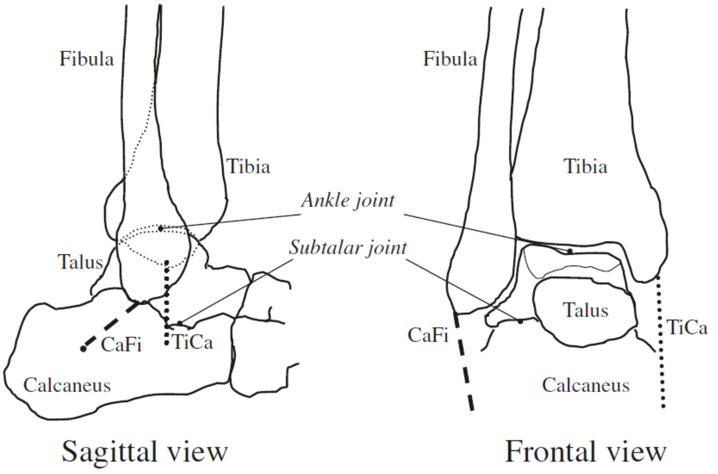

Figure 1.10: Representation of the main bones, joints and anatomical structures at the ankle joint complex (adapted from [6]).

In literature, the axes of motion of the ankle joint complex in the different planes are defined as follows: in the transverse plane the ankle axis is given by 84 degrees from the midline axis of the foot. The midline axis is definited as the axis running from anterior to posterior of the foot ([13]), while the ankle joint axis is passing through the centers of the medial and lateral malleoli ([14]). In the frontal plane, the axis of motion is located around the intersecting point between the line passing through the tips of malleoli and the long axis of the tibia ([3],[5],[13]). In figure 1.11 a-b it is possible to see their representation.

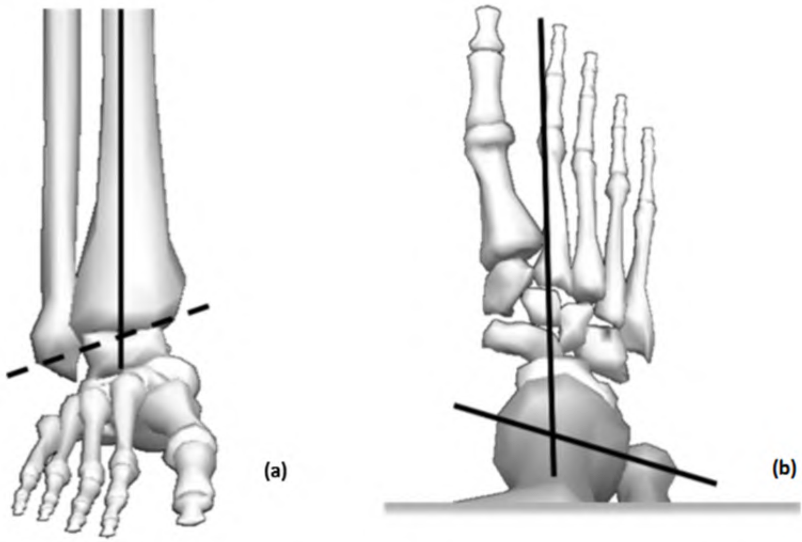

Figure 1.11: (a) Picture showing the sagittal (dashed line) and frontal plane axes of motion of the ankle joint complex. The intersecting point represents the rotation point for inversion and eversion (b) Picture showing the axis of rotation in the transverse plane of the ankle joint complex. The intersecting point represents the point for the internal and external rotation (adapted from [3]).

The axis of motion in the sagittal plane can be considered as dynamic and shifting during dorsiflexion and plantarflexion [15]. Lundberg et al.[16] analyzed the motion of the ankle joint using the röentgen stereophotogrammetry (a highly accurate technique used for the assessment of the three-dimensional motion of the skeletal system) in eight human volunteers: during full weight bearing the foot of each volunteer was carried from 30 degrees of plantarflexion to 30 degrees of dorsiflexion with increments of 10 degrees. The determination of the helical axes (the helical axis represents the axis of rotation and the line along which translation of the body occurs) for each pair of consecutive positions showed that all plantarflexion axes are more horizontal, or inclining downward and in the medial direction, than the dorsiflexion axes, which are inclined downward and in the lateral direction (figure 1.12).

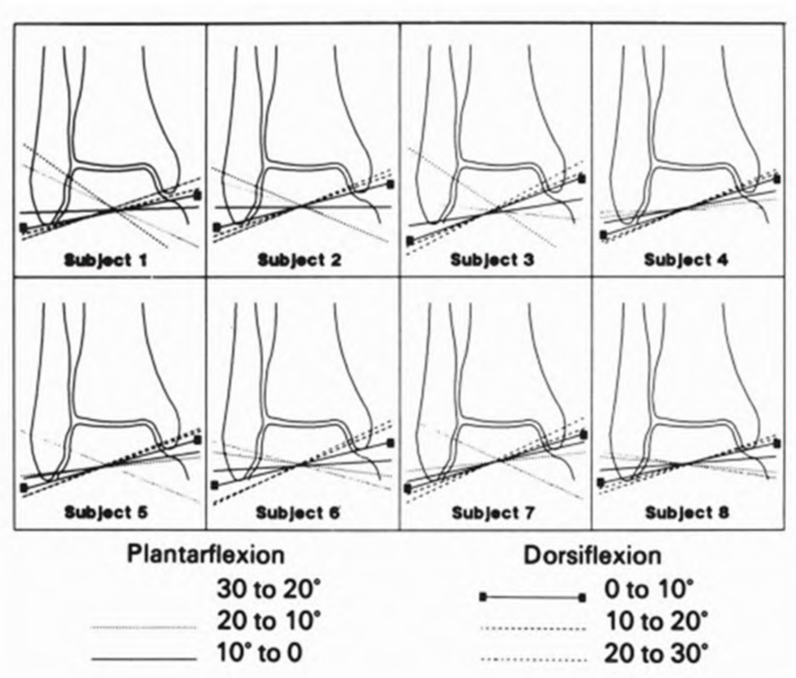

Figure 1.12: Helical axes of the ankle joint of each subject during plantarflexion and dorsiflexion. (adapted from [16]).

The outcomes obtained by Lundberg et al. confirm the results of Barnett and Napier [17] (based on the differences in the radial curvature of the medial and lateral aspects of the talus) and Hicks [18], who also believed that the ankle joint uses different axes of motion during dorsiflexion and plantarflexion. The transition during motion between these axes is predicted to happen around the neutral position of the joint [16]. Regarding the ankle range of motion, it can vary significantly between individuals due to several factors such as age and gender [19]. In literature, the reported ranges of motion in the sagittal plane are generally ranging from 10 – 20 degrees of dorsiflexion to 40 – 55 degrees of plantarflexion ([3],[8]).
Considering the range of motion during the stance phase of gait, Stauffer et al. [20] reported approximately 25 degrees, of which 10 degrees in dorsiflexion and 15 degrees in plantarflexion, while in the transverse plane they detected 5 degrees of ankle joint rotation; this contribution takes the name of abduction if the forefoot rotates away from the midline of the body and adduction if the forefoot rotates towards it (figure 1.8). In addition they also reported a total range of motion in the frontal plane of approximately 35 degrees (23 degrees inversion – 12 degrees eversion) [3].

In the past, a common convention was to consider dorsiflexion and plantarflexion as movements only of the ankle joint and inversion and eversion as movements only of the subtalar joint. Recently, this complete separation has been reconsidered; in fact, despite that most of the plantarflexion/dorsiflexion occurs at the ankle joint, a contribution also comes from the subtalar joint ([3], [21]). Leardini et al. [6] reported that, during the stance phase of gait, the joint rotations in the three planes of motion were respectively 15 degrees, 8 degrees and 8 degrees at the ankle joint and 7 degrees, 10 degrees and 7 degrees at the subtalar joint.
Concerning the motion in the transverse plane, two other studies, [22] and [23], reported 5-6 degrees of external rotation of the talus relative to the tibia when dorsiflexion takes place at the ankle; the rotation is reversed when the ankle goes into plantarflexion. Close [22] also reported 5-6 degrees of rotation at the ankle joint in the frontal plane during the stance phase. Lundberg et al. [24], using the röentgenographic technique, noticed that, going from 0 to 30 degrees of dorsiflexion, a maximal external rotation of 8.9 degrees of the talus was reached; from 0 to 10 degrees in plantarflexion, instead, a minimal internal rotation of 1.4 degrees ± 0.9 degrees followed by an external rotation of 0.6 degrees ± 3 degrees when 30 degrees of plantarflexion are reached. This trend is reported in figure 1.13.
From an anatomical point of view, it can be noted that the superior surface of the talus is larger anteriorly than posteriorly. However, going from dorsiflexion to full plantarflexion at the ankle joint, the articular surface of talus and malleoli always stay in contact and no play of the talus in the mortise is occurring and/or reported [8].

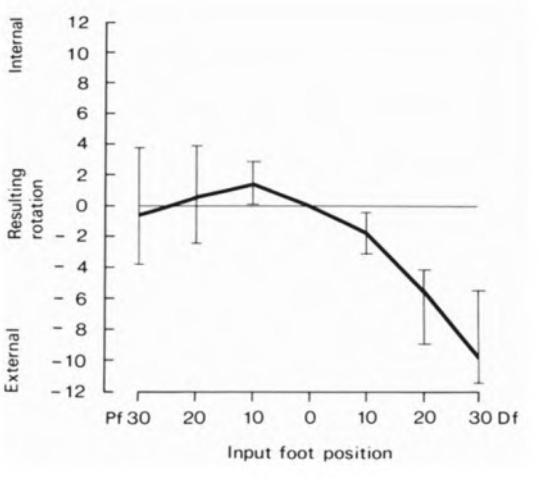

Figure 1.13: Horizontal rotation of the talus during plantarflexion/dorsiflexion movements of the foot (adapted from [24]).

As previously anticipated, the main movements at the ankle joint complex are dorsiflexion/plantarflexion in the sagittal plane, inversion/eversion in the frontal plane and abduction/adduction in the transverse plane. The simultaneous combination of dorsiflexion, eversion and abduction results in a triplane motion called pronation, while the combination of plantarflexion, inversion and adduction is called supination (figure 1.14). When the movements in the transverse plane are extended to the entire foot, the terms internal/external foot rotation are substituted to the adduction/abduction terms.

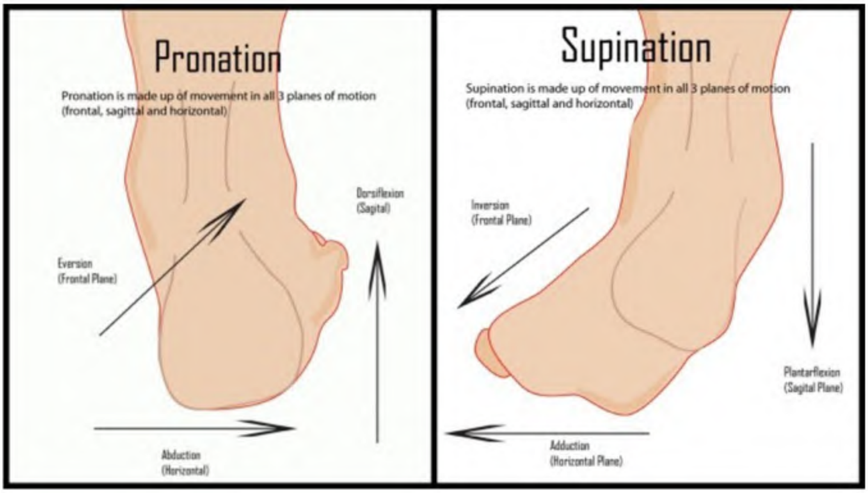

Figure 1.14: Pronation (a) and supination (b) of the foot (adapted from: http://www.newcastlesportsinjury.co.uk).

The stability at the ankle joint complex is determined by the action of several muscles and strong ligaments. These ligaments typically extend from the medial or lateral malleoli till the talus and calcaneus, as it happens for the strong deltoid ligament shown in figure 1.15. In addition, the ligaments prevent abnormal side-to-side and twisting movements of the talus and calcaneus during eversion and inversion of the foot. From a muscular point of view, the motion of the ankle and the foot is mainly controlled by four compartments of muscles, that originate in the leg and continue till the foot: the anterior, the lateral, the posterior and the deep posterior compartments. A representation of the main muscles of the lower leg is visible in figure 1.16.

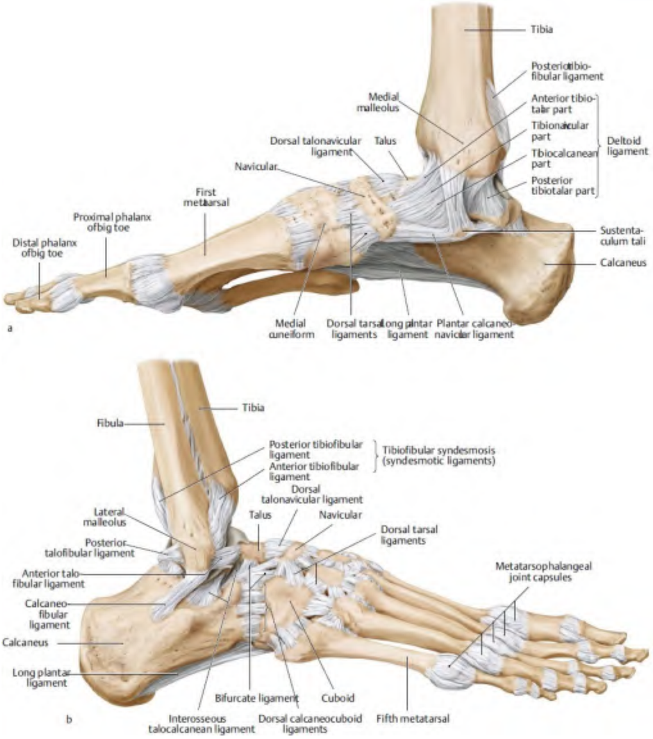

Figure 1.15: Medial (A) and lateral (B) views of the foot, where the location of different ligaments is depicted (adapted from https://musculoskeletalkey.com).

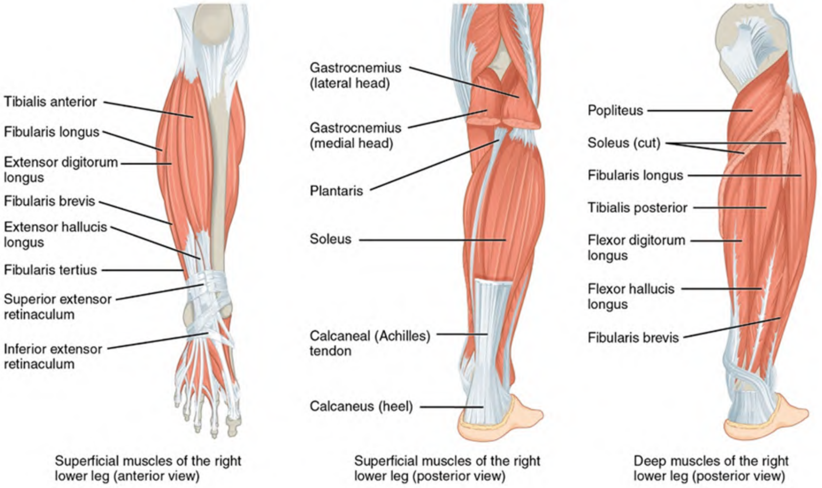

Superficial muscles of the right lower leg (anterior view)

Superficial muscles of the right lower leg (posterior view)

Deep muscles of the right lower leg (posterior view)

Figure 1.16: Different views of the main muscles in the lower leg (adapted from [7]).

1.3 GAIT

Ankle foot orthoses are prescribed for the correction of the pathological gait of patients, that exhibit neurological and/or musculoskeletal disorders. Before elaborating upon the main dysfunctions that can affect the physiologic gait pattern, a description of the normal gait cycle is provided. The gait cycle consists of two phases: stance or weight-bearing phase and swing or non-weight bearing phase. During a physiological gait, the stance phase corresponds to approximately 60% of the entire gait while the swing phase to 40% (figure 1.17).

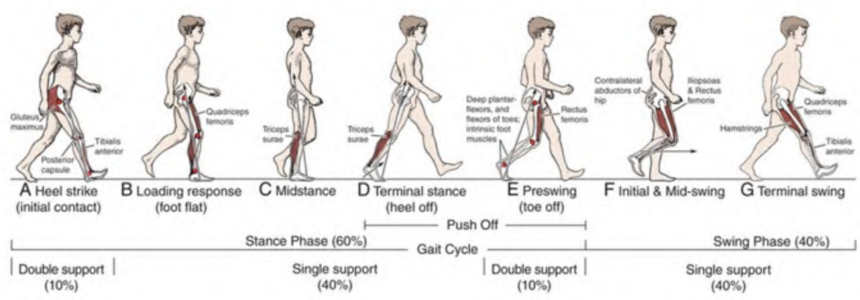

Figure 1.17: Physiologic gait cycle(adapted from [25]).

The stance phase can be subdivided in five phases: the heel strike (A) where the foot has the initial contact with the ground through the heel; the loading response (B) where the rest of the foot touches the ground until it is flat; mid stance phase (C) which starts with the foot flat and terminates with the heel rise. During this phase the other foot leaves the ground for the swing phase, transferring all the ground reactions on the forefoot. Subsequently, there is the terminal stance (D) which begins with the heel rise and ends when the other foot touches the ground. Then the final phase is called preswing (E), which starts with the contact of the other foot with the ground and terminates with the toe off. The body weight is transferred to the other foot. The swing phase instead is composed by the initial & mid swing (F), where the limb moves forward and the terminal swing (G), which ends when the foot touches the ground again.

Considering the motion of the ankle in the sagittal plane, the stance phase, under physiological conditions, can be subdivided into three sub-phases called rockers (figure 1.18): the heel (or first) rocker (a), the ankle (or second) rocker (b) and the forefoot (or third) rocker (c). The heel rocker begins with the heel strike, where the foot is neutral or slightly in plantarflexion, until the second rocker where the foot is completely flat on the ground and the

limb goes from plantarflexion to a maximum dorsiflexion (heel off phase), allowing the progression of the body. In the last rocker, instead, the foot rotates around the forefoot phase, starting when the calcaneus leaves the ground. The ankle starts to plantarflex reaching the maximum plantarflexion (about 20 degrees) approximately around the toe off phase. During the swing phase, instead, the ankle is initially in plantarflexion, then dorsiflexion till neutral position [8].
The flexion movement of the ankle is usually complemented by the movement at the subtalar joint, with about 15 degrees in eversion/inversion. In particular, the inversion normally occurs at the heel strike, changing to eversion during mid stance phase, in order to permit the heel to rise and the push off into swing. From the heel strike to foot flat we also have the internal rotation of the tibia resulting in the supination of the foot, while from heel rise to the push off the tibia undergoes the external rotation [26].

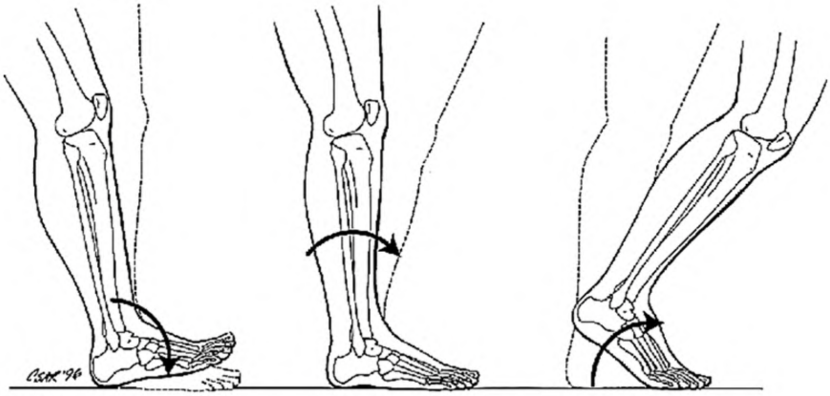

(a) Heel rocker *(first)*

(b) Ankle rocker *(second)*

(c) Forefoot rocker *(third)*

Figure 1.18: Motion of the ankle during stance phase (adapted from [27]).

1.4 PATHOLOGIES

Several neurological and/or musculoskeletal disorders can affect the physiological gait of a subject resulting in a pathologic condition. Foot drop is a common gait deviation where the weakened muscles are not able to support the foot and the ankle during the dorsiflexion movement in the swing phase ([28]). These muscles include the anterior tibialis, the extensor hallucis longus and the extensor digitorum longus (figure 1.16), which function is to ensure that the initial contact of the foot with the ground is through the heel (figure 1.17 a) and to control the movements of the foot till the end of the stride

([29]). Abnormal muscle activity will result in an abbreviated heel strike or forefoot contact due to excessive plantarflexion ([25]). This causes the rapid drop of the foot while the tibia stays in a vertical position [30]. During swing, the weakened muscles will cause a functional leg path discrepancy, and toe dragging [31].

Foot drop can be induced by several causes: motor neuron diseases as amyotrophic lateral sclerosis (ALS) or post-polio syndrome, tumors in the brain or spinal cord, diseases of the nerve roots of the lumbar spine, stroke are all neurological conditions that may produce foot drop ([28], [32],[33]). Another cause can be a direct damage to the involved muscles or even skeletal or other anatomical dysfunctions that can affect the movements of the ankle and foot. A combination of the neurological, muscular and anatomical factors can also be involved, which is known as the Charcot-Marie-Tooth (CMT) disease. This represents a hereditary neuropathy which affects both sensor and motor nerves and causes weakness and progressive loss of the muscle tissue leading to deformities [34].

Common ways used by the affected subjects to compensate for foot drop include steppage gait, circumduction and a persistent abducted limb. Steppage gait consists in excessive hip and knee flexion, which can lead to further hip problems; circumduction and abducted limb cause the movement of the limb, involved in the swing phase, away from the midline of the body and a lateral trunk inclination. In general, all these compensation methods alter the physiological gait, increasing the energy consumption and decreasing the walking speed ([35],[36],[37]). They are commonly noticed in elderly or cardiopulmonary compromised patients with foot drop. Another type of compensation is vaulting, which consists in the lengthening of the stride for the swing phase limb, which implies an increase of the energy expenditure. This is normally visible in young patients who try to keep the same velocity during gait. In case of other pathologies such as pain in the ankle, subtalar and/or midfoot joints or MTP joint arthritis, compensation techniques were noticed to provoke the shortening of the stance phase duration [37].

1.5 ANKLE FOOT ORTHOSES

The most common solution for treating gait disabilities is the prescription of external medical devices called ankle foot orthoses (AFOs), which are applied around the leg and foot to provide support and stability to the weakened muscles during gait and thus to improve the reduced walking ability ([38], [39], [40]). In order to consider an AFO successfully applied, it needs to provide all the desired functions for the expected amount of time, without causing discomfort to the patient. The impact of an AFO depends on the mechanical properties of the material used and the design: for obtaining the

optimal functional gains it is essential to customize the AFOs to the patients' needs [41].
In the past, AFOs were produced using metal bars connected to the shoe and the shank, which was made of leather [42]. These AFOs (figure 1.19 a) resulted to be uncomfortable and heavy, especially when children had to wear them. Afterwards, with the increase of plastics usage, custom-molded thermoplastic materials started to be employed, such as polypropylene (PP) or polyethylene (PE). They showed high strength, lightweight and manageability [43], which currently make them the most used materials, providing the patients with an intimate fit (figure 1.19 b). In addition, carbon fibers can be used, in order to manufacture reinforced plastic AFOs or to realize entire AFOs (figure 1.19 c) that can have a better impact in terms of energy efficiency (storage and return capabilities) during gait, in comparison to the other AFOs [44].

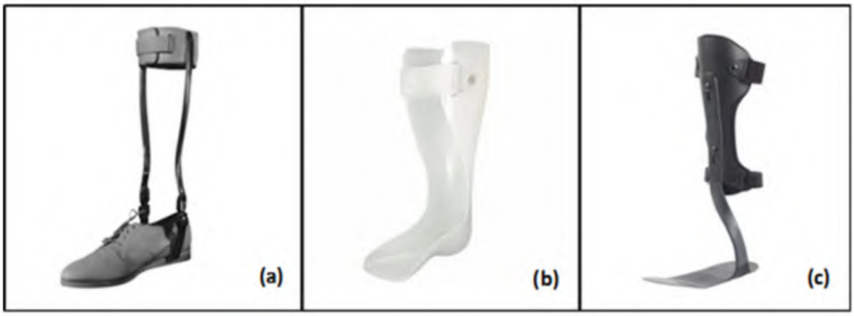

Figure 1.19: (a) metal, (b) polypropylene and (c) carbon AFOs.

In general, it is possible to find different types of AFOs depending on the function they provide to the patient and the involved components in the design: hinged, solid, posterior leaf spring or ground reaction AFOs. As suggested from the name, hinged (or articulated) AFOs (figure 1.20 a) contain a mechanical hinge in the proximity of the ankle, made of metal or plastic. This kind of orthosis allows control of the ankle dorsi/plantar flexion and blocks the movements in the other planes ([45],[46],[47]). The control in the sagittal plane is exerted by using stops that limit the range of motion of the ankle joint, depending on the pathology of the patient. For example, a restriction of the dorsiflexion range is applicable whenever there is weakness of the muscles around the tibia but at the same time a certain mobility of the tibia is wanted. On the other side, a restriction of the plantarflexion range is applied for preventing the foot drop during the heel strike or the swing phase. Solid AFOs (figure 1.20 b) are characterized by a rigid design in order to control the mobility of the ankle-foot complex in all the three planes ([48],[49]). They are usually made of polypropylene and used to treat several conditions such as weak ankle plantar/dorsi flexor muscles, spasticity, weak knee extensor muscles or deficiency in terms of proprioception. Posterior leaf spring AFOs (figure 1.20 c) are flexible devices which provide assistance to weak dorsiflexor muscles and optimal swing phase clearance [46] . They differ from the solid AFOs by the cut of the trimlines in proximity of the ankle section (posterior to the lateral malleolus, while it is anterior for the solid AFOs) [50] and they are mainly recommended for patients who already have a good stability in pronation/supination (mediolateral) and absence or moderate presence of spasticity. Ground reaction AFOs (figure 1.20 d) are specifically designed to use the moments caused by the ground reaction forces to improve the stability of the knee joint in the sagittal plane, during the stance phase. Crouch gait (excessive dorsiflexion at the ankle in combination with excessive flexion at the knee) can thus be better controlled [51].

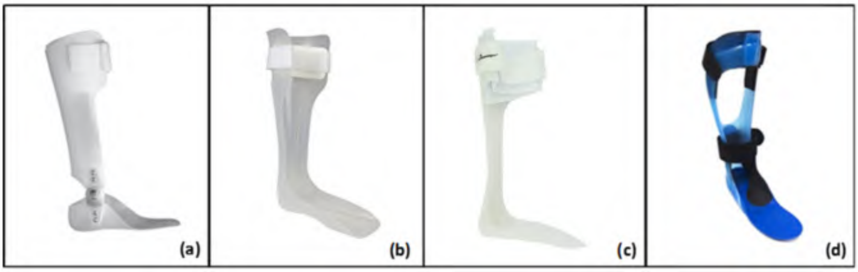

Figure 1.20: (a) Hinged, (b) Solid, (c) Posterior Leaf Spring and (d) Ground Reaction AFOs.

Currently, in the USA, the big majority of the AFOs are custom fabricated (73%) and made of thermoplastic materials (83%), compared to carbon (13%) or other materials (4%) [52]. The most common technique used for realizing thermoplastic AFOs is time consuming and a manual process performed by skilled orthotists (figure 1.21). The first step of the process is to take a manual plaster cast of the patient leg, which will then be filled with plaster to obtain a positive mold. The positive mold is then manually corrected and used for manufacturing of the AFO: a polypropylene sheet is first heated in an oven and then vacuum formed over the mold. After a cooling down phase, the plastic shell is removed from the cast and trimmed to the final design. In this context, a critical role is played by the CPOs (Certified Prosthetic Orthotists), who take the measures on the patients, and the production technicians, who apply their expertise to manually create the devices. Unfortunately, this way of manufacturing does not allow complete control of the AFO properties such as thickness or stiffness, which are key factors for determining the amount of assistance the orthosis is able to provide to the patients ([53], [54], [55]). In fact, every AFO can have its own mechanical properties and even bilateral AFOs for the same patient can behave in a different manner.

1. Taking a plaster cast

2. Result

3. Making positive mold

4. Manually correcting

5. Positive mold

6. Applying PP sheet

7. Vacuum formation

8. Result after Manual trimming

Figure 1.21: Different steps of the manufacturing process for thermoplastic AFOs (adapted from: http://www.sim-flanders.be).

By using 3D printing technologies, instead, the standardization and a more precise control of the design characteristics and the mechanical properties of these devices seems feasible. Other manufacturing techniques could also be partially or completely applied, such as computer numerical control (CNC) techniques: i.e. they can be used for the realization of metal parts within the AFOs [56], for the realization of the positive mold of the patients leg, in polyurethane foam, cork or ethylene-vinyl acetate (EVA) (Vorum Research Corp, Vancouver, Canada), which is employed during the conventional manufacturing process (figure 1.21, steps 3-5) or even for the realization of entire carbon fibre AFOs (Baltic Orthoservice, Kaunas, Lithuania). However the range of possible applications is still restricted and needs further development.

1.5.1 State of the art

Nowadays, different research groups are focusing on the use of additive manufacturing technologies: 3D printed AFOs are manufactured for healthy subjects and patients to study their mechanical contribution to the ankle biomechanics and/or compare their performance with the commonly prescribed AFOs.

For example, Mavroidis et al. [57] tested two custom-fit rapid prototyped AFOs obtaining good biomechanical data from the subject gait assessment, comparable to those obtained with prefabricated polypropylene AFOs. Choi et al. [58] investigated the impact of 3D Printed AFOs with different ankle dorsiflexion stiffness on the medial gastrocnemius muscle (MG) and Achilles tendon (AT) using two walking speeds. They noticed that increasing the stiffness of the AFO, the peak AT length decreased, while the peak MG length increased. At the same time peak knee extension and ankle dorsiflexion angles decreased. An adjustable 3D printed AFO was tested on a healthy participant by Telfer et al. [59]: different biomechanical effects on the kinematics of the patients were found, which could be varied by adjusting the stiffness level of the device in the sagittal plane.

Cha et al. [60], instead, designed and manufactured a 3D printed AFO in thermoplastic polyurethane, for a patient affected by foot drop, which showed similar functionalities as a conventional polypropylene AFO in terms of gait speed, cadence and stride length. It also resisted to a durability test (300000 cycles to simulate the AFO use by the patient), showing no cracks, damage or changes in shape and stiffness; in addition, the patient also considered the AFO satisfactory in terms of weight and ease of use. Creylman et al. [61] did a similar comparison by evaluating the clinical performance during gait of customized selective laser sintering (SLS) AFOs on 8 subjects with foot drop. No statistical differences were found between the SLS AFOs and the PP AFOs in terms of spatial temporal gait parameters and ankle kinematic parameters; they both provided a significant benefit in comparison to the barefoot gait of the patients. Deckers et al. [50] selected 7 patients to walk with PP and SLS AFOs (foot and calf part connected by carbon rods), each of them for 6 weeks: the study showed that some of the 3D printed AFOs failed, probably due to fatigue or inaccurate cutting of the carbon rods, highlighting the importance of more extensive characterization tests on the material, in addition to test bench and finite element analyses for predicting the behavior of the AFOs and optimize their design.

Harper et al. (A) [62] manufactured SLS AFOs for ten patients with unilateral lower limb impairments, finding comparable gait parameters with carbon fibre (CF) AFOs. Another study from Harper et al. (B) [63] used SLS AFOs to investigate the influence of stiffness on the walking performance of patients with the same pathologies. For each subject, three AFOs were produced: one with stiffness equivalent to the subject's clinically prescribed CF AFO, one 20% more compliant and one 20% more stiff. A decrease of the stiffness values showed an increase of the ankle range of motion and the medial gastrocnemius activity, while the kinematic, kinetic and electromyographic parameters showed comparable results. Stiffness impact is also the subject of the study carried out by Arch and Stanhope [64], where two healthy subjects walked at a scaled velocity while wearing a series of three 3D printed AFOs with different stiffness levels. The results showed how peak ankle plantarflexion moments remained unchanged across different stiffness conditions and that the patients used adaptive movement strategies due to the AFOs usage. Dimensional accuracy for SLS AFOs was investigated by Schrank et al. [41], by calculating the discrepancies between the original CAD model and the corresponding fabricated orthoses; values well under the tolerance limit (2mm), suggested by the literature, were found.

All the previous studies support the idea that additive manufactured AFOs can be a valid alternative for the treatment of the gait pathologies, providing good kinematic performance, consistency of shape and functional characteristics over the different production stages while decreasing the time needed during the manufacturing process, in comparison to the conventional methods. In addition, further studies should be done for better evaluating the fatigue behavior of the devices, since they will be subjected to many gait cycles exerted by the patients.

An evaluation of the behavior of the devices could also be done by using experimental setups and/or computational methods (briefly introduced in section 1.7), as suggested by Deckers et al. [50], which are the main subjects of this dissertation and will be further analyzed in the next chapters.

1.6 ADDITIVE MANUFACTURING

Additive manufacturing is the formalized name for what was used to be called rapid prototyping and what is commonly known as 3D printing and describes all those technologies that allow to manufacture 3D objects by adding layer-upon-layer of material under computer control [65]. This technology has a broad range of applications (automotive, aerospace, healthcare sectors), due to the possibility of using different materials: polymers, ceramics, metals, composites. Nowadays, these processes are being used more often and thus the medical world (prosthetics, orthodontics, pre-surgery models, etc.) is evolving and starting to embrace them.

The normal workflow consists in creating geometric parts in the STL file format by using 3D computer aided design (CAD) programs, which give more freedom to the designers and engineers in the realization of the design of the objects; this results in a potentially less expensive methodology and allows to explore new ways of design that were not possible before. The reverse engineering process can also be used, by starting from a geometric model i.e. obtained from CT scans of the object, which will be further modified and converted in a usable file format. Once the part is designed, the STL file is sent to the 3D printer for the complete realization. The commercialized additive manufacturing machines typically use a layer-based approach and the main differences between them are due to the supported materials, the printing velocity and the methodology of the layer creation, which determine the accuracy and the mechanical properties of the final part. By using

these technologies, a decrease of the production steps would be obtained in comparison to conventional methods. In fact, the production process with additive manufacturing machines normally requires fewer steps while traditional methods, especially when polymers are used, require more iterative steps, which can further increase if changes to the design are required.
The most common additive manufacturing techniques are the Stereolithography (SLA), the Fused Deposition Modeling (FDM) and the Selective Laser Sintering (SLS). SLA is considered one of the first 3D printing processes to be used since it was patented in 1986, leading to the first commercial machine produced by 3D Systems in 1987. It uses a liquid-based layer approach (figure 1.22) where an ultraviolet (UV) laser beam gives initiation to a curing reaction in a photocurable resin. The building process occurs in a vat of the resin; therefore a selected portion of the resin is cured (information provided through the STL file) and solidified by the laser on a platform. This platform is then lowered and a new portion of liquid resin is available for the creation of a new layer, which bonds to the previous one. The procedure is repeated until the entire object is submerged in the vat. After building, the object will be post-processed in a UV and/or thermal oven to further cure any uncured resin. Objects realized with this technique have poor mechanical properties (compared to other techniques) which can be affected over time and by light exposure and humidity.

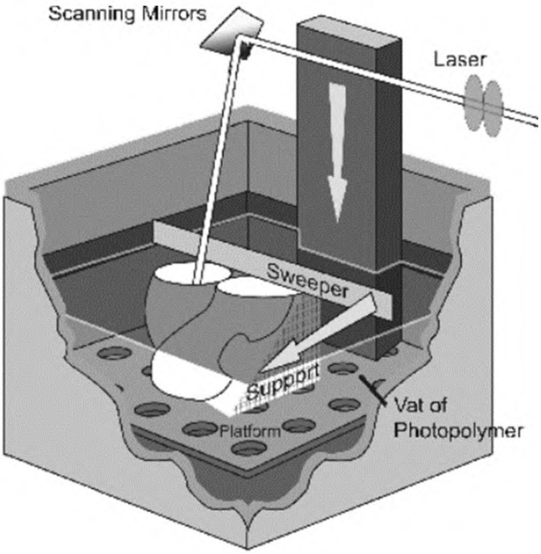

Figure 1.22: Stereolithography process [66].

FDM is a solid-based process (figure 1.23), which was firstly commercialized by Stratasys in 1991. This technology is based on the extrusion of a material through a heated nozzle which can move in two directions to create two dimensional layers onto a platform. A separate nozzle provides support material where required, which can be manually removed or dissolved in water, once the object is finished. Once the layers are deposited in the right position, the material cools down and hardens, bonding with the previous layer. Since the nozzles need to move over the building area, this can limit the printing velocity but the process is easy to setup and flexible; in fact, a wide range of materials can be used such as polycarbonate (PC), polylactic acid (PLA), acrylonitrate butadiene styrene (ABS), etc.

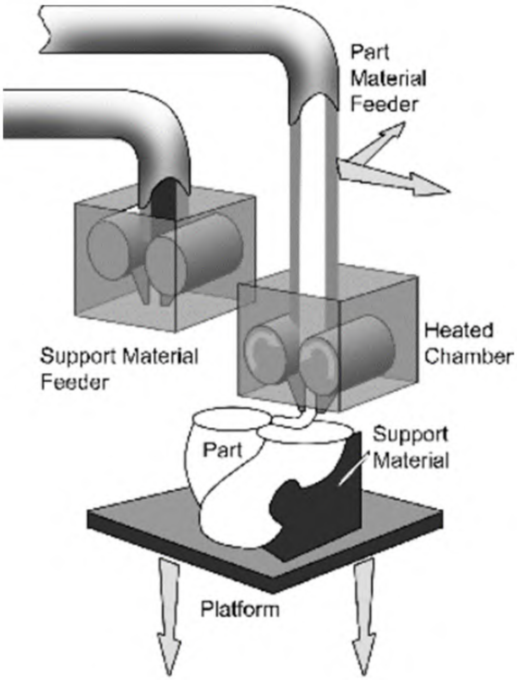

Figure 1.23: Fused deposition modeling process [66].

SLS, instead, is a powder-based technology which was firstly commercialized in the late 1980s, with the first machine sold in 1992 by DTM Corporation. This process (figure 1.24) is similar to the SLA and allows the formation of 3D objects by sintering successive layers of raw powdered material. In particular, a computer controlled laser scans the surface of a powder bed consolidating the particles in specific areas. A new layer of powder is then added while the platform is lowered for the creation of a new layer which bonds to the previous one. The sintering process is then repeated till the 3D object is created; the un-fused material, which surrounds the object, acts as support

material. During the process, the powder bed is pre-heated by the use of infrared heaters till a temperature lower than some degrees of the sintering temperature, in order to reduce the thermal gradients between the fused and non-fused material and decrease the energy needed from the laser for sintering the powder.
SLS allows the realization of objects with a greater geometrical complexity as compared to traditional processes and is considered more stable over time than the liquid-based processes like SLA. Moreover, it offers a wide range of material possibilities (polymers, metals, ceramics), which number is increasing due to the scientific research progress.
For example, highly crystalline polymers like polyamide (PA), also known as nylon, are being used; the action of the laser beam allows the PA powder to reach the melting temperature (TM), promoting good contact between the powder particles and the creation of 3D objects with good mechanical properties.

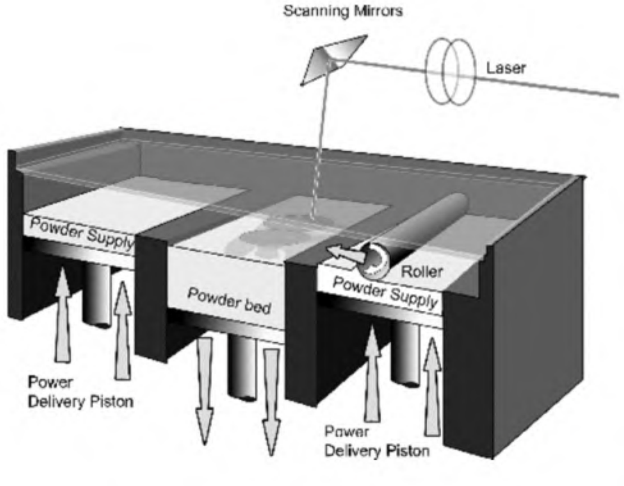

Figure 1.24: Selective laser sintering process [66].

Compared to the traditional thermoforming process of the AFOs (figure 1.20), it is obvious that the number of steps and resources involved in the product development chain can be significantly reduced; manual interaction is only required for the creation of the STL file, which needs to be sent to the printer, and this allows to decrease the manufacturing time, errors and waste of material. In fact, the application of the PP sheets, the trimming of the material and similar actions are tedious and difficult operations that might easily induce mistakes. If modifications of the devices are needed, this can even result in a remolding of the device and in a further increase of the costs, while easier and faster actions can be directly applied to the STL file. In addition, as done during this PhD project, STL files can be used for the realization of high quality finite element (FE) models for the prediction of the mechanical properties of the 3D printed ankle foot orthoses, which represent a strong tool applicable to the design process of the AFOs.

Besides all the benefits, there are some aspects of the AM technologies that need to be further investigated: for example, the mechanical properties of the realized devices are sensitive to parameters such as the printing direction or differences in bond strength between a single and/or different layers which can lead to different mechanical properties within the device. Also the heating and the cooling down processes during manufacturing can have an impact and, even impurities in the powder or evaporation due to the excessive laser power, can lead to porosities that will affect the performance of the final object [67].

1.6.1 Polyamide 12

The patient specific ankle foot orthoses described in this PhD dissertation are all made with polyamide (PA) 12, by selective laser sintering. This polymer was commercially introduced in 1997 and its use widely increased with the spreading of the additive manufacturing technologies, especially the selective laser sintering. Many studies were conducted to assess the mechanical properties on samples of this material. Lammens et al. [67] presented a detailed study where they evaluated the visco-elasto-plastic response of SLS PA 12 samples, which was determined by several dedicated experiments (tensile, compressive, shear and relaxation experiments). Tensile tests showed that, for a given speed, the Young's modulus is similar for all printing directions and the material can be considered isotropic within the elastic range. An increase of the Young's modulus is observed with an increase of the speed. In the plastic region, differences can be seen based on the testing speed (viscous nature of the material) and the printing direction, which make the material anisotropic. In addition, strength data suggest that the material might fail in tension rather than in shear. This study was important for the derivation of the parameters used in the material model applied for the predictions of the mechanical behavior of the 3D printed AFOs in the finite element environment, which will be further discussed in Chapter 4.

In the past, plastic and viscous effects of the PA 12 were mainly neglected while the focus of the studies was often the effect of the printing conditions. Starr et al. [68] studied the influence of processing conditions such as laser power, scan pattern, build orientation and position on the yield strength and elastic modulus of the laser sintered PA 12. Build orientation and other important parameters such as the supplied energy density, which is the amount of energy supplied to the particles per unit area of the powder bed surface, were studied by Cauliefield et al. [69], who investigated their influence on the mechanical properties of PA 12 (Young's modulus, yield strength, etc.). The anisotropy of the material, resulting from the build orientation and temperature changes during the manufacturing process, was assessed by Ajoku et al [70]. Another study [71] investigated the anisotropy of specimens of glass-filled PA 12, concluding that the material is transversely isotropic in Young's modulus and strain to failure and orthotropic in ultimate strength failure. The material was found to be inhomogeneous throughout the build volume and affected by ageing; further studies were demanded to prove if they were caused by moisture. Conversely, moisture and temperature effects were considered by Salazar et al. [72], who even compared fatigue properties of PA 11 and PA 12. Another study [73] evaluated the differences in terms of material structure and fatigue performance of PA 12 specimens realized from the same powder particles through SLS and injection molding. The main findings of this article were that the building direction of the SLS parts has a negligible effect on the fatigue properties, which are very similar to the injection molded parts, despite differences in terms of crystallinity, material density, fracture strength and surface roughness. The fatigue failure of all the samples was due to the tension-compression cyclic loading plus the temperature effect. In addition they observed that all the stress vs number of cycles curves converge to a value > 18 MPa. This is a bit higher with respect to the limit of approximately 15 MPa (regardless the build orientation of the samples) proposed by Munguia et al. [74], who performed fatigue tests by providing rotating bending loadings at 30 and 50 Hz. They also assessed that using a stress limit of 20 MPa would ensure a fatigue life of at least 1 million cycles of the samples.

The available information in literature represents a valuable asset for the full understanding of the mechanical behavior of PA 12, which usage and development will surely increase, allowing selective laser sintering technology to further become a widespread manufacturing technique for the realization of customized products.

1.7 CONTEXT OF THE RESEARCH

As described in Section 1.4, many pathologies can affect the physiological human gait, impacting the quality of life. AFOs can be used for treating these disorders and helping the patients to restore the lost functionalities. Many research studies (see section 1.5) demonstrated the efficiency of these devices and that new manufacturing methods, such as additive manufacturing, could be used for their realization. 3D printed AFOs, in fact, showed to be a good alternative to conventional polypropylene or carbon fibre AFOs by exhibiting good mechanical properties together with comparable kinematic and kinetic parameters. In addition, more control on the shape and geometry of the devices is obtained, since additive manufacturing technologies only require the implementation of an STL file where all geometrical details are contained. This allows to avoid production errors, which can occur in the conventional methodology, due to the manual work of the craftsmen. In addition, conventional manufacturing doesn't allow an accurate prediction of the mechanical behavior of the devices before their realization, which is a major limitation: in fact, even if their mechanical behavior would be more predictable, the AFOs would always be realized using the same manual procedure, prone to inter and intra-variability between skilled craftsmen. Knowing in advance how an AFO reacts to a certain load or movement would facilitate the application of the devices and optimize their design process. Therefore, the STL files used for 3D printing could be used, after some refinement process (further described in Chapter 4), for the implementation of computational models: modifications in terms of the AFO shape and geometry could be directly applied to the STL files and the impact on their behavior could be simulated. At the same time this process allows to avoid eventual waste of material, since more devices with different characteristics would need to be realized with conventional methods, and, as a consequence, results would be obtained faster.

1.7.1 Industrial and academic partners

In this context, a multidisciplinary research project, funded by VLAIO (Flanders Innovation & Entrepreneurship) and the A_STREAM_AFO project (Applied Structural Engineering of AM Materials for Ankle Foot Orthosis; project numbers: 140164 & 140165) under the SIM (Strategic Initiative Materials in Flanders) research program STREAM (STRuctural Engineering materials through Additive Manufacturing), was created. Many industrial and academic partners were included in the project:

- V!GO NV: industrial partner and coordinator of the project, responsible for the realization of the design of the devices, starting from the scans of the patient's leg till the STL files used for 3D printing. They also contributed to the realization of an experimental setup for the mechanical evaluation of the 3D printed devices (further details will be provided in Chapter 3).

- Materialise NV: industrial partner, responsible for the 3D printing of the devices by selective laser sintering (SLS).

- Devan Chemicals: industrial partner, responsible for the coating of the devices, which need to stay in contact with the skin of the patients without causing infections or bacterial reactions.

- Gait & Movement Analysis Laboratory, Cerebral Palsy Reference Centrum, University Hospital Ghent: academic partner, involved in the execution of the gait assessment of the patients, which provided useful information to be used in the experimental and computational environment.

- Mechanics of Materials and Structures research group, UGent-MMS: academic partner, involved in the experimental characterization of the samples of PA12, identified as the suitable material to be used within this research project. They also provided the parameters for the material model used for the virtual prediction of the behavior of the 3D printed devices (described in Chapter 4).

- Institute of Biomedical Technology (IBiTech) – bioMMeda at Ghent University: academic partner, responsible for the experimental (through the creation of an experimental setup described in Chapter 3) and computational evaluation (through the creation of patient-specific finite element models described in Chapter 4) of the mechanical properties of the AFOs, in order to create a standardized framework that can be used in combination with optimization algorithms to speed up the design and development of more effective 3D printed devices.

The purpose of the project was to apply the recent discoveries and developments in terms of additive manufacturing materials for the creation of a customized and usable prototype of a 3D printed AFO, in place of the conventional AFOs manufactured through vacuum forming technique. This prototype should be applicable to patients of all the ages and supply significant improvements to their gait pattern, paying attention in providing a certain level of comfort, since they need to be continuously worn. From a mechanical point of view, to be considered a successful AFO, it needs to provide the required amount of stiffness based on information provided by medical specialists after the gait assessment and clinical evaluation of the patient, and it requires sufficient durability to withstand specific stress/strain values experienced when being worn by the patients. The AFO lifetime was estimated to be 2 years in a child and 5 years in an adult, which corresponds to 3 million walking cycles in an adult. The aim is to create a novel workflow integrating information coming from different partners and sources, such as the gait analysis, design requirements, computational and experimental testing, to realize more effective devices

More in detail, the AFO stiffness quantified around the ankle joint represents the main focus of this dissertation, identified within the research project as the key parameter that can determine how much support the AFO is able to

provide to the patients, and might be used in the clinical setting to improve their prescription process or as an input for rigid body kinematic models to predict the impact on the gait pattern of the patient (part of the research project of the Gait & Movement Analysis Laboratory, Cerebral Palsy Reference Centrum, University Hospital Ghent). In fact, the quantification of the ankle stiffness is currently not included in the AFO prescription process, where the AFOs are only defined as rigid, flexible and/or semi-rigid/flexible based on the experience of the clinical staff. Including a quantification of such a parameter will be helpful for improving the entire process, which is now more trial and error, that currently can include the production of multiple AFOs for the same patient, until a suitable configuration is found.
In this dissertation, the evaluation of the ankle AFO stiffness was performed by experimental and computational means. The experimental evaluation required the creation of a dedicated experimental setup, which allowed the quantification of the AFOs stiffness around an axis aligned with the anatomical ankle joint during the second rocker of the stance phase of the gait over their range of motion, derived from a previous gait assessment. In addition, the reliability of the setup was measured in terms of the test-retest, intra-tester and inter-tester variability by statistical methods. The experimental results were then used for the creation of a computational framework, where different finite element models of the patient-specific devices, implemented for the prediction of the ankle stiffness and the stress distribution, were validated. This represents an applicable strategy for the optimal evaluation of the mechanical properties of the 3D printed AFOs prior to their realization in order to improve their manufacturing process, by the combination with optimization design algorithms, and to provide further means for facilitating their clinical prescription.

1.8 HYPOTHESIS AND OBJECTIVES

This PhD work is based on the hypothesis that the mechanical properties of patient-specific 3D printed AFOs can be evaluated before their physical realization by the utilization of advanced numerical models, which are validated through the utilization of a dedicated experimental setup, able to reproduce the conditions that the AFOs undergo during the second rocker of the stance phase of the gait. To test this hypothesis, the following objectives were defined:

- the creation of an experimental setup able to quantify the stiffness of patient-specific AFOs with different topology around an axis aligned to the anatomical ankle joint in the sagittal plane, over their range of motion, during the second rocker of the gait in a non-destructive manner. The development of the design of the setup is based on the idea that it will be further extended in order to allow testing of the AFOs around other axes of motion.

- the analysis of the ability of the experimental setup to provide reliable results under different working conditions, such as the test-retest reliability and the intra-tester and inter-tester variability.
- the implementation of an algorithm for the conversion of the STL files of the AFOs, intended for 3D printing and containing only the geometric parameters of the surface of the AFOs, in a usable format for the numerical analysis, since their direct use might provide inaccurate outcomes.
- the implementation of a computational framework where accurate FE models are used for the prediction of the ankle stiffness of and the stress distribution in the patient-specific AFOs in a short amount of time, that can be used in combination with optimization algorithms for the design and realization of more effective AFOs.
- the validation of the FE models by using the results obtained from the experimental setup, since the applied boundary and loading conditions are implemented to mimic the conditions established in the experimental setup as closely as possible. Different techniques are used to find an efficient way to obtain the prediction of the AFOs behavior.
- the possibility of evaluating different types of AFOs by the developed numerical simulations, in order to prove that the strategy is potentially extendable to different AFO topologies.

1.9 THESIS OVERVIEW

This thesis is divided in five chapters which present the methods used for the accomplishment of the previously discussed objectives and that will be briefly summarized in this paragraph. In particular:

- **Chapter 1** introduces the main concepts of the anatomy of the lower limbs, together with an illustration of the gait cycle and the most common pathologies, which might require the use of AFOs as treatment option. In addition a description on the different types of AFOs and the main 3D printing methods is included. At the end of the chapter the context of the research, the hypothesis and the objectives of this work are summarized.

- **Chapter 2** provides a literature review on the different approaches described to assess the performance of the AFOs by using experimental and/or computational methods or a combination of both.

- **Chapter 3** describes the design of a novel experimental setup, which allows to quantify the ankle stiffness of 3D printed AFOs over their specific range of motion in the sagittal plane during the second rocker of the gait. In addition, the analysis of the reliability of the setup, carried out by statistical means, is also included.

- **Chapter 4** gives an overview on the computational strategy used for the creation of the FE models of the patient-specific AFOs. The results in terms of the ankle stiffness and the stress distribution on four FE models are provided and validated by the comparison with the results obtained from the experimental setup described in Chapter 3.

- **Chapter 5** concludes this dissertation by describing the main contributions that this work provides to the scientific community and suggests ideas to further develop and improve the analysis of the AFOs from both an experimental and computational point of view.

CHAPTER 2

EXPERIMENTAL SETUPS & COMPUTATIONAL MODELS OF AFOS

The experimental results, that are described in Chapter 3, were obtained from the utilization of a dedicated experimental setup for the quantification of the ankle stiffness of patient-specific 3D printed ankle foot orthoses in the sagittal plane during the second rocker of the gait cycle. The acquired experimental results were then used for the validation of finite element models of the 3D printed AFOs, created for simulating their behavior in the same range of motion used in the test rig, derived from the gait assessment of the patients. Before providing a more detailed description of the methodologies used in this work, the current chapter wants to supply a general introduction, followed by a literature review, where the approaches used in the past by the other research groups worldwide are described. Moreover, the advantages and disadvantages of using experimental and/or computational methods or a combination of both are discussed.

2.1 INTRODUCTION TO THE CONCEPT

The biomechanical functions of a prescribed AFO are extremely important for the successful application of the devices, since they directly impact on the patient's conditions, by providing stability and control to the ankle joint area. Amongst all, AFO stiffness, which is defined as the moment around the ankle joint exerted by the AFO per degree of ankle joint rotation [75], plays a big role in restoring a natural gait pattern for the patients: i.e. it determines how the gait will be influenced by adding a certain contribution to or against the action of the patients' muscles [76]. The value of stiffness of an AFO can be affected by different design parameters: the material, the shape, the curvature or the thickness, without forgetting the conventional manufacturing process (thermoforming), described in Section 1.5, which is currently the most used fabrication method [52] and can introduce unpredictable modifications to the design parameters, not assessable before the production of the devices. The methodologies used for the quantification of the mechanical properties of the AFOs are twofold: experimental and computational, each of them with different particularities. The experimental approach is time consuming and expensive and can involve different sources of error, depending on the applied method. This methodology can be subdivided into two categories: quantifications that require the construction of a specific test rig (1), where the AFOs are fixed inside, and measurements directly on the leg of the patients wearing the AFOs during daily activities (2), which are called functional analyses [77]. The computational approach, instead, requires the construction of AFO computational models using finite element (FE) methods, which are based on the fundamental mechanical equations and aim at simulation and prediction of the behavior of the AFOs for unimpared subjects or patients. This methodology can be used to improve the manufacturing process of the devices; in fact, modifications can be directly applied to the geometry of the object by manipulating the STL file, intended for the 3D printing, and that can be used for the creation of computational models, allowing for the prediction of the mechanical properties of the devices before their physical realization. The introduction of this step, in the production chain, should increase productivity and decrease timelines and costs. On the other hand, in order to obtain reliable results, it is important to use accurate material properties and boundary/loading conditions, with these being as close as possible to real life situations. In addition, the validation of the computational results, using experimental tests, is an important aspect for proving that reliable results can be obtained and be applied as a suitable and successful complement to the experimental methods. In order to find the right balance between model accuracy and simulation run times, assumptions need to be made which define the context of the simulation results.

2.2 STATE OF THE ART

2.2.1 Experimental tests on AFOs

Several research groups have conducted experimental tests for the determination of the mechanical properties of the AFOs. As previously said, they can be subdivided in two categories: tests that involve the use of an experimental setup and functional analyses. In the vast majority of the articles of the first category, the main focus is the quantification of the stiffness in the sagittal plane, where dorsiflexion and plantarflexion occur, by manual or automated test rigs. This is the case for the setup developed in 2009 by Bregman et al. , which was called BRUCE (figure 2.1) [75]: it is a manual controlled device which allows the measurement of the AFO stiffness around the ankle joint and the metatarsophalangeal (MTP) joint. In addition, the neutral angle around the ankle and MTP joints is quantified, since it was considered an important factor that influences the gait of patients. The reliability of the measures acquired on four different topologies of AFOs was assessed by calculating the test-retest repeatability, the intra-tester and inter-tester variability, which revealed high reliability: the intraclass correlation coefficient (ICC) for the stiffness measures was ranging between 0.98 and 1. Measures acquired for the neutral angle were reasonable (ICC = 0.79-0.92).

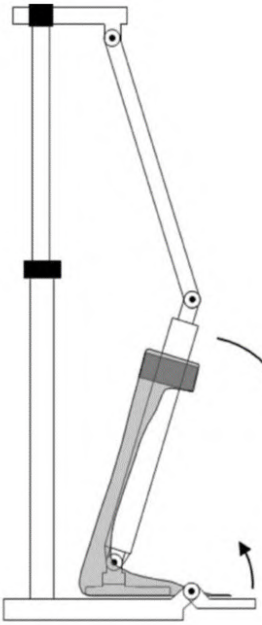

Figure 2.1: Schematic overview of BRUCE [75]. The arrows indicate the ankle plantar-dorsiflexion motion and the MTP flexion-extension motion.

Novacheck et al. [78] also used a manual controlled test rig (figure 2.2), which was previously created by Katdare [79], for assessing the stiffness and the energy return in the sagittal plane of three different designs of Posterior Leaf Spring AFOs. Repeatability between different tests showed positive results for the stiffness but not for the energy return. Speed was also evaluated, by conducting experiments at different values: 30 steps/minute, 40 steps/minute and 60 steps/minute. No influence of the speed was reported by the authors on the stiffness values.

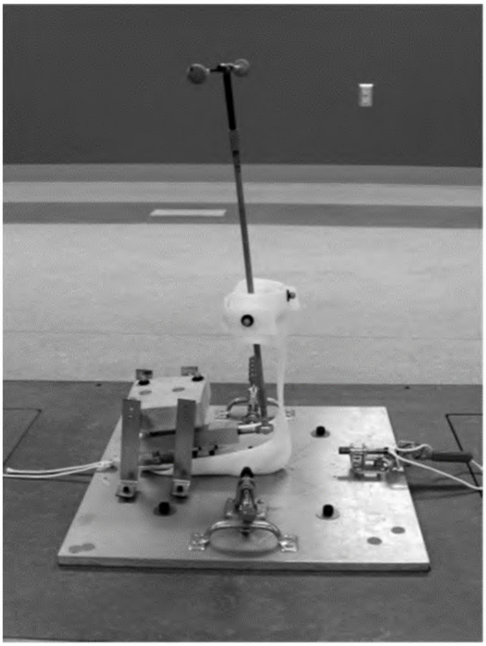

Figure 2.2: Picture of the experimental setup used by Novacheck et al. [78]. This tester was built by Katdare [79].

Nagaya et al. [80], conducted experimental tests to evaluate the flexibility, calculated as force vs. deflection angle, of 32 polypropylene AFOs during dorsiflexion and plantarflexion. The AFO was flexed with a force of 19.6 N, while the deflection was measured with a goniometer and strain gauges (figure 2.3). In particular, the angle was defined as the angle between a horizontal line and a line drawn at the posterior wall of the calf part and the posterior portion of the heel, probably not considering the neutral angle of the AFO.

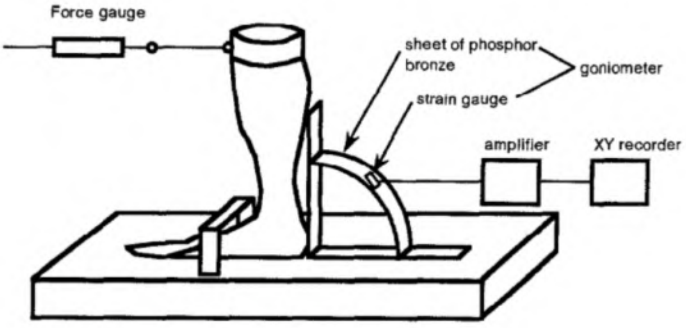

Figure 2.3: The experimental tester used by Nagaya et al. [80].

An automated device was realized by Kobayashi et al. [81] in 2010 (figure 2.4), which allowed to measure the stiffness of a thermoplastic articulated AFO till 15° in dorsiflexion and plantarflexion with a speed of 10 °/s. The AFO was positioned in order to have its rotational center in alignment with the rotational axis of the test rig. The rotational center of the orthosis is assumed to be in the middle of the joints. A rotary plate is positioned perpendicular to both the ground and the shank of the AFO. When measurements are performed, this is the orientation of the orthosis defined as neutral or at 0°. A plaster model is used as surrogate shank, which is penetrated by a prosthetic pylon. This pylon is fixed inside the surrogate shank, so that the surrogate shank would slide inside the AFO as a real shank would do. The accuracy of the test rig in reproducing the range of motion and the angular velocity was respectively of 4% and 1%, while the torque was measured with a maximal error of 8% at the neutral position.
One year later, the same research group published another article [82], where they modified the current setup to allow the possibility of accommodating the foot of a patient (figure 2.5). The torque was then applied manually around the ankle joint by using a steering wheel, while the range of motion was adjustable by using mechanical stoppers positioned under a bar connected to the steering wheel. Repeated measurements effected at 0°, 5° and 10° in dorsiflexion demonstrated high reliability with values of the ICC over 0.97.

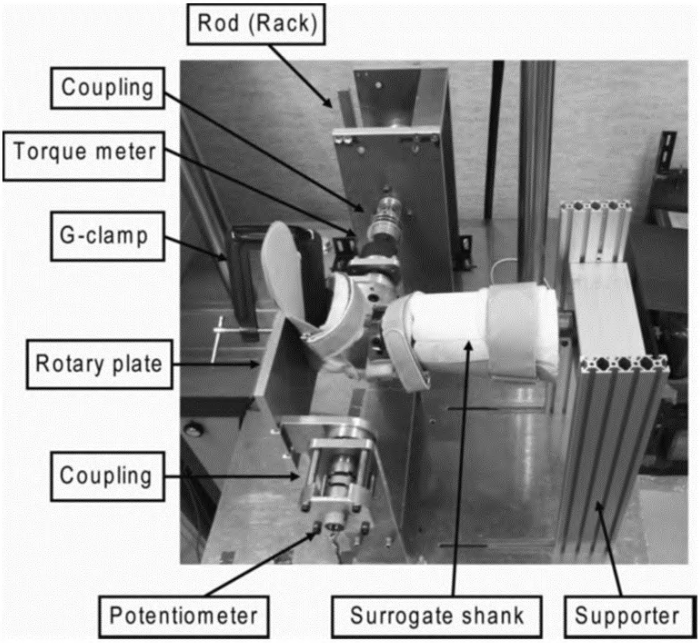

Figure 2.4: The automated control setup developed by Kobayashi et al. [81].

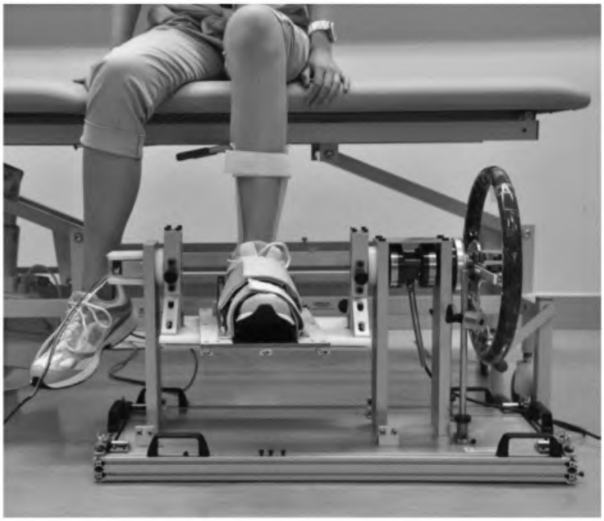

Figure 2.5: The manual control setup developed by Kobayashi et al. [82], as a modification of the test rig previously created [81].

In 2011, another study Gao et al. [83] measured the stiffness (at 0°, 5°, 10° and 15° in plantarflexion) of a thermoplastic polypropylene articulated AFO in the sagittal plane at a speed of 10 °/s (figure 2.6).

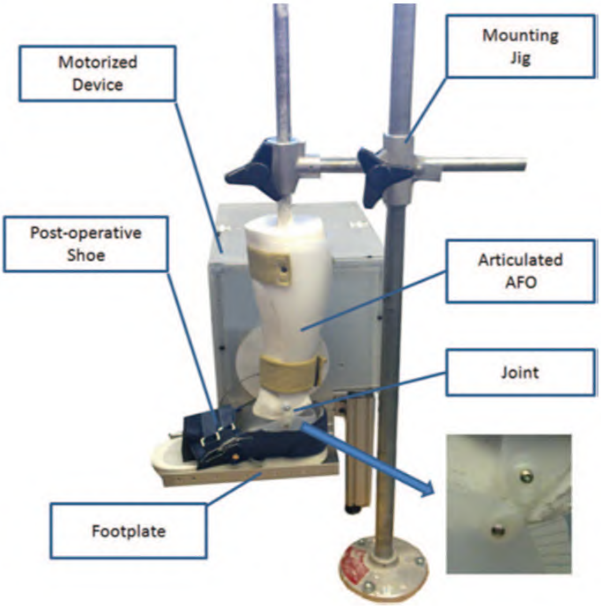

Figure 2.6: The automated setup used by Gao et al. [83].

The goal of the study was to quantify the effects of the AFO alignment and joint types (free motion or dorsiflexion assisted flexure) on the mechanical properties (stiffness, hysteresis index, passive resistance torque) of the AFO. In fact, the AFO was aligned with the center of the motor shaft and 10 mm superior, inferior, anterior and posterior with respect to the motor shaft center. As result of this, significant changes were found depending on the different joint types and alignments, suggesting that anterior and posterior alignments should be avoided since they increase the stiffness values, which might lead to potential skin irritation and higher stresses around the ankle joint in clinical practice. In addition, the dorsiflexion assisted flexure joints were found to be effective in assisting the ankle dorsiflexion, thus to facilitate the toe clearance during swing phase. Four different AFO designs were loaded in plantarflexion/dorsiflexion by Singerman et al. [84], who proved that changes in the design, specifically made to alter the stiffness, also have an influence on the kinematics of the AFOs. In particular, an increased trim on the AFOs results in a decrease of stiffness. The load was applied manually by an instrumented lever arm, attached to the plantar surface of the orthosis, where 12 strain gauges detected the values of moment in the three planes.

Sagittal resistive moments were, instead, recorded on plastic AFOs by Sumiya et al. [85],[86]; the static force was manually applied by using a lever arm and measured with a tensiometer (figure 2.7), while a protractor was used to set a deflection angle at 2.5 degrees intervals until a maximum possible value of 25 degrees. A plaster foot model was fixed to the AFO by screws and clamps. The authors report that a speed of 2 °/s was used, but in reality it would be complicated to have constant values of speed by the utilization of a manual controlled test rig.

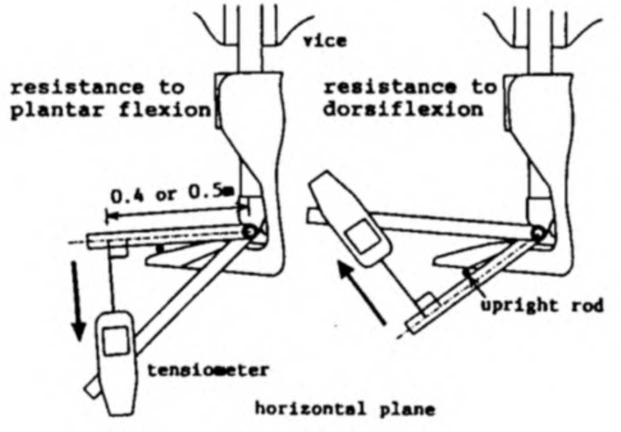

Figure 2.7: Measurement system used by Sumiya et al. [85]. Resistance to plantarflexion gives a measurement of dorsiflexion and resistance to dorsiflexion a measurement of plantarflexion.

DeToro et al. [87], manually measured the resistive force supplied at the forefoot during plantarflexion of 18 AFOs (realized with different materials). The static force was measured by a digital tensiometer, while the deflection angle through a digital goniometer. Screws were used to attach the AFOs at a surrogate limb, which was fixed at the shank level to a rigid support, in order to only allow the movement of the foot region. Four other studies evaluated the mechanical properties of the AFOs in the sagittal plane, but only in dorsiflexion: three of them respectively evaluated the strain [88], the force [89] and the stiffness [90] of polypropylene AFOs. Takahashi et al. [91], instead, evaluated the performance of a 3D printed AFO manufactured with PA 11 EX (figure 2.8). The footplate of the AFO was mounted vertically, by using C-clamps, to a base plate apparatus that was placed over a strain gauge force platform. The force, recorded by the platform, was applied manually through a cylinder deforming the AFO and the motion was registered through reflective targets of a motion capture system applied on the footplate and cuff. The goal of this study was mainly to prove that the AFO stiffness is sensitive to changes in the application angle of the provided loads.

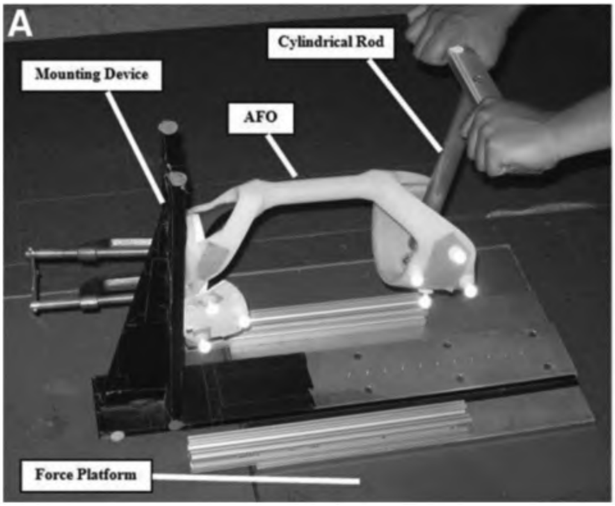

Figure 2.8: Measurement system used by Takahashi et al. [91].

Apart from the sagittal plane, the quantification of the stiffness in the other two planes (frontal and transverse) would surely provide a more complete information. Ringleb et al. [92] evaluated the stiffness of five AFOs, calculated as load vs. angular displacement of the footplate, with an automated testing device in the sagittal and frontal planes, using a speed of 0.5 °/s. Holes (2.5 mm diameter) were drilled to allow for the placement of reflective markers on the medial and lateral malleoli and on the calcaneus: stiffness in sagittal plane significantly decreased with respect to the situation where no holes are added, but not in the frontal plane. It was also noticed that stiffness in plantarflexion changed with the increase of the height of the medial malleolus hole. Assessment of the stiffness in the same planes of motion was provided by Yamamoto et al. [93], who tested 11 polypropylene AFOs realized with different designs. A muscle training machine was used, where the patient's foot could be attached to a footplate, connected to a pulley. The pulley axis, which was attached to a driving shaft, rotated at a constant velocity in correlation with the program of the muscle training machine. Three different velocities were used during the measurements (5, 10 and 50 °/s), which, according to the authors, showed to have no impact on the stiffness measures. In 2003, Cappa et al. [76] firstly created a manual device to evaluate the stiffness of the plastic AFOs in the sagittal and frontal planes; some years later [94], they created an automated device for the quantification of the stiffness of 2 polypropylene AFOs for the same patient in the three planes, for obtaining a more accurate approach in the AFOs assessment. The method involved the application of known ankle joint rotation and the measurement at the knee joint of the AFOs reaction forces by a load cell (figure 2.9). In the latest article, they claimed to have obtained uncertainty values always lower than 1 %, while in their previous, this value was at 4%.

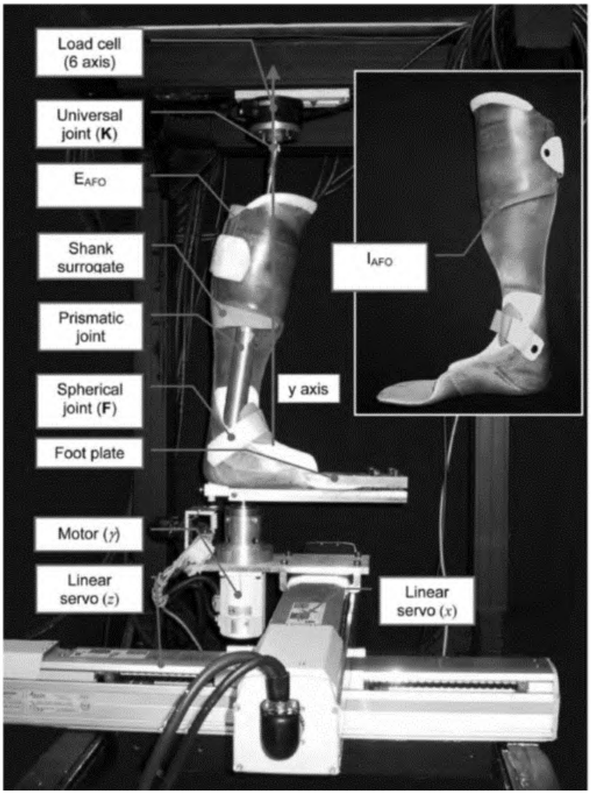

Figure 2.9: Measurement device used by Cappa et al. [94].

The quantification of the stiffness in the three planes was performed in two other studies: Bielby et al. [95], tested polypropylene AFOs for the same patient investigating changes in stiffness when modifications to the trimlines were applied, without using a surrogate limb, while Klasson et al. [96] did. Both setups required a manual control by testers. A study by Polliack et al. [97], evaluated the performance of polypropylene and composite AFOs, subjected to static or impact loads. In the static mode, the authors claimed that the used apparatus could simulate three phases of the gait (heel strike, mid stance and terminal stance), assess an isolated region of the AFO and test the entire AFO freely. Load blocks were added manually through a system of cables and the obtained deflection was measured (figure 2.10). No fixation of the AFO on the ground was requested.

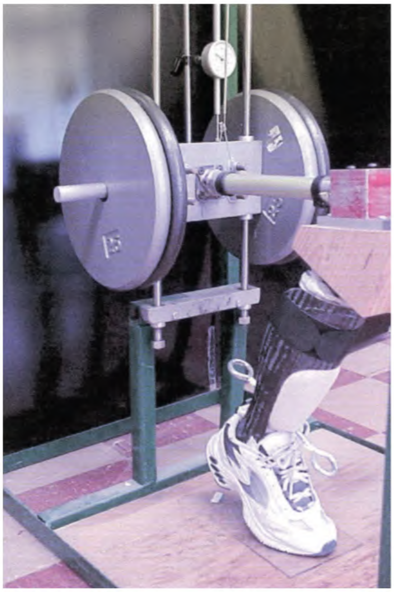

Figure 2.10: Testing apparatus with the surrogate limb attached to the AFO used by Polliack et al.[97]. In this picture also the load blocks and the dial indicator used to measure the deflection are visible.

Lai et al. [98], instead, developed an ankle foot simulator for assessing thermoplastic anterior-posterior AFOs, which are typically used to correct the gait of patients by providing ankle mediolateral and postural stability. These AFOs are susceptible to failure and are not commonly employed for a long time. Therefore, the goal of the study was to evaluate the AFOs failure mechanism during cyclic walking and stepping (figure 2.11) in the sagittal plane.

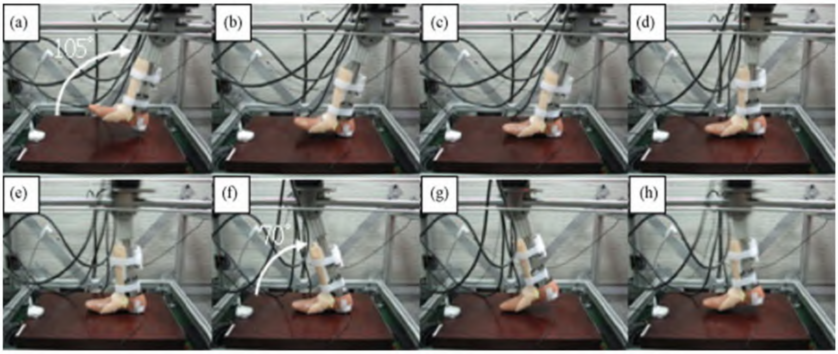

Figure 2.11: Cyclic stepping with ankle plantarflexion and then dorsiflexion (a)-(f); while in (g) and (h) the foot is lifted and returned to the initial position for a new cycle [98].

Failure mechanisms (and stiffness) were also studied by Sheehan et al. [99], who tested 9 carbon fibre AFOs, by providing a compressive loading at 200 N/min through two Instron machines.

As already mentioned, AFOs can also be experimentally quantified through functional analyses, which require the devices to be directly measured on the patients' leg while they are involved in activities like walking, running etc. Strain gauges are commonly applied along the geometry of the AFOs for deriving their mechanical properties: Chu and Feng [100], calculated the stress/strain of 5 different types of polypropylene AFOs during various activities, identifying the maximum stress during the heel strike and toe off phases. Their location was in proximity of the AFO ankle region, which would cause the failure of the devices, as observed in clinical practice and predicted in a previous finite element analysis study [101]. In addition, the authors suggested that, in order to prevent failure, AFOs should be realized asymmetrically, with the lateral side wider and/or thicker than the medial side. Two other studies respectively quantified the assistive moment [102] and the stiffness [103] generated by AFOs during walking.

Conversely, the goal of Nowak et al. [104] was to evaluate the contact pressure between molded AFOs (MAFOs) and the patient leg during different activities, in order to optimize the design of the devices. MAFOs are commonly used to reduce the plantar contact pressure associated with foot ulcers in patients with diabetes, but, because of the discomfort, their usage is not encouraged. In the study, the contact pressure was acquired through a real time F-scan pressure measurement system (TEKSCAN, Boston, MA). The results demonstrated high contact pressures at the metatarsal region of the foot, around the ankle, heel and straps (the highest values were found during mid-stance phase of gait and stair climbing). No contact pressure was recorded on the posterior calf region, which suggested this area to be suitable for design modifications.

A list of the analyzed articles, which report experimental methods for measuring the AFOs, is summarized in table 2.1. It is possible to see that, whilst AFO stiffness is the most common focus, some authors refer to other mechanical properties such as strain or resistive force.

Table 2.1: List of articles (in alphabetical order) where bench tests and functional analyses on AFOs are conducted during one or more plantarflexion (PF), dorsiflexion (DF), inversion (INV), eversion (EV), abduction (ABD), adduction (ADD), internal (INT) and external (EXT) rotations.

Author	AFO ROM	AFO characteristics	Surrogate Limb	Final Outcome	Reliability measures
Bielby et al., 2010 [96]	4° PF - 4° DF/ 7° INV - 7° EV/ 7° ADD - 7° ABD	PP AFOs	No	stiffness	Inter-variabiliy by using five different testers
Bregman et al., 2009 [76]	10° PF - 20° DF (Ankle)/ 0°-30° FX (MTP)	4 AFOs with different materials	Yes	stiffness and the neutral angle	Repeatility between measures, inter-tester and intra-tester variability
Cappa et al., 2003 [77]	6° PF - 6° DF/ 10° INV - 10° EV	plastic AFO	Yes	stiffness	Global accuracy in terms of stiffness below 4%
Cappa et al., 2005 [95]	7° PF - 15° DF/ 12° INV - 15° EV/15° INT - 15° EXT	2 PP AFOs	Yes	stiffness	Repeatability between different tests.
Chu and Feng, 1998 [101]	Not available	5 PP AFOs	Patient Limb	stress/strain	Not available
DeToro et al., 2001 [88]	0° PF - 10° PF/ 10° DF - 10° PF	18 AFOs with different materials	Yes	resistive force	Not available
Gao et al., 2011 [84]	20° PF - 10° DF	PP AFO	Yes	stiffness	Repeatability within cycles and different tests
Klasson et al., 1998 [97]	2° PF – 3° DF/1° INV – 3° EV/2° INT – 3° EXT	PP AFO	Yes	stiffness	Not available
Kobayashi et al., 2010 [82]	15° PF - 15° DF	thermoplastic AFO	Yes	stiffness	Not available
Kobayashi et al., 2011 [83]	Not available	Not available	Patient Limb	stiffness	Repeatability between different tests at 0°, 5° and 10° only in dorsiflexion
Lai et al., 2010 [99]	Not available	thermoplastic AFOs	Yes	failure and kinematic parameters	Accuracy and repeatability of the leg simulator assessed during cycling walking and cycling stepping with and without AFOs in sagittal plane.
Lee et al., 2006 [89]	0° - 16° DF	PP AFOs	No	strain	Not available
Lunsford et al., 1994 [90]	0° - 10° DF	PP AFOs	Yes	force	Not available
Major et al., 2004 [91]	0° - 14° DF	PP AFOs	No	stiffness	Not available
Nagaya et al., 1997 [81]	1.2° PF - 12.2° PF/ 2° DF - 14.8° DF	32 PP AFOs	No	deflection angle	Statistical analysis used to investigate the influence of different parameters of the AFO design.
Nowak et al., 2000 [105]	Not available	Not available	Patient Limb	contact pressure	Reliability tests on the F-scan pressure measurement system
Novacheck et al., 2007 [79]	20° PF - 20° DF	4 AFOs with different materials	Yes	stiffness	Repeatability between different tests.
Papi et al., 2015 [103]	Not available	PP with CF reinforcements	Patient Limb	moment	Not available
Polliack et al., 2001 [98]	Not available	PP and composite AFOs	Yes	deflection	Not available
Ringleb et al., 2009 [93]	3° PF - 10° PF/ 1° DF - 9° DF/2° INV - 5° INV	5 Arizona AFOs	Yes	stiffness	Repeatability between different tests.

Author	AFO ROM	AFO characteristics	Surrogate Limb	Final Outcome	Reliability measures
Sheehan et al., 2016 [100]	Not available	9 CF AFOs	Yes	stiffness and failure	Not available
Singerman et al., 1999 [85]	10° PF - 10° DF	plastic AFOs	Yes	stiffness	Not available
Sumiya et al., 1996, 1 [86]	0° - 15° PF	plastic AFOs	Yes	resistive moment	Not available
Sumiya et al., 1996, 2 [87]	15° PF - 15° DF	30 PP AFOs	Yes	resistive moment	Not available
Takahashi et al., 2010 [92]	0° - 10° DF	3D printed AFO (PA 11 Ex)	No	stiffness	Not available
Tanino et al., 2015 [104]	Not available	Not available	Patient Limb	stiffness	Not available
Yamamoto et al., 1993 [94]	20° PF – 15° DF/ 15° INV – 10° EV	11 PP AFOs	Patient Limb	stiffness	Not available

2.2.2 Finite element models of AFOs

Complementary to the experimental methods, computational models can be used for the quantification of the mechanical properties of AFOs; several research groups have investigated the potential of using finite element (FE) models for the prediction of the AFOs behavior, which would allow the improvement of their design and manufacturing process. The main goal of the AFOs virtual representation is usually the calculation of the stiffness and/or the location of the maximum stress/strain values along their geometry. The most common procedure is to start from patient-specific geometric models obtained from laser scans or CAD files, which are then imported in the FE environment, where material properties, loading and boundary conditions are applied for achieving the best approximation of the devices behavior. In table 2.2, a list of the articles, where research groups have used FE models for the quantification of the mechanical properties of AFOs, is summarized.

Table 2.2: List of articles (in alphabetical order) where finite element models of AFOs are used. PP and PE stands respectively for polypropylene and polyethylene.

Author	AFO characteristics	Virtual Limb	Simulation program	Material properties	Boundary and loading conditions
Badescu et al., 2013 [109]	PP AFO with elastic steel wire insertions	No	Ansys	Not available	AFO sole fixed and Force = 200 N applied at the calf region in the sagittal plane
Chu et al., 1995 [102]	PP AFO	Foot model	Adina	All parts are linear, elastic and isotropic	Upper foot and AFO calf regions fixed; forces exerted by tendons and muscles; ground reactions included as concentrated nodal forces
Gomes et al., 2017 [106]	PE AFO	No	Ansys	Not available	AFO sole fixed and force of 50 N or deflections of 10 degrees applied at the calf region
Jamshidi et al., 2010 [107]	AFO composed of outsole, midsole and insole realized with different materials	Foot model	Ansys	hyperelastic and nonlinear for the AFO sole; bones and cartilage as linear and homogenous, ligaments and tendons as linear elastic; soft tissue as nonlinear, hyperelastic and homogenous	AFO sole in contact with the ground and forces/torques, recorded experimentally, exerted to the AFO sole by the contact with the foot.
Lee et al., 2006 [110]	PP AFO	No	Ansys	linear elastic	AFO sole fixed and deflection applied at the calf region.
Syngellakis et al., 2000 [111]	PP AFOs	No	Ansys	Multilinear elasticity	Constraints applied to the calf and heel regions; deflections till 15 degrees.
Syngellakis et al., 2012 [112]	PP AFO	No	Ansys	homogenous, isotropic, linear elastic	Different boundary conditions are applied on the heel region to evaluate their impact; displacements on the distal foot part
Uning et al., 2008 [108]	PP AFO	Foot model	Ansys	all parts as linear elastic isotropic	Preliminary study based on [36], plus friction effect between foot and AFO

In the most recent article of this category, Gomes et al. [105] used an AFO made of polyethylene (PE) for evaluating the impact in terms of stress and strain of using structural reinforcements in different zones of the AFO during the stance phase of gait and for preventing the opening of cracks in the device. The basic (un-reinforced) AFO model was modified to create 7 additional models with reinforcements in different zones. The analysis consisted in applying a force of 50 N or a nodal displacement resulting in 10 degrees of dorsiflexion on the proximal region of the AFO, while the sole remained fixed. No virtual representation of the patient's foot or leg was involved; including these parts would imply an increase of the simulation time and in the modelling difficulty, since other parameters, such as the material properties of the new parts or the contact properties between AFO and leg/foot, need to be inserted. Such an approach was used by three different research groups: Jamshidi et al. [106], proposed a virtual representation of the AFO in combination with a foot model, where bones, ligaments, cartilage, tendons and soft tissue were included. Bones and cartilage had elastic, linear and homogenous properties and were modeled as 3D quadratic elements. Ligaments and tendons as linear elastic, in order to bear only tension forces. The material for the soft tissue was non-linear, hyper-elastic and homogenous, whilst the sole of the AFO was divided into outsole, midsole and insole (figure 2.12) with different materials with hyper-elastic nonlinear properties chosen for each. The goal of the study was to optimize the function of the AFO by minimizing the stress on the patient's sole. Moreover, previously experimentally acquired time-dependent forces and torques, during the second rocker of the gait, were exerted to the sole. By imposing the contact between the sole and the foot, the forces were transmitted and even the effect on bones and tendons of the loaded AFO was continuously modeled. As a result, the authors claimed that, by using an optimized sole, a reduction of the stress values is reached, showing the possibility of achieving benefits in case of pathological gait.

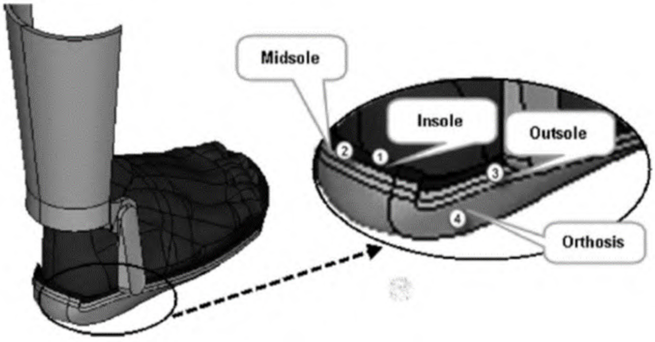

Figure 2.12: Model of the AFO and foot, where the different parts of the sole are indicated [106].

Another study from Chu et al. [101], considered all the involved parts as linear, elastic and isotropic (figure 2.13), in order to simulate the foot drop condition and study the consequent values of stress. The simulation required the fixation of the upper part of the foot and the AFO (calf region) to simulate the AFO strap action on the leg. Forces exerted in the Achilles tendon or in the flexor/extensor muscles tendons, during foot motion, and ground reactions were included as concentrated nodal forces. Maximum values of peak stresses were found around the AFO ankle and heel region; high stress concentrations around the ankle region are consistent with the common clinical observations, that this area is more susceptible to fatigue failure. No friction was considered by the authors between the different parts; therefore, Uning et al. [107], based on the work of Chu et al. [101], illustrated a methodology for simulating the behavior of the AFOs, by including interaction parameters between the AFO and foot. However, this was a preliminary investigation on the methodology and no results were reported.

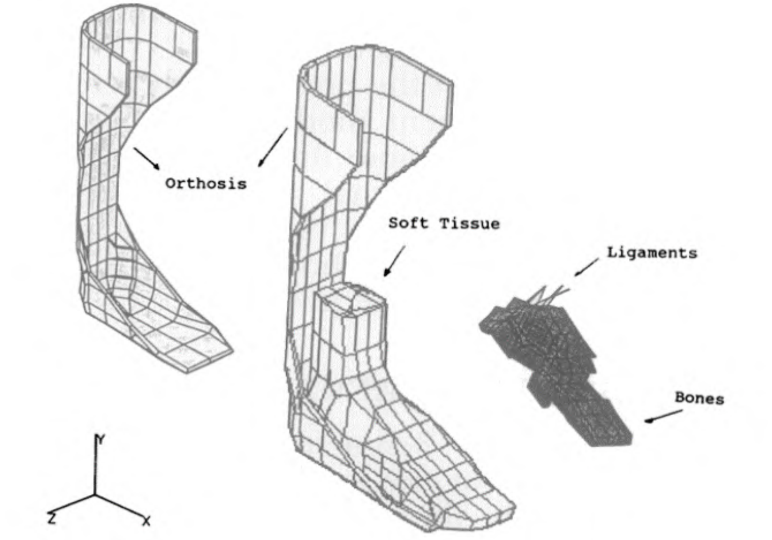

Figure 2.13: Model used by Chu et al. [101].

The other models present in literature do not consider the presence of a leg or foot in their analyses. Badescu et al. [108] reproduced the behavior of two polypropylene AFOs, in order to assess how elastic steel wire insertions influence the stress/strain values on the AFOs, since they believed this might be a new approach for their manufacturing process (figure 2.14). The analysis required constraining the sole and applying a force of 200 N to the calf region. The results showed that the area around the ankle joint, which is the area with the highest stress and strain, is less subjected to stresses when the steel insertions are included.

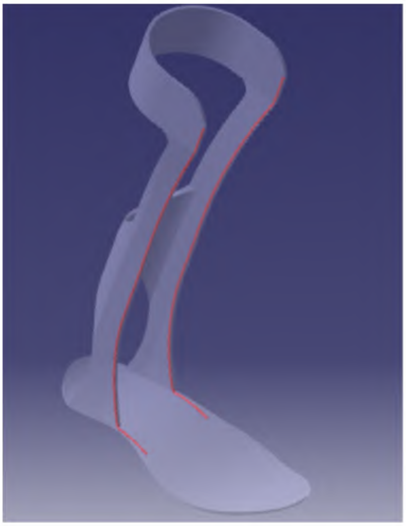

Figure 2.14: AFO model with wire insertions colored in red [108].

Similar loading and boundary conditions were applied by Lee et al. [109], who provided 20 degrees in dorsiflexion and 10 degrees in plantarflexion on a polypropylene AFO, while the sole was constrained (figure 2.15). The highest stresses were seen around the trimlines of the ankle part in agreement with other work. Subsequently, they performed a topology optimization analysis which showed how a 50 % volume optimization of the trimlines can be applied on the device.

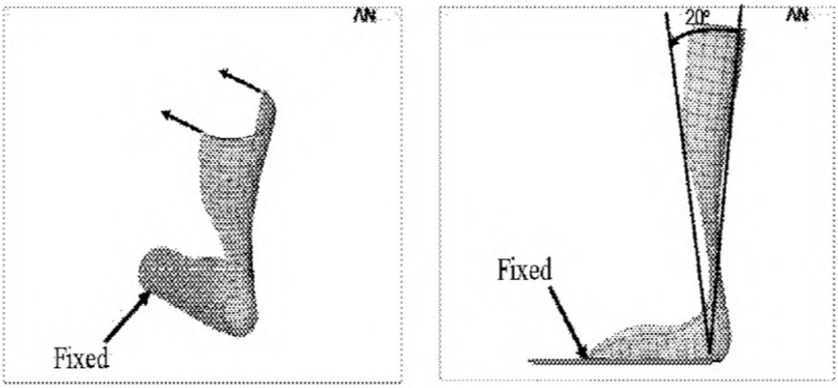

Figure 2.15: AFO model used by Lee et al. [109], where the sole is kept fixed while the calf region is rotated by 20 degrees. The situation showed in the current picture is for dorsiflexion.

The last two studies contained in Table 2 were realized by Syngellakis et al. and also imply simulations on polypropylene AFOs. In the oldest [110], they gave more focus on modelling and prediction of the nonlinear behavior of the devices, by including material nonlinearities and the large deformation effects. A geometrical model of the AFO was realized by starting from the subject leg, which was then modified according to previously selected geometric parameters of the AFO (figure 2.16).

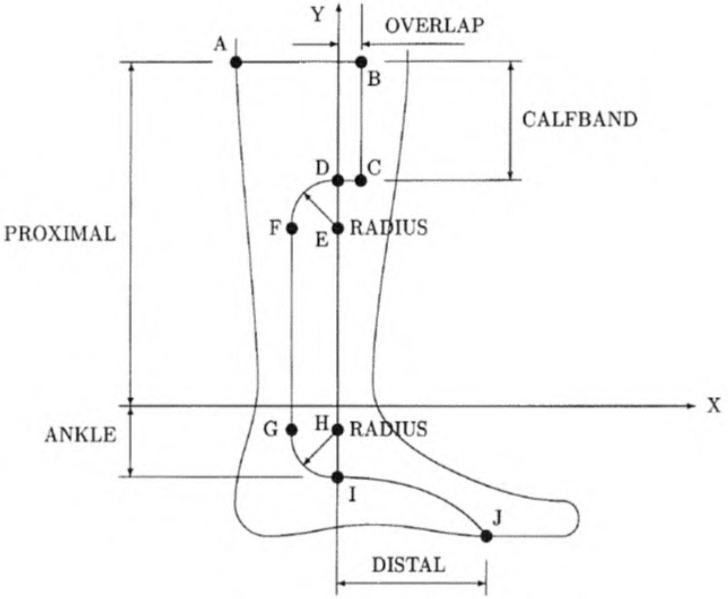

Figure 2.16: Parameters used by Syngellakis et al. [110] to define the geometry of the AFO.

The mesh of this AFO (thickness = 2 mm) required 8-node quadratic shell elements (549 in total) and nonlinear material properties were provided by using 8 points extracted from experimental graphs, in order to define a multilinear elasticity. The model was divided into smaller areas, thus to facilitate the application of loads and constraints to specific regions. In fact, partial constraints were applied to two areas of the calf region, in order to simulate the calf strap action and to allow the AFO to move up and down the calf and undergo internal and external rotations. Other constraints were also imposed on the heel region to simulate the shoe and foot. Loading conditions implied a rotation of 15 degrees in plantarflexion and dorsiflexion. The authors wanted to validate their models by comparing the outcomes with the experimental data obtained by Sumiya et al. [85], who reported how AFO stiffness changes with ankle trimlines variations; therefore, modifications to the geometric parameters and thickness were required for a better match of the AFO geometry used in the article of Sumiya et al.[85]. In the latest article [111], Syngellakis et al. aimed to assess the effect of changing parameters, such as the geometry, loading and boundary conditions. The AFO was divided into several areas and different values of thickness were provided for each area for simulating the characteristics of a vacuum formed AFO, which typically has a non-uniform thickness due the variability of the manufacturing process, as described in Section 1.5. The AFO meshes were realized with triangular and quadratic 8-node shell elements, while the boundary conditions were initially similar to the previous study. The comparison between an AFO with a uniform and a non-uniform thickness showed a small effect in terms of stiffness and stress. By changing the constraints on the heel region, larger differences were obtained, indicating how the magnitude and distribution of the stress and moment are dependent on the distribution of the imposed deformation.

2.2.3 Combination of experimental tests and finite element models of AFOs

In this paragraph, a list of the articles with a comparison between the experimental and computational results on AFOs is provided in table 2.3.

Table 2.3: List of articles (in alphabetical order) where experimental tests and finite element models of AFOs are combined. The following abbreviations are used: polypropylene (PP), carbon fibre (CF), polyamide (PA), polycarbonate (PC) and carbon fiber reinforced polymer (CFRP).

Author	AFO characteristics	Virtual Limb	Simulation program	Material properties	Boundary and loading conditions
Amerinatanzi et al., 2016 [120]	PP AFO with stainless steel or Ni-rich NiTi spring	No	Abaqus	superelastic NiTi properties implemented with UMAT subroutine while stainless steel as linear elastic	Derived from the experimental tests but not specified
Bellavita et al., 2017 [116]	CF AFO	No	Abaqus	orthotropic	AFO fully constrained at the ankle region and loaded with 10 mm displacement at the metatarsal head region
Chen et al., 2009 [115]	1 PP and 2 PC-ABS and ULTEM (3D printed)	No	Comsol	elasto-plastic	AFO sole fixed and a distributed load applied at the calf region
Faustini et al., 2008 [113]	3D printed AFOs in PA 11, PA 12 and glass filled PA 12	No	EDS I-deas™	elasto-plastic	AFO sole fixed and force applied at the calf region
Krukonis et al., 2017 [117]	AFO made of carbon fiber and glass fiber composite	No	Solidworks	isotropic homogenous	AFO heel part constrained and a load of 1500 N applied at the calf part
Leone et al., 1991 [119]	PP AFO	No	Marc	Not available	AFO calf region fixed and a load applied at the metatarsal head region
Schrank et al., 2013 [114]	3D printed AFOs in PC	No	Catia	linear and isotropic	AFO sole fixed and rotation applied at the virtual ankle joint, connected to the calf region
Stier et al., 2015 [118]	(CFRP) AFO	No	Abaqus	fibers trasversely isotropic and matrix isotropic	AFO clamped at two positions at the sole and displacement applied at the calf region
Zou et al., 2014 [45]	2 CF composite AFO and 1 PP AFO	No	Abaqus	CF AFOs with homogenous isotropic material; PP with elasto plastic	AFO calf region fixed and a load of 1000 N applied at the metatarsal head region

In this list, three studies used 3D printed AFOs: Faustini et al. [112], tested AFOs realized in PA 11, PA 12 and glass filled PA 12 through SLS. The aim was to validate the stiffness values of the different devices (figure 2.17) and evaluate the material dissipation energy and the ability to withstanding large deformations (destructive tests by a hydraulic axial load device were used). The stiffness tests were performed in the sagittal plane and revealed that the AFO realized in PA 11 was the most flexible and the only one that survived the destructive tests. This device was also the best performing in terms of dissipated energy, although not as good as a carbon fibre AFO, used as comparison.

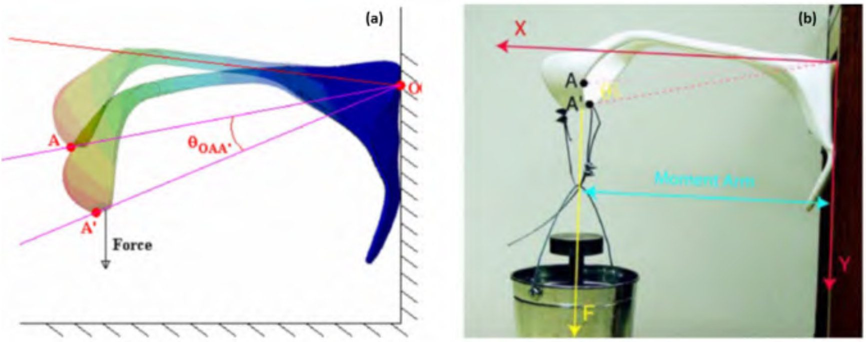

Figure 2.17: Computational (a) AFO representation and corresponding experiment (b) used by Faustini et al.[112].

The second study was realized by Schrank et al. [113], who assessed a virtual functional prototyping process (VFP) for the rapid manufacturing of polycarbonate (PC) AFOs. The devices were tested in a manual controlled test rig in the sagittal plane during a dorsiflexion motion. The goal of the test rig was to replicate the constraints, boundary and loading conditions that occur during the second rocker of the stance phase of the gait. The measuring device consisted of a base platform, a vertical endplate and two perpendicular metal rods coupled by a frictionless hinge joint (figure 2.18 a). The foot part of the AFO was clamped to the vertical endplate of the test rig and a force was manually applied to the longitudinal axis testing rod (figure 2.18 b). The virtual representation of the device was then realized, as visible in figure 2.18 c, where the presence of the testing rod, constrained to the virtual ankle joint center, was included. As in the experiments, a cuff insert was included between the AFO and the rod in order to distribute the pressure on the front surface of the AFO. By using the elastic modulus provided by the manufacturer, the validation of the stiffness values gave an error of 15.3 %, which decreased when a new elastic modulus, derived from the experimental tests, was used. The reliability of the experimental measures was also evaluated, showing a maximum test-retest error of 4.7 %.

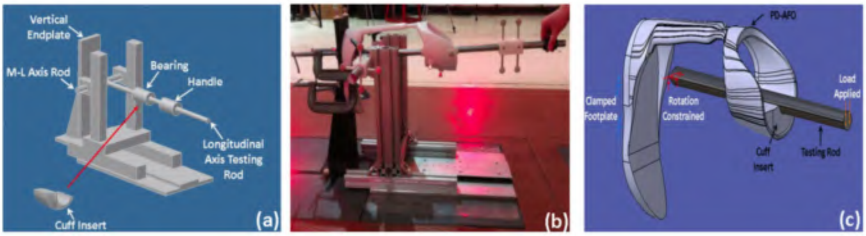

Figure 2.18: Experimental device used by Schrank et al.[113].

The last study was realized by Chen et al. [114] who used two 3D printed AFOs made in polycarbonate-acrylonitrile butadiene styrene (PC-ABS) and ULTEM using fused deposition modeling and one PP AFO. The experimental tests quantified the loading conditions of the AFOs by using strain gauges during the gait of the patient. The finite element simulations were created for the calculation of the static and dynamic loading conditions during the gait cycle and for the prediction of the stress, strain and bending stiffness of the AFOs. In particular, the results of the bending stiffness seemed to be overestimated.

Carbon fibre AFOs, instead, were the main focus of four studies: Bellavita et al. [115], wanted to assess the stresses acting on the AFO during the propulsive action of the foot during the gait cycle: while the AFO was constrained in proximity of the ankle trimlines, a rigid rod applied a deflection in the vertical direction at the metatarsal region causing dorsiflexion (figure 2.19 a).

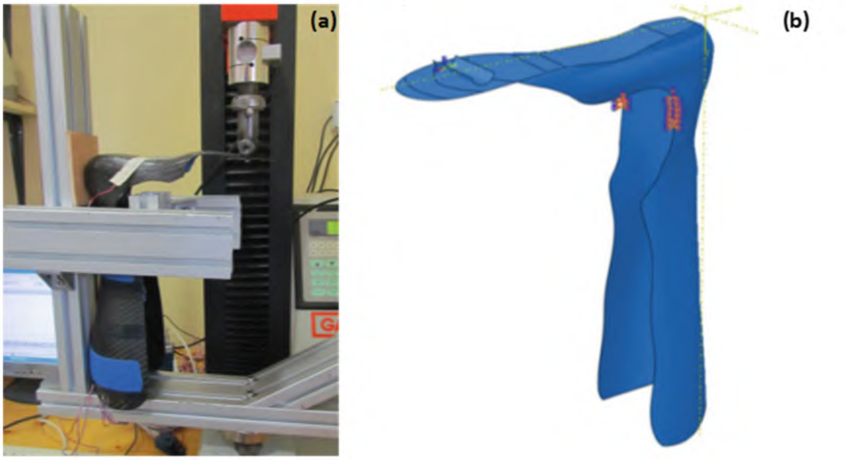

Figure 2.19: Experimental (a) and computational (b) setting used by Bellavita et al.[115].

In the simulation (figure 2.19 b), the bar was also included and the hard contact without friction between the rod and the AFO was imposed. Graphs in terms of stress (MPa) vs deflection (mm) and force (N) versus deflection (mm) were obtained. Subsequently, simulations were used to predict how concentric notches with different radius impact the AFO stiffness.
For the identification of the maximally loaded zones of the devices, static (computational) and dynamic (experimental) tests were performed by Krukonis et al. [116]: during the computational tests, the heel portion of the AFO was fixed while a force of 1500 N was applied on the superior calf part of the AFO, for simulating the weight of a patient of 150 Kg. During the experimental tests, functional analyses on two subjects (60 and 80 Kg) were conducted to assess the AFOs during daily activities. Both analyses identified the beginning of the spring part, close to the foot region, as the highest loaded region of the AFO (figure 2.20).

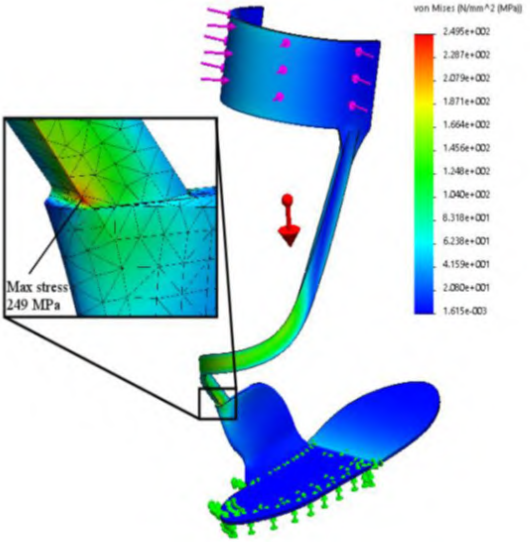

Figure 2.20: Highest loaded zone on the AFO (static test situation) which resulted from the study of Krukonis et al. [116].

Stier et al. [117], used experimental and computational methods to evaluate a carbon fiber reinforced composite (CFRP) AFO (figure 2.21). They clamped the sole and applied displacements at the calf at 2 mm/min in dorsiflexion by using a punch, which was also implemented in the finite element environment as a cylindrical analytical rigid body, while considering a frictionless contact with the calf zone. A graph in terms of Force (N) vs. punch displacement (mm) was obtained. Good correlation was also found in terms of the maximum strain fields between the computational and the experimental results, which were acquired by means of a fully coupled digital image correlation (DIC) system.

In another study, Zou et al. [44], performed experimental tests on two CF composite AFOs and one PP AFO: the devices were blocked in proximity of the calf straps, while the load (calculated as 1.3 multiplied the patient's weight), was applied on the sole of the AFOs by a cylindrical device with a loading rate of 8 mm/min. As it can be seen from figure 2.22, the same experimental boundary conditions were replicated in the finite element modeling environment. The friction coefficient between the cylinder and the AFO was assumed to be equal to 0.1. Good predictions were found in terms of force (N) vs displacement (mm). In the same article the energy return of the AFOs, as the area contained in the hysteresis loop, and the fracture analysis were quantified. The CF AFO showed better mechanical performance than the PP AFO, with a relative error of 3% in the prediction of the energy return ratio. The prediction was not accurate for the PP AFO.

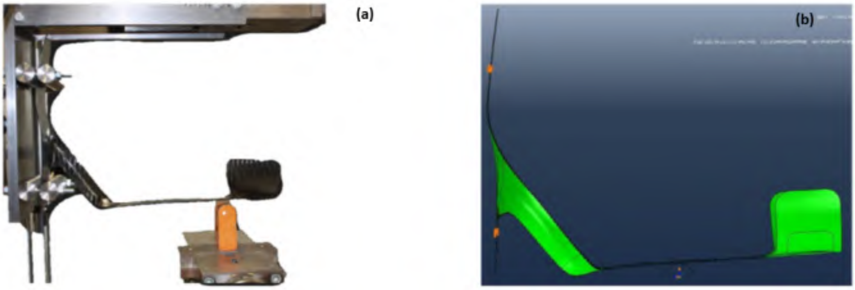

Figure 2.21: Experimental (a) and computational (b) setting by Stier et al. [117]

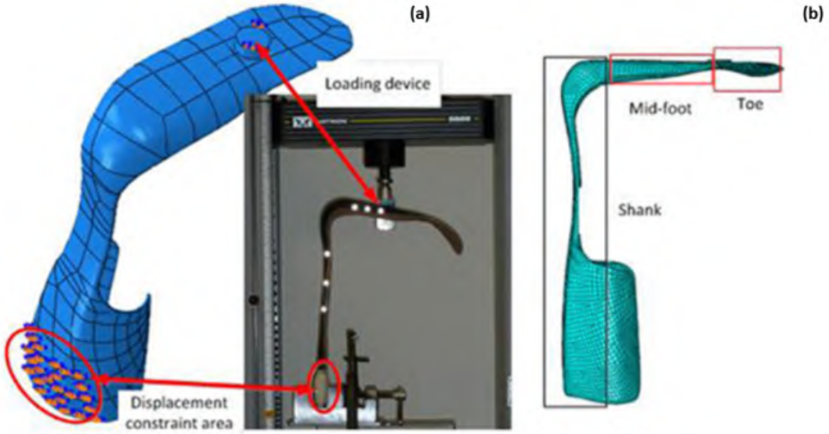

Figure 2.22: Bench top testing (a) and finite element modeling (b) setting by Zou et al.[44]

Similar boundary and loading conditions were used by Leone et al. [118] on a PP AFO: by increasing the experimental load the authors noticed the possibility of reaching structural failure by instability; replicating the situation computationally showed how model refinements in terms of material model and AFO geometry were needed to reach more predictive results. The last considered study was realized by Amerinatazi et al. [119], where they assessed the performance of an articulating AFO, containing a hinge made of Ni-rich NiTi alloy. The goal was to study the behavior of the AFO and particularly the hinge, since NiTi alloys are able to recover large amounts of deformation, compared to other materials. Therefore, a motion analysis was performed on a subject while walking with an AFO containing a NiTi spring and the results compared to those of a conventional stainless steel spring. Improved results were found for the NiTi spring, but additional evaluations were needed.

2.3 DISCUSSION AND CONCLUSIONS

In this chapter, the methodologies for the quantification of the mechanical properties of AFOs published by other research groups were presented and divided into three sub-categories based on whether experimental or computational methods or a combination of both were used.

Concerning the first category (table 2.1), many manual and automated setups were realized in the past years for the experimental evaluation of the stiffness of the AFOs, especially in the sagittal plane during plantarflexion and dorsiflexion; the goal of this approach was principally to mimic the behavior of the devices during the second rocker of gait, when the patient's foot is in complete contact with the ground and the forward progression of the body is obtained (see paragraph 1.3).

In general, a more complete approach would be reached if the AFOs were quantified in the three planes of motion (sagittal, frontal and transverse) ([94], [95], [96]), since it was identified in literature that the ankle joint has different axes of motion (see paragraph 1.2.2), in order to obtain a full representation of the behavior of the devices. In addition, a research group [75] determined the stiffness of the devices, not only in the sagittal plane, but also around the metatarsal-phalangeal (MTP) joint, which could be important for studying the propulsion effect of the AFO, during the push off phase of the gait (figure 1.17).

Typically, predefined ranges of motion were used: maximum values reported were 20 degrees in dorsiflexion/plantarflexion, 15 degrees in inversion/eversion and 15 degrees in abduction/adduction. As shown in table 2.1, using a surrogate limb is very common, since it can facilitate the fixation of the inferior (foot) part of the AFO to the ground and provide the specific loading to the superior (calf) part. In many cases, the fixation of the AFO was destructive ([78], [85],[86], [87],[90], [96],[97]): bolts and screws were employed, provoking damage to the devices, which made them not usable anymore. Two studies ([82], [93]), directly used the limb of the patients in their setups, without being functional analyses, which could be important for quantifying the impact of the human leg on the stiffness measures.

The differences between using a manual or an automated test rig are many: the use of a manual steering implies that many important parameters such as the speed and/or acceleration are not controllable, potentially affecting the behavior of the devices, i.e. if they are cyclically tested. Two studies ([93],[78]) tested AFOs using different speed values declaring that the stiffness of the devices was not affected, which seems unlikely due to the viscoelastic behavior of the materials employed for their realization.

Another important parameter, which was not always addressed, is the reliability of the setups, which plays a big role in the final outcome (table 2.1): the test-retest repeatability, the intra-tester and inter-tester variability measures provide useful information to assess the validity of the obtained results, especially if different partners involved in the project need to use them. In fact, these measures can assess if the experimental setups would provide reliable information in case of different applications, such as tests on different days or by different operators. Other parameters, such as the alignment of the AFO to the anatomical ankle joint, derived from the gait assessment of the patients, should not be neglected, as it helps to better mimic the real life conditions and to obtain reliable measures that can be used for validation purposes in the finite element environment, as done in this dissertation (see chapters 3 and 4). In general, the importance of the alignment was assessed by two studies: Takahashi and Stanhope [91], who evaluated how providing a load with a different orientation could influence the stiffness values and Gao et al. [83], who considered the impact of the alignment of the AFO with respect to the motor shaft.

Overall, the conduction of experimental tests on AFOs is time consuming and the construction of dedicated experimental setups is a complex and expensive operation. Computational analyses, instead, represent a useful tool which allows the prediction of important parameters of the AFOs in a faster manner (table 2.2). The main difficulty consists in finding the appropriate boundary and loading conditions that reflect the real life situations adequately. In addition, the choice of a suitable material model is critical, since most of the materials used (PA, PP or CF) exhibit viscoelastic properties, which need to be considered for a full description of the material behavior, especially under cyclic loading.

In general, most of the simulations in table 2.2 focused on the evaluation of the AFOs in the sagittal plane, usually providing a full constraint of the AFO sole and a load at the calf region or, vice versa, a full constraint at the calf region and a load applied at the metatarsal head region. None of the studies was considering the viscoelastic properties of the materials, which were typically modelled with elastic or elasto/plastic properties. Three studies ([101],[106],[107]) included a virtual representation of the patient limb in the simulations: this requires a significant increase in the modeling difficulty and the simulation time since other parameters, such as the material properties of foot, leg, and relative contact properties, need to be considered. At the same time this would allow to include the forces and torques exerted by the different parts on the AFO and study other pathologic conditions more specifically.

When talking about computational models, a mesh sensitivity analysis should always be included ([111],[119]), for assessing whether the obtained results are independent of the mesh size and density. Such a study was included in this dissertation (see Chapter 4) in order to find a simulation strategy that allows to evaluate the mechanical behavior of the AFOs accurately in a reasonable amount of time.

Moreover, the computational models need to be validated in order to prove they can address reliable information: this is accomplished by most of the studies listed in table 2.3; however, some of them require further refinements/evaluations for obtaining optimal results ([118], [119]).

Based on the analyzed studies, coupling advanced finite element models, constructed with accurate material properties and appropriate boundary/loading conditions, with experimental techniques would therefore represent the best adoptable strategy for the quantification of the AFOs mechanical properties, allowing the optimization of their manufacturing process before their physical realization by coupling them with optimization algorithms and possibly helping to gain better insight in their prescription process.

This strategy was used in the current PhD study; in particular, a novel approach was adopted for testing the AFOs in the experimental setup, by aligning them to the anatomical ankle joint, which location was previously measured during the gait assessment of the patients; this showed to be an important factor for obtaining reliable measures under several conditions, proven by quantifying the test-retest repeatability and the intra-tester and inter-tester variability of the setup. Therefore the experimental setup, based on the studies found in literature and described in Chapter 3, allows to obtain reliable measures of the AFO stiffness around the ankle joint in the sagittal plane and in a non-destructive manner; this setup will be further expanded in order to obtain a full characterization of the ankle mechanical properties of the AFOs in the three planes of motion (frontal, sagittal and transverse planes) plus around the MTP joint, which can permit to better study the impact of the neutral angle on the propulsion effect of the AFOs. Therefore, it will be the first experimental setup ever produced that will allow such an

AFO quantification and more details will be introduced in Chapter 5.
The adopted experimental approach enabled to obtain suitable measures for the comparison and relative validation of the finite element models of the AFOs, described in Chapter 4. The use of a PRF material model, which was never used in the past for representing the behavior of 3D printed AFOs, facilitated these tasks, by including the visco-elasto-plastic properties of the devices, carried out from samples of PA 12, the material used for manufacturing the AFOs [67]. Adopting different approaches for virtually representing the boundary and loading conditions imposed on the AFOs in the setup was then useful for understanding which representation is the most efficient for obtaining a prediction of the mechanical properties of the AFOs and create a methodology which can be coupled with optimization algorithms to design and realize more effective 3D printed AFOs. All these aspects will be discussed with more details in the next chapters.

II

Experimental tests on AFOs

Chapters

CHAPTER 3

DESIGN OF THE EXPERIMENTAL SETUP

This chapter provides an overview on the design of a new semi-automated experimental setup, developed in close collaboration with the orthopedic device company V!GO NV (Wetteren, Belgium), which allowed to obtain the results used for the validation of the finite element models of several patient-specific 3D printed AFOs, which will be introduced in Chapter 4. In particular, a detailed description of the different components of the setup, the ankle stiffness measures and the statistical analysis for assessing the reliability of the setup is provided.

3.1 INTRODUCTION

The construction of the setup required the contribution of different academic and industrial partners, employed in a multidisciplinary environment, where also doctors and certified prosthetic orthotists (CPOs) had an important role. Their support was important to decide which parameters and ranges of motion were relevant to be reproduced. This collaboration resulted in the creation of a new semi-automated experimental setup (figure 3.1 A-B) which allows the calculation of the stiffness around the ankle joint of patient-specific ankle foot orthoses over a maximal range of motion of 50 degrees (-25 degrees plantarflexion up to 25 degrees dorsiflexion) in the sagittal plane and in a non-destructive way. The main goal of the setup was to mimic the behavior of the AFOs during the second rocker of the stance phase of the gait, described in section 1.3, when the foot of the patient is in complete contact with the ground. The experimental setup is defined as semi-automated because, despite the measuring procedure being completely automated, clamping the AFO inside the setup is subjected to manual interaction.

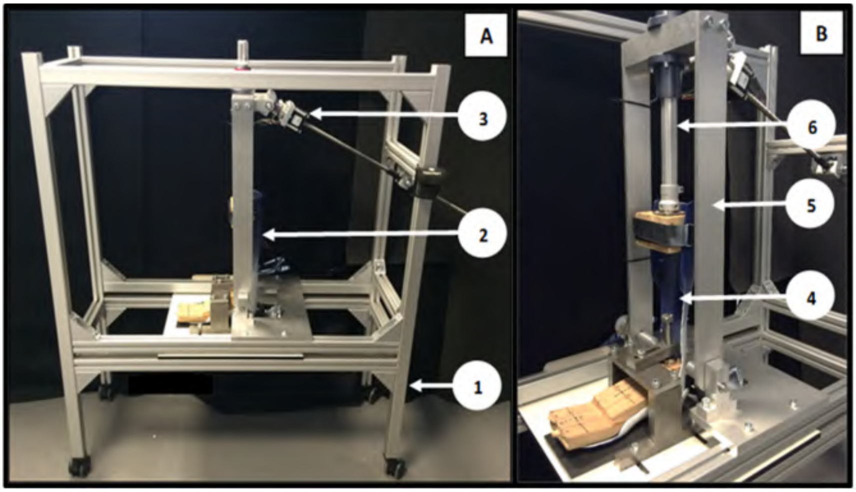

Figure 3.1: Overview of the experimental setup (A-B): 1. External frame; 2. AFO; 3. Linear Motor; 4. Closer view of the clamped AFO; 5. U-shaped frame; 6. Shank axis.

The design allows the alignment of the AFOs to the anatomical ankle joint, which location was derived from the gait assessment of each patient: a model of the patient leg (one for each patient-specific AFO considered), containing the anatomical landmarks, was milled from medium-density fibreboard (MDF) and inserted in the test rig to allow the alignment to the rotation axis of the setup. The MDF leg model was used, not only for alignment purposes, but also to constrain the AFOs in the setup and define the loading and boundary conditions to be implemented in the finite element environment, further described later. In particular, a system composed by a linear motor (HaydonTM Size 23), connected to a U-shaped frame, imposes the rotation of the AFOs around the anatomical ankle joint (figure 3.1 A-B). This is possible through the action of the spindle of the motor, which induces the plantar/dorsiflexion movements on the AFOs. In order to better describe the design of the setup, it was subdivided in several sub-assemblies, which will be introduced in the Section 3.2.
Prior to measuring the AFOs, a test object, called CalibrAFO, was created for evaluating an inox steel sheet in a "Instron Electropuls E10000" testing machine, which allowed to confirm the validity of the results coming from the experimental setup. In the same framework, the reliability of the setup was assessed by conducting a statistical analysis: the test-retest repeatability,

the intra-tester and the inter-tester variability were investigated showing that the ankle joint stiffness can be measured with high reliability (ICC = 0.94 – 1.00). Other parameters, such as the accuracy between different cycles during one AFO measurement or the recovery time, defined as the time needed for the AFO to recover its mechanical properties after an initial test, were investigated and also presented in this chapter.

3.2 DESIGN DESCRIPTION

The key design specification for the setup was the possibility of measuring the stiffness around the ankle joint of a wide variety of AFOs over patient-specific ranges of motion in the sagittal plane during the second rocker of the gait. The utilization of a patient-specific MDF leg model for each of the AFOs considered, which contains the anatomical landmarks of the patient, permitted to align the rotational axis of the setup to the anatomical ankle joint. A representation of the leg model is visible in figure 3.2 A-B.

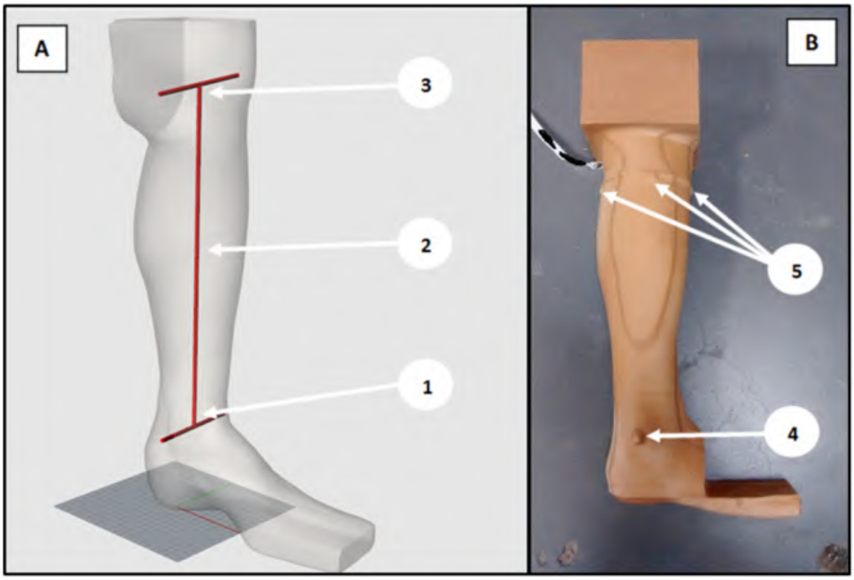

Figure 3.2: Drawing of the patient leg model (A): 1. Ankle axis, 2. Shank axis, 3. Knee joint centre; Patient leg model milled from MDF (B): 4. marker on the lateral malleolus for the ankle axis identification; 5. markers on the frontal, lateral, and posterior side for the shank axis identification.

The objective was to make a direct connection between the kinematics as defined and measured in the gait laboratory when walking both barefoot and with AFO, in mechanical testing of the AFO and in computer simulations. In the kinematic modelling (which is based on an adapted version of Plug-in-Gait from VICON Motion Systems), the knee joint centre (figure 3.2 A, item

3) is defined as the point between the centre of the medial collateral ligament on the joint line on the medial side of the knee and the popliteal groove on the lateral side of the knee (this marker placement is taken from that developed in the CP Cluster Protocol for 3D Marker placement within the CAMARC II EU Programme (1992) with the kinematic modelling methods outlined in Cappozzo et al. [94] and prior to this by Davis et al. [120]). The long axis of the shank is the line from the knee joint centre to the mid-point of the medial and lateral malleoli. Therefore, the plantarflexion-dorsiflexion axis of the ankle is defined as a line through the lateral malleolus in the plane containing the knee joint centre, the medial and lateral ankle (tips of malleoli) and which is perpendicular to the long axis of the shank. This definition is also taken from Plug-in-Gait which is a variant of the original model of Davis et al. [120] and has been widely used in clinical gait analysis for many years and continues to be seen as the reference standard.

Small surface markers are then placed on the patient's medial and lateral malleoli just prior to digital scanning of the leg. The STL file derived from the scan and used to mill the MDF model contains both the anatomical and technical references required for the alignment in the test rig. The axis of the shank is subsequently identified by the midpoint of the ankle reference points and the intersection of 2 lines from medial to lateral and posterior to anterior hemispheres on the mould of the leg just below the knee joint centre (these points being established by projections from the shank axis of the 3D scan of the leg in the AFO design software, developed by V!GO NV) (see (figure 3.2 B).

The 3D scanning of the leg of the patient is done by using the software Artec Studio®, in combination with the acquisition of standard physical measures such as the height of the fibula, heel width, ankle width, meta width, foot length etc. and when the pathology of the patient is too severe, even a plaster cast is taken and eventually scanned. Once the patient-specific scans are obtained, they are virtually corrected using an orthopedic software called Rodin 4D, which allows to obtain the STL files of the patients leg. This STL file is used for two purposes: firstly, to realize the MDF blocks of each patient-specific leg by using a five axes milling machine and secondly as a starting point in the computer aided design environment where a combination of three programs (3-Matic® (Materialise N.V.), Solidworks® (Dassault Systemes) and Rhinoceros® (Robert McNeel & Associates)) allow to obtain the design of the AFO. More details can be found in the study of Deckers et al. [50].

After the milling procedure, the MDF leg model of the patient is cut in three parts: a calf, an ankle and a foot part, in order to allow the fixation of the AFOs in the setup and not to hinder their deflection, which is imposed by the experimental setup (figure 3.3).

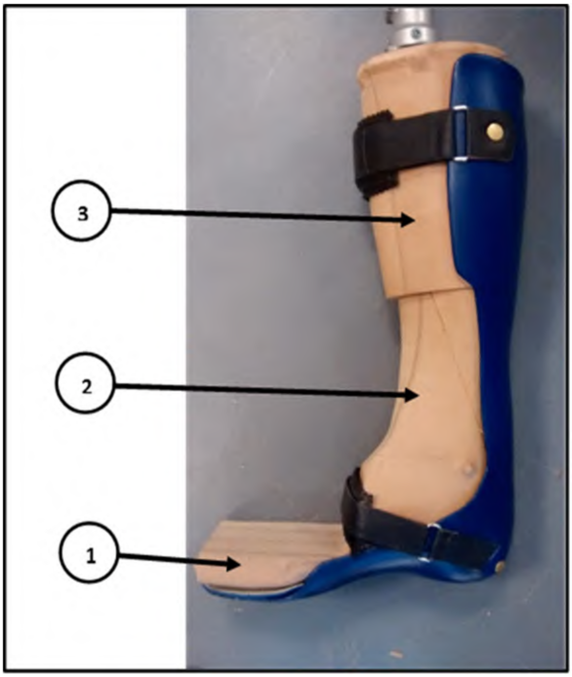

Figure 3.3: MDF leg model of the patient already cut in three parts (foot (1), ankle (2) and calf (3)) coupled with an AFO to be placed inside the setup for the alignment to the rotation axis.

The calf part, in fact, is used for the connection with the shaft of the setup, which represents the shank axis and is strapped to the AFO. The ankle part is used for the alignment of the shank axis and the plantar/dorsiflexion axis of the ankle, during the clamping of the AFO in the test rig. To facilitate the alignment at the ankle joint, the test rig was designed with two pointers, which can be extended or retracted depending on the dimension of the block. When the alignment is done, the ankle part is removed. The foot part is then used for clamping the sole section of the AFO: a compression screw clamps the AFO sole section between the MDF foot block and the test rig base plate. The tightening of the screw might introduce unwanted values of pressure on the AFO; in the ideal case these values should be equal to zero thus to have the AFO in an unstressed condition, but this is not always possible; therefore, a load cell (SensyTM 2712), which location will be defined later in this section, detects the eventual values of pressure and, if they are too high, the clamping will be regulated in order to lower them. If needed, metal sheets of various thickness are inserted below the AFO to ensure the flexion-extension axis alignment in the test rig irrespective of the AFO size. The clamping system is non-destructive and requires no special preparation or AFO surface treatment (figure 3.4).

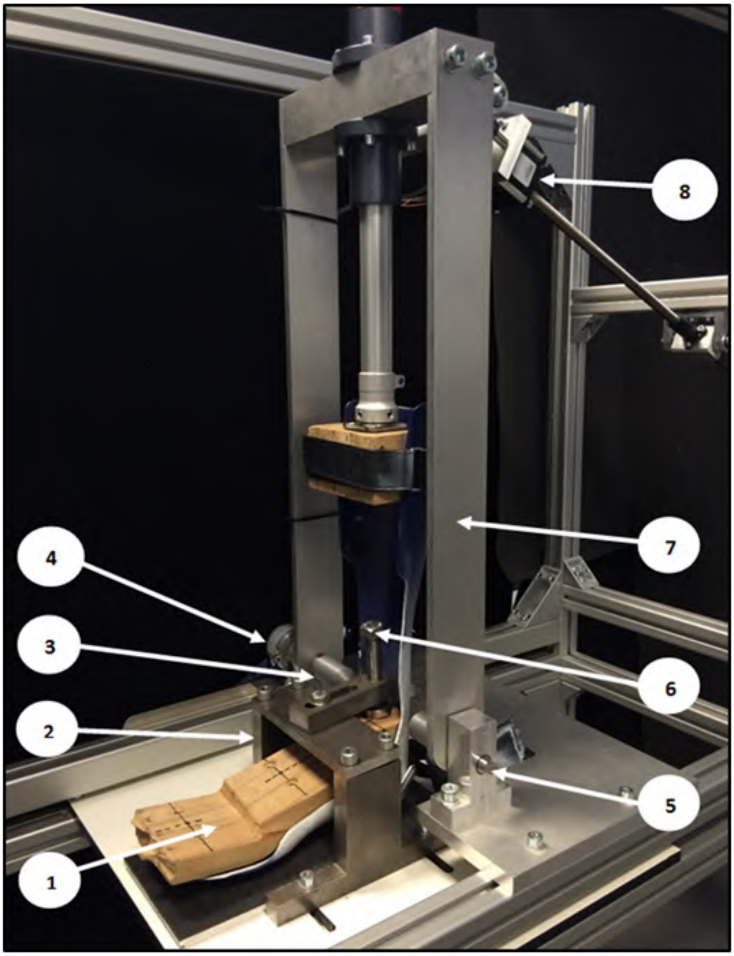

Figure 3.4: Detail of the experimental setup: 1. MDF foot block; 2. Clamping system; 3. Pointer for the ankle axis alignment; 4. Incremental optical encoder; 5. Ankle rotation axis ; 6. Compression screw; 7. U-shaped frame; 8. Linear motor.

Once the AFO is mounted in the test rig, plantarflexion and dorsiflexion can be applied to the orthosis: a specific range of motion is imposed according to the information coming from the previous gait assessment of the patients; therefore the design of the setup allows deflections up to 25 degrees in both dorsiflexion and plantarflexion, starting from an initial neutral angle of 0 degrees. The neutral angle represents the configuration of the AFO when no external moment is applied [75] and, depending on the produced AFO, can have a certain value in dorsiflexion or plantarflexion. In common with much of the published gait assessment data, plantarflexion is indicated with negative angles and dorsiflexion with positive angles (table 2.1).
As visible from figure 3.4, the movement is applied by the linear motor

through a U-shaped frame, which connects the shaft of the shank axis with the ankle rotation axis of the setup. The U-shaped frame is part of a complex called 'ankle rotational 1'. As previously anticipated, the realization of the test rig required its subdivision in six different sub-assemblies called: frame 1, frame 2, ankle horizontal, ankle rotational 1, ankle rotational 2 and ankle rotational 3. This subdivision was used for facilitating the design and the description of the setup and will be shown in the next figures.
In figure 3.5, a representation of frame 1 is visible: it is the main structure of the setup, realized through a series of bars of different length, which are connected using angle brackets, chosen for sustaining the high loads applied to the AFO during the movements and the weight of the other sub-assemblies. In frame 1, the clamping system plus the installation of four castors, that allow the easy transportation of the setup, are also contained.

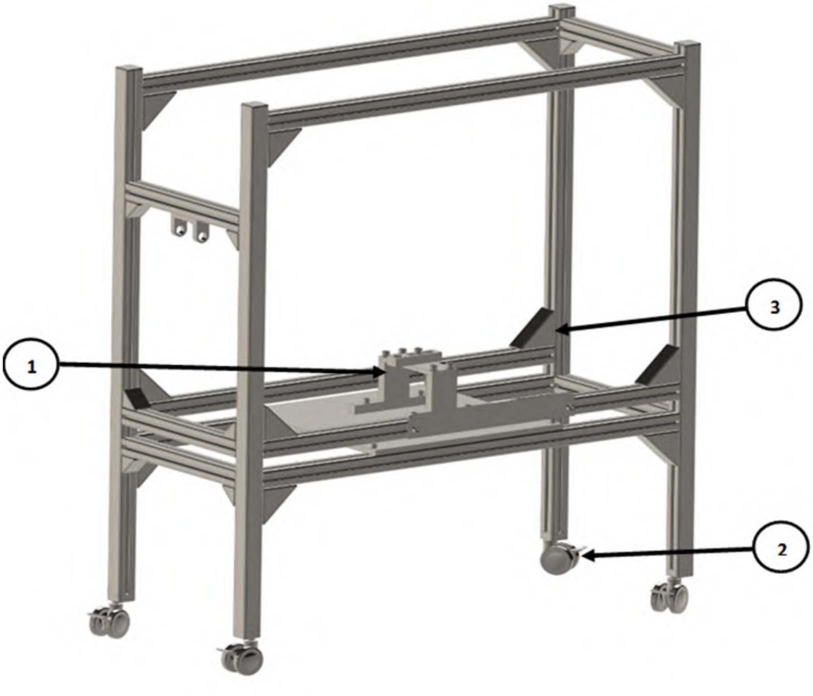

Figure 3.5: Visual representation of frame 1: 1. Clamping system; 2. Castor; 3. Angle bracket.

Frame 2 (figure 3.6) consists of a few components which allow for the connection of the linear motor, used to provide the rotation to the AFO, with frame 1. In particular two shafts, with respective bearings, facilitate the advancement/retraction of the spindle of the linear motor in the nut, which is secured to an aluminum block by screws.

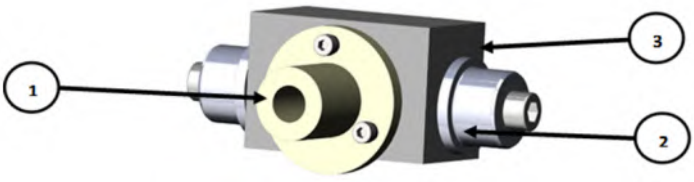

Figure 3.6: Representation of frame 2: 1. Nut for the spindle of the linear motor; 2. Bearing applied around the shaft; 3. Aluminum block.

The linear motor is then fixed to the complex called ankle rotational (figure 3.7), which is composed of three other sub-assemblies, respectively called as ankle rotational 1, 2 and 3. In figure 3.7, it is possible to notice how a modular 3D printed AFO is fixed to the shank axis of the setup. The other extremity of the shank axis is free. The sole of the AFO is immobilized on the baseplate of the frame 1 by using the MDF foot block of the patient leg model.

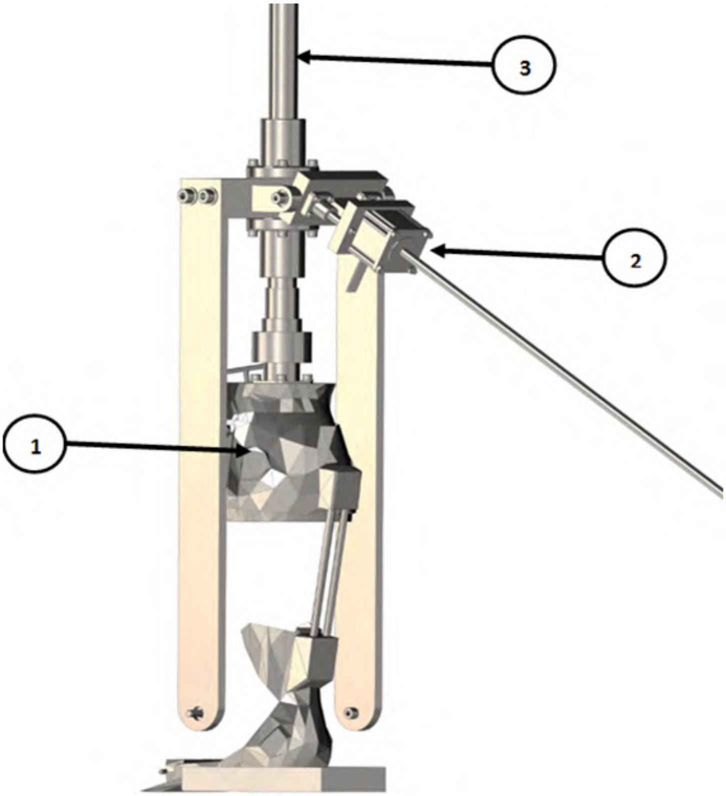

Figure 3.7: Representation of the ankle rotational complex: 1. AFO; 2. Linear motor; 3. Shank axis of the setup.

By having a closer view (figure 3.8) on the drawings of the two sub-assemblies called ankle rotational 2 and 3, it is possible to see the attachment of the linear motor (HaydonTM Size 23 with a spindle length of 750 mm) to an aluminum block, which is connected to two cylinders that slide inside a second aluminum block. In order to acquire the force acting on the AFO, a load cell (SensyTM 2712), is placed between the two aluminum blocks. Two bearings located on the two cylinders and parallel to the load cell make sure that only the forces acting along the same axis of the load cell are acquired. The second aluminum block is then connected to the U-shaped frame of the ankle rotational 1 sub-assembly, forming a hinge mechanism, that contribute to provide the load generated by the motor to the AFO. A detail picture of the mechanism is contained in figure 3.9.

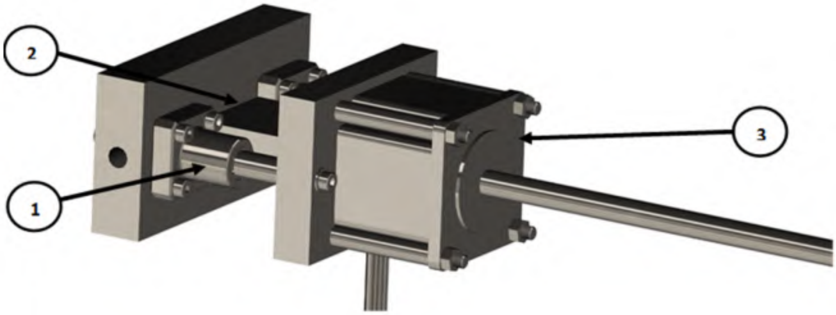

Figure 3.8: Closer view on the motor-load cell complex, composed by the sub-assemblies called ankle rotational 2 and 3: 1. Bearing applied around the sliding cylinder; 2. Load cell; 3. Linear motor.

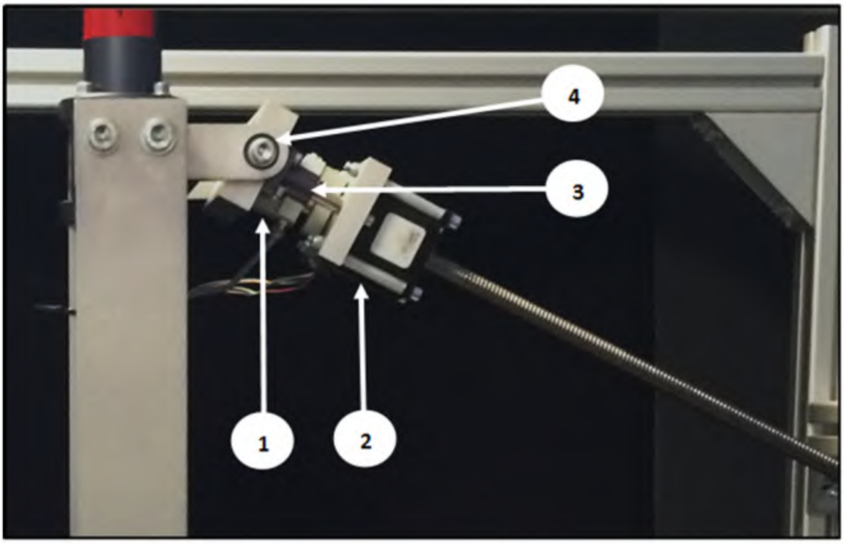

Figure 3.9: Hinge mechanism of the motor-load cell complex and the ankle rotational 1 sub-assembly: 1. Load cell, 2. Linear motor, 3. Bearing applied around the sliding cylinder; 4. Hinge mechanism.

As anticipated, the ankle rotational 1 sub-assembly contains the U-shaped frame (figure 3.10), which connects the shank axis of the setup to the ankle rotation axis (figure 3.4). The action of the linear motor drives the rotation of the U-shaped frame around the ankle rotation axis. At the same time the shank axis, can slide up and down through the presence of two bearings, which prevent excessive loading on the AFO.

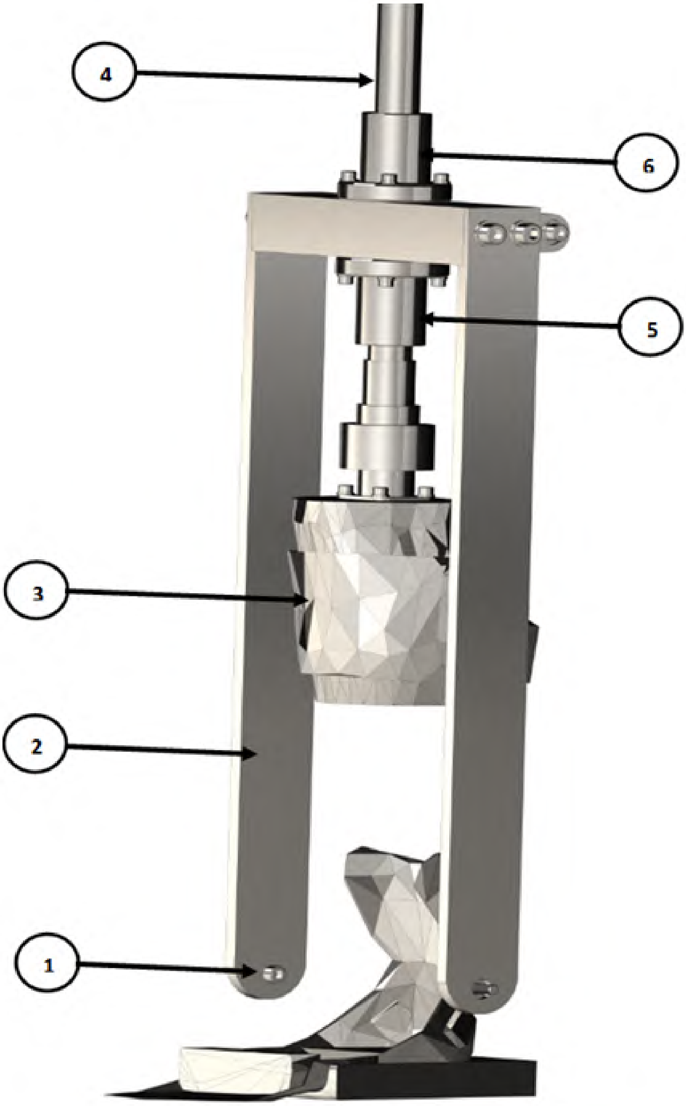

Figure 3.10: Overview of the ankle rotational 1 sub-assembly together with a virtual representation of a 3D printed AFO: 1. Attachment for the ankle rotation axis; 2. U-shaped frame; 3. AFO; 4. Shank axis of the setup; 5. Bearing 1; 6. Bearing 2.

The last sub-assembly is called ankle horizontal (figure 3.11), which sustains the ankle rotational 1, 2 and 3 sub-assemblies and is directly fixed onto the frame by t-slot nuts and hexagonal screws. By untightening them, it is eventually possible to horizontally slide the sub-assemblies for better matching the location of the ankle rotation axis. In the picture is also visible the attachment of an incremental optical encoder (KublerTM 5020) around the ankle rotation axis in order to detect the angle variations during the AFO deflection. Before the experiment, the neutral angle is also measured, by means of a digital goniometer (Toolcraft 816141) to give absolute angles from the relative angles measured by the optical encoder.

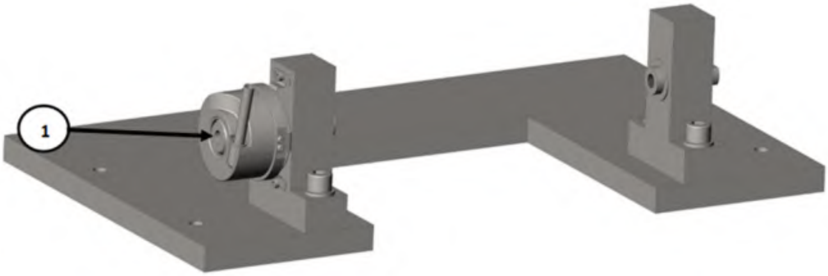

Figure 3.11: Overview of the ankle horizontal sub-assembly: 1. Incremental optical encoder attached around the ankle rotation axis.

A custom written LabView code allows the operator to adjust the angular speed, defined in degrees per second and the relative acceleration, in degrees per square second. The code also permits to regulate the patient-specific range of motion for each AFO, by defining the maximum plantarflexion and dorsiflexion angles, and the number of continuous cycles to be applied. Data collection and initial visualization of the data are also performed within the LabView environment. Besides the measurement curve, a calibration curve needs to be recorded for every AFO in their specific range of motion. In fact, the gravitational effects, given by the weight of the MDF blocks and the hardware of the setup, can have an impact on the measurements. Therefore, they are quantified for each AFO in their specific range of motion, when the AFOs are not secured in the setup, and subtracted from the measurement curves by using an automated python code, further described in Section 3.3.

3.3 POST-PROCESSING

The AFO ankle stiffness was defined by Bregman et al. [75], as the moment around the ankle joint exerted by the AFO per degree of ankle joint rotation. Therefore, once the measurement and calibration curves of the AFOs are recorded, the moment values need to be derived in order to calculate the stiffness. These values are not directly calculated, since the load cell of the setup can only acquire the forces exerted by the AFO. The derivation of the moment values is possible through a series of formulas, which are used to describe the setup during the plantarflexion and dorsiflexion movements (figure 3.12). Providing a description of the used quantities in the formulas is necessary (figure 3.13): L1 is defined as the length of the U-shaped frame and measures 587.5 mm, L2 is the distance between the hinge of the load cell-motor complex and the U-shaped frame and measures 75 mm, X and Y, which are equal to 502 mm and 355 mm, are respectively the horizontal and the vertical distances between the rotation axis and the nut of the motor; αin, instead, represents the neutral angle. As visible from figure 3.12, the values of many angles are defined; they can be calculated as follows:

$$\beta = \arctan\left(\frac{L_2}{L_1}\right) \qquad \alpha = \alpha_{in} + \Delta\alpha \qquad \varepsilon = \alpha - \beta$$

$$\delta = \pi - \gamma - \left(\frac{\pi}{2} + \varepsilon\right) \qquad \gamma = \arctan\left(\frac{S_y}{S_x}\right)$$

For the calculation of λ it is necessary to calculate the distances Sx and Sy which are equal to:

$$Sx = \sqrt{L_1^2 + L_2^2} * \sin(\varepsilon) + X \qquad Sy = \sqrt{L_1^2 + L_2^2} * \cos(\varepsilon) - Y$$

This leads to the formula of the moment M, where F is the measured force by the load cell:

$$M = \sqrt{L_1^2 + L_2^2} * \cos(\frac{\pi}{2} - \delta) * |F|$$

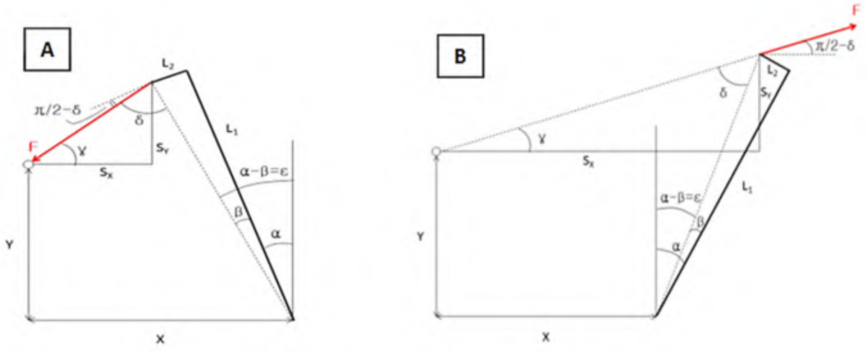

Figure 3.12: Free body diagrams of the experimental setup during plantarflexion (A) and dorsiflexion (B).

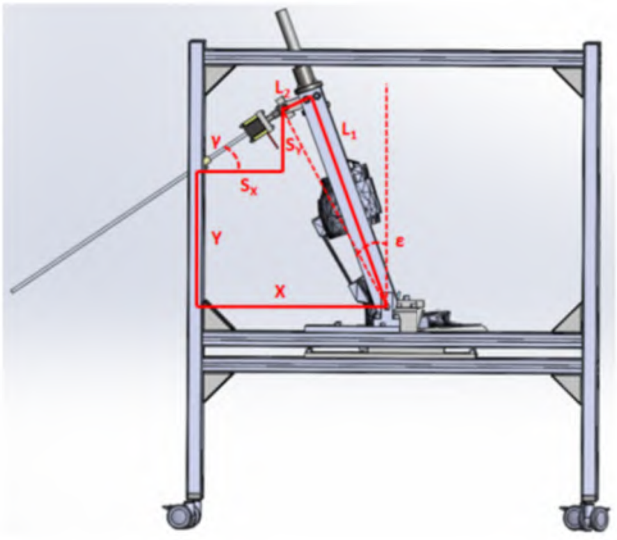

Figure 3.13: Representation of the quantities used in the formulas for the calculation of moment

By using this set of formulas it is possible to obtain the description of the behavior of the AFOs in terms of angle vs. moment curves. In order to speed up the calculation process they are inserted in a custom realized python script, which allows the calculation of the stiffness by linear fitting in four different quadrants: plantarflexion loading (PL), plantarflexion unloading (PU), dorsiflexion loading (DL) and dorsiflexion unloading (DU), as shown in figure 3.14. This is done because the AFOs generally behave differently in the four quadrants, due to their shape. It's also possible to notice the presence of hysteresis: the hysteresis area represents the dissipated energy from potentially two sources; as heat during the deformation (loading) and the recovery phases (unloading) which is dependent upon the strain rate employed to deform the devices [121] constructed from PA 12, which has visco-elasto-plastic properties [67]; and by the friction present between the AFO and the test rig and between the components of the test rig itself.

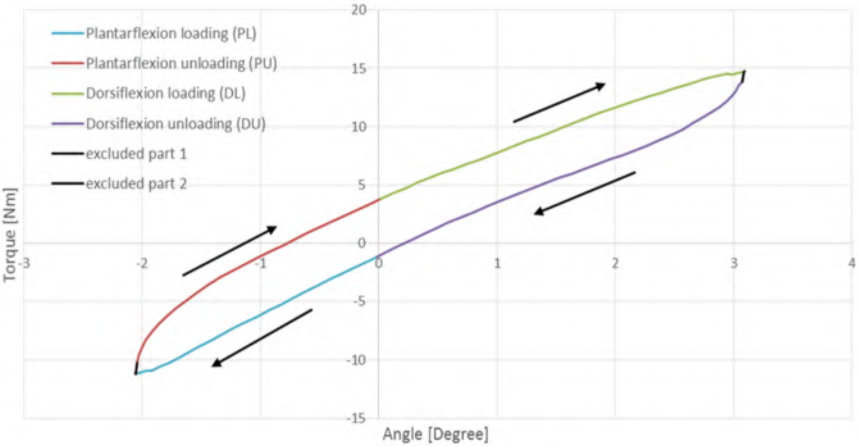

Figure 3.14: Example of the stiffness calculation in the four quadrants on filtered data: plantarflexion loading (PL), plantarflexion unloading (PU), dorsiflexion loading (DL), dorsiflexion unloading (DU) and the excluded parts 1 and 2.

The operational speed of the setup is not constant for the entire cycle, but there are zones, corresponding to the maximum plantarflexion and dorsiflexion angles, where the inversion of the movement direction is not instantaneous, but requires a certain time depending on the user defined acceleration. The data gathered during these de/acceleration phases are always excluded from further use, since they could introduce errors on the effective stiffness measures (figure 3.14). The calculation of these zones is possible through the quantification of the derivative of the angle. An example is visible in figure 3.15: when the algorithm finds that two consecutive values of the derivative are equal, it means that no variation of the angle has happened and the first value is then considered as the end of the loading phase; conversely, when the value of the derivative changes, it is considered as the beginning of the unloading phase.

Another aspect to consider in the post-processing is the need of filtering the experimental data from the noise produced during the measurement (figure 3.16). This is solved by applying a 4th order low-pass Butterworth filter with a cut off frequency of 0.2 Hz, while the sampling frequency was 10 Hz. Other studies also used this type of filtering in the past, such as ([81], [83]).

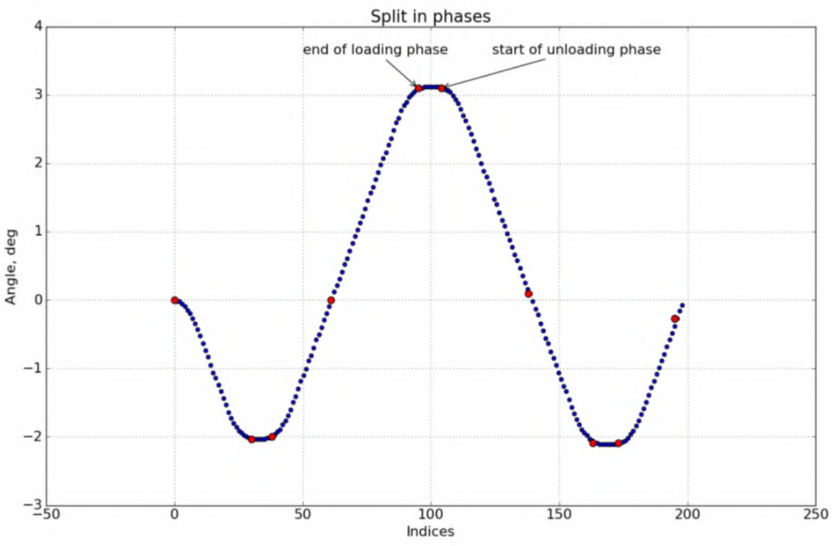

Figure 3.15: Example of the calculation of the derivative of the angle, which is used to mark the beginning and the end of the loading and unloading phases: in this case the end of the loading phase and the beginning of the unloading phase are shown.

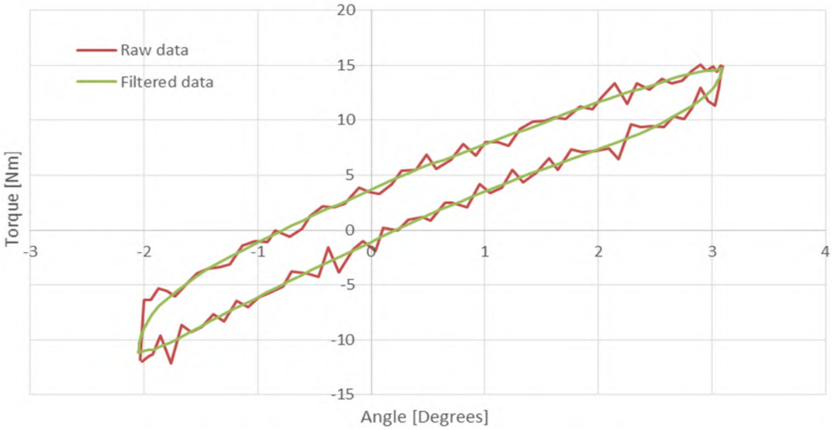

Figure 3.16: Example of the application of the filtering on the raw data of a 3D printed AFO and the successive filtered data.

Therefore, after splitting the angle vs. torque curves in the four compartments, the ankle stiffness of the device is calculated: the slope of the curve in each quadrant represents the effective stiffness of the AFO in that specific area. This procedure is applied to every cycle of the measurement, which are then averaged to obtain one common value for each quadrant. Because of the Mullins effect [122], the first cycle is always excluded from the calculations. The Mullins effect is the term used to define the stress softening of the devices: this is a common phenomenon in elastomers, characterized by the decrease of the stress during the unloading phase in comparison to the stress during the loading phase at the same strain (figure 3.17). During tests with constant displacement amplitude, as in our case for the AFOs loaded for a specific range of motion, the stress decreases during successive loading cycles; this is particularly visible from the first to the second cycle and it becomes negligible afterwards. Therefore the decision of excluding the first cycle. The investigation of the accuracy between the other cycles is presented in Section 3.7.1.

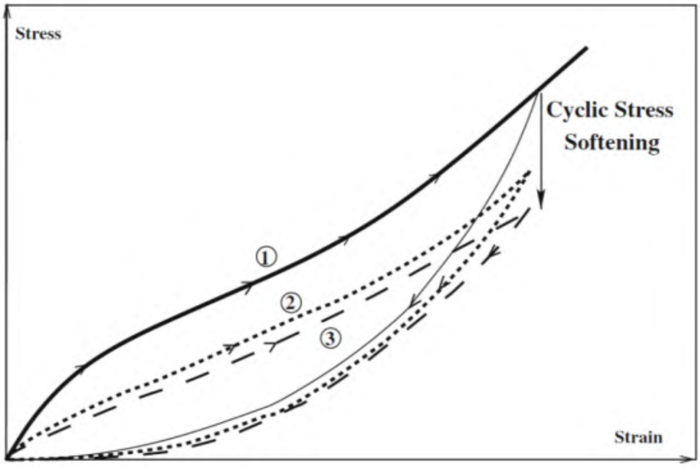

Figure 3.17: Representation of the Mullins effect during a constant displacement amplitude (adapted from [122]).

3.4 CalibrAFO

Before starting the experimental evaluation of the AFOs, a test object called 'CalibrAFO' was designed: an inox steel sheet, which owns rather pure elastic material properties, is held inside two steel clamps and attached to the test rig for testing figure 3.18.

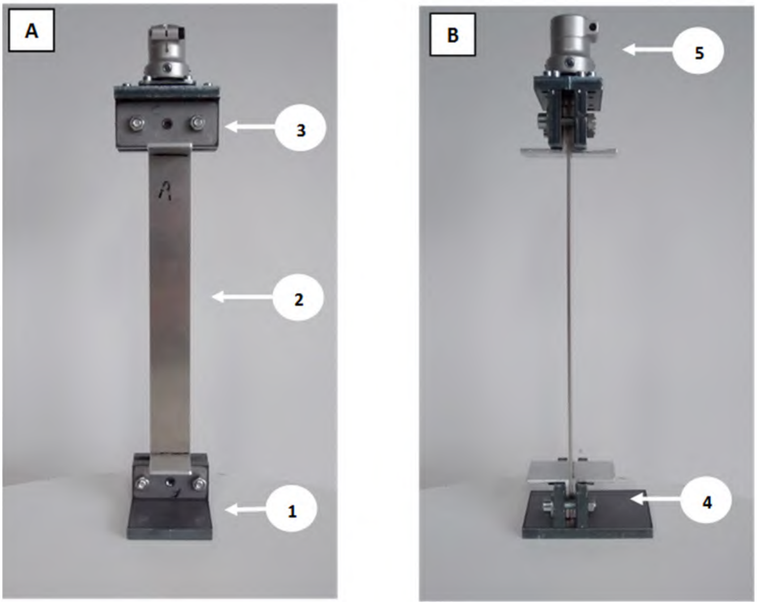

Figure 3.18: Front (A) and side (B) view of the CalibrAFO device: 1. bottom clamp; 2. inox steel sheet; 3. top clamp; 4. clamping position; 5. attachment component to the shaft of the setup.

The inox steel bar has the following dimensions: length of 379 mm, thickness of 3 mm and width of 40 mm. The bottom and top clamps of the device are composed of an anterior and a posterior part which are tightened by bolts. The contact between the inox steel bar and the clamps is enhanced by using aluminum plates in between. After securing the inox steel bar between the clamps, the device needs to be inserted inside the test rig: firstly the connection with the shaft of the setup is made through the components shown in figure 3.18 B. After the device is aligned with the rotation axis of the setup (it passes through the middle of the steel sheet), the screw of the clamping system is applied in order to completely block it, as done for the AFOs MDF blocks: in fact, the superior surface of the bottom clamp (figure 3.18 B, item 4) is compressed by the screw of the clamping system on the base plate of the frame, constraining the movements of the device. Once these precautions are taken, the measurements on the inox steel bar can start; also in this case, a calibration curve is recorded for excluding the gravitational effects caused by the test rig and the top clamp on the measurements.

3.5 Validation of the CalibrAFO results

The objective of using the CalibrAFO device was to validate the results coming from the test rig by using an easily applicable and fast approach. For this purpose, additional experiments were conducted on a "Instron Electropuls E10000" testing machine (Dynamic linear force capacity = ± 10 kN, accuracy 0.005 % of load cell capacity; more technical details can be found on www.instron.us) by using a custom made mounting frame for the clamping of the inox steel bar, as shown in figure 3.19.

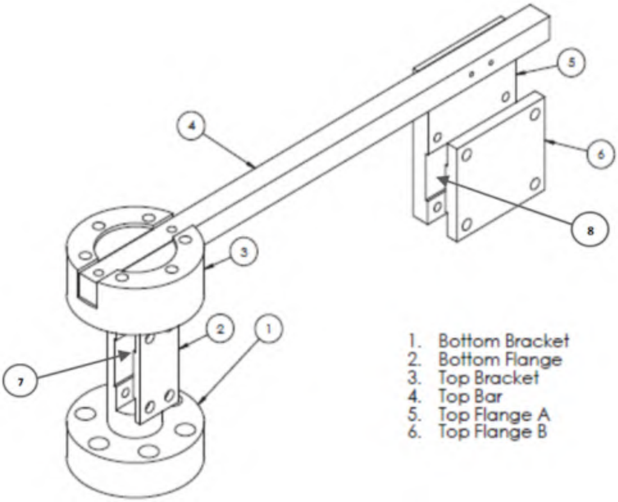

Figure 3.19: the mounting frame used for the experiments on the inox steel bar inside the 'Instron Electropuls E10000' testing machine. The inox steel bar is clamped inside the bottom bracket (1) and flange (2) inferiorly and the top flanges A (5) and B (6) superiorly (location indicated as 7 and 8). Bottom and top brackets are not connected to each other, but they are accurately aligned in order to center the rotational actuator and the load cell on the same axis.

The mounting frame allows the fixation of the inox steel bar through bottom and top flanges, which are connected by a stiff and thick steel bar, called top bar (figure 3.19, item 4), which has a higher Young's modulus compared to the inox steel sheet. Besides the top bar, all the other components of the mounting frame are realized in aluminum. The deflection is applied through the top bracket (figure 3.19, item 3), which is connected to the rotational actuator of the Instron testing machine, while the bottom bracket (figure 3.19, item 1) is screwed onto a stationary load cell for the direct measurement of the torque values. Bottom and top brackets are not connected to each other, but accurately aligned in order to center the rotational actuator and the load cell on the same axis. As shown in figure 3.10, the shaft of the experimental setup can slide up and down through the presence of two bearings, in order to prevent excessive loading on the AFO. This is partially replicated in the custom mounting frame of the Instron testing machine by loosening the screws between the top bar and the top flange A, thus to allow the spring to shorten or lengthen depending on the direction of the deflection. Another difference between the two settings was that, for the custom mounting frame indicated in figure 3.19, the rotation axis was passing through the center of the bottom and top brackets while for the test rig (figure 3.1 A-B) it was located at the end of the bottom clamp, resulting in a difference of 25 mm. In order to compensate this difference, steel sheets were applied under the CalibrAFO device during the measurements in the test rig, in order to have a rotational axis with the same height in both configurations. In figure 3.20, the comparison of the results coming from the two configurations is reported, with the inox steel sheet tested over a range of 10 degrees in plantarflexion and dorsiflexion.

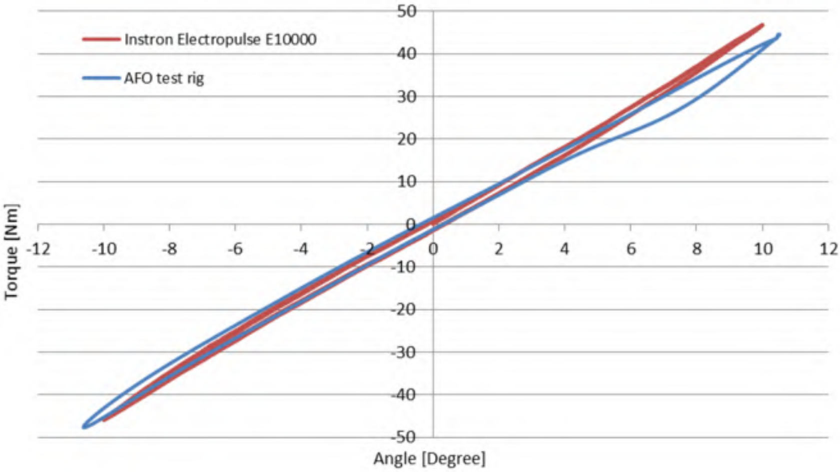

Figure 3.20: Comparison of the results between the experimental setup and the 'Instron Electropuls E10000' testing machine.

The results obtained from the two testing machines show comparable results, which indicate how the test rig can be applied for the quantification of the stiffness of the AFOs around the ankle joint. However, some differences can be noticed, which are believed to be related to the clamping (boundary) conditions: for example, the clamping in the test rig is provided by a compression screw on the superior surface of the bottom clamp (figure 3.18), which can expose the device to a certain lifting, when a dorsiflexion movement is applied. During plantarflexion, this phenomenon is not present, since a perfect contact with the base plate of the setup is provided, because of the action of the compression screw. In the mounting frame of the Instron testing machine, instead, the clamping system was designed to be symmetrical and to firmly hold the inox bar. Other factors, such as the frictional effects within the testing devices could also have an impact on the obtained measures.

These results, obtained on the inox steel bar, can be assumed to be valid and extendable to the AFOs; however, further tests should be realized in both setups by directly using AFOs, which have different material properties than the inox steel bar. This requires to mimic the same boundary/clamping conditions in both setups, since, as we observe in figure 3.20, these may introduce some differences in the results. At the same time, this would require the realization of a custom made clamping system for the Instron Electropulse E10000 testing machine, that will be only used for a short time period and that can be both expensive and time consuming. For these reasons, the current methods were applied keeping its limitations in mind.

3.6 RESULTS

After the validation of the experimental results obtained by the inox steel sheet, an experimental campaign on different 3D Printed AFOs was conducted. The goal was to study the stiffness around the ankle joint of the patient-specific devices, thus to provide further information that could be potentially used during the prescription process. In addition, since the experimental setup would also be used by the other partners within the research project (see paragraph 1.7.1), a statistical analysis was conducted to assess the reliability of the measures in terms of the test-retest, intra-tester and inter-tester variability. These processes are extremely important since they are able to prove whether the experimental setup could be applied under several working and control conditions.

3.6.1 Stiffness

In this study, five subjects (four patients and one unimpared subject) with different anthropometric data were selected (table 3.1); the patients were affected by the following disorders: trauma, neuro-muscular disorder and/or cerebral palsy. Five 3D printed AFOs were then used for the quantification of the stiffness around the anatomical ankle joint. They were indicated as AFO A, B, C, D for the patients and E for the unimpared subject and respectively have an EU foot size of 32, 35, 37, 45 and 42. AFOs A, B, C and D are made of three parts [50]: a foot and a calf part made in Polyamide 12 (PA 12) are connected by two carbon rods (6 mm diameter for AFOs A, B and C; 8 mm for AFO D), as shown in figure 3.21. AFO E is entirely 3D printed in PA 12, as in figure 3.3. All the devices are made for a right foot.

Table 3.1: Anthropometric data of the analyzed subjects.

AFO	Mass [Kg]	Height [m]	Gender	Age
A	25	1.33	F	10
B	26.5	1.39	M	10
C	58	1.57	F	13
D	93.5	1.85	M	38
E	72	1.76	M	33

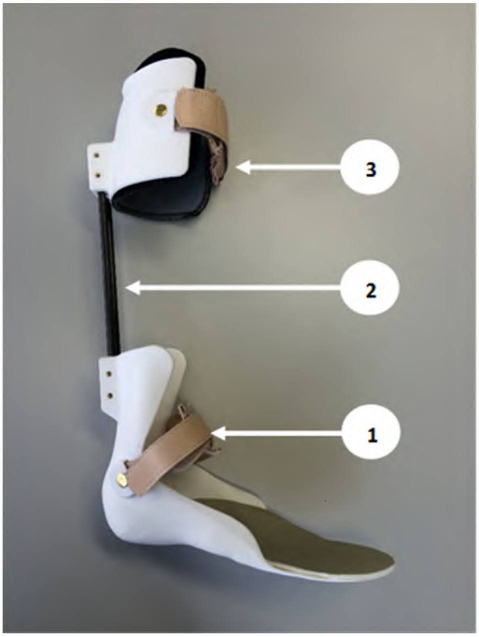

Figure 3.21: Modular design used for four of the AFOs tested: a foot (1) and a calf (3) part made in PA 12 are connected by two carbon rods (2) of 6 or 8 mm diameter.

An appropriate range of motion was selected for testing the devices (table 3.2): before the experimental trials, all the AFOs were subjected to gait assessment while the subjects were walking with them in order to obtain the ranges of motion to be used in the test rig. This feature, together with the alignment of the motor rotational axis to the anatomical ankle joint, allows to obtain the best approximation of the AFO stiffness felt by the subject during the second rocker of the gait. In general, during the measurement, five cycles are recorded plus one calibration curve at the speed of 1 degree/s.

Table 3.2: AFOs ranges of motion.

AFO	Plantarflexion [°]	Dorsiflexion [°]
A	-2	6
B	-6	3
C	-6	10
D	-7	9
E	-2	4

In figure 3.22, it is possible to notice the behavior of the different 3D printed AFOs in terms of the averaged ankle stiffness during a single measurement. AFO D resulted to be the stiffest AFO in both plantarflexion and dorsiflexion, while AFO E the most flexible. All the AFOs show the presence of hysteresis, due to the viscoelastic behavior of the devices and the friction within the setup.

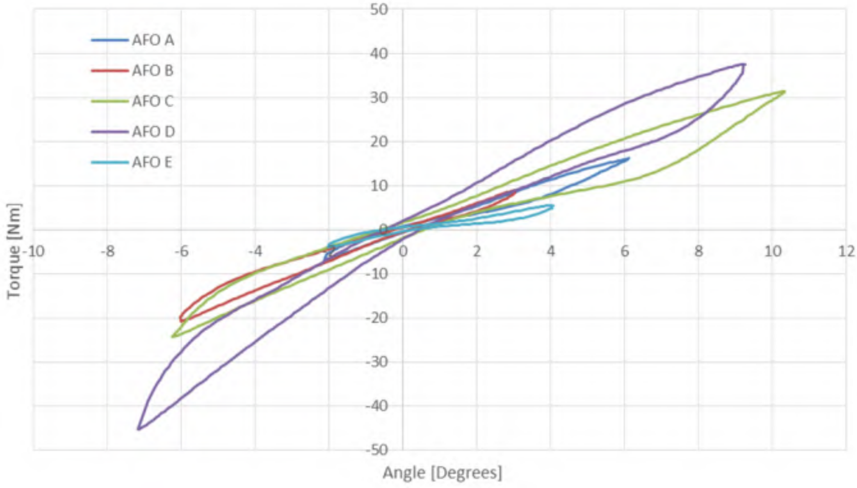

Figure 3.22: Ankle stiffness graphs during dorsiflexion and plantarflexion for the five 3D printed AFOs.

The graphical trend of figure 3.22 is confirmed by the calculation of the ankle stiffness values, averaged between cycles, in the four quadrants, where again AFO D and AFO E are respectively the stiffest and most flexible AFOs (figure 3.23). This can be explained by the fact that the patient wearing the AFO D owns the highest mass compared to the other subjects (table 3.1), while the AFO E was worn by an unimpared subject who wasn't prescribed with an AFO.

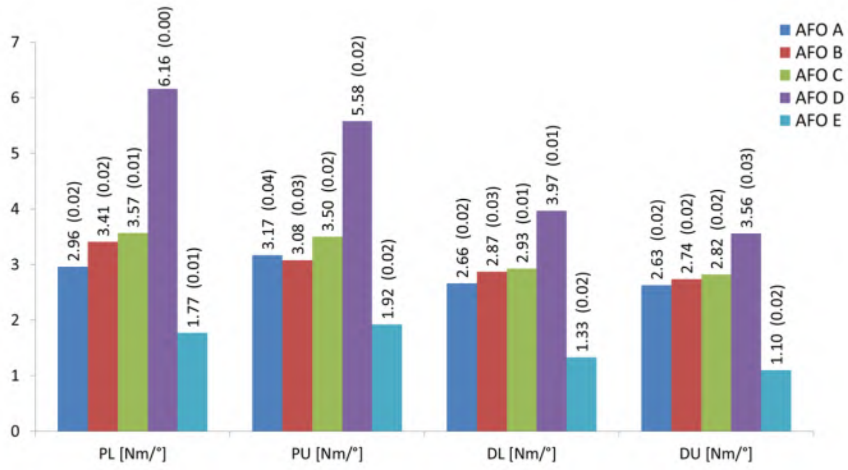

Figure 3.23: Averaged ankle stiffness values calculated during dorsiflexion and plantarflexion for the five 3D printed AFOs. In brackets, the standard deviation is indicated.

These results indicate that the test rig is able to measure the stiffness around the anatomical ankle joint of several patient-specific AFOs in a non-destructive manner. However, in order to prove the ability of the test rig to provide reliable stiffness measures under different working conditions, additional statistical tests are demanded.

3.6.2 Statistical analysis

As anticipated, a statistical analysis was performed to assess the reliability of the experimental setup to measure the ankle stiffness of the patient-specific AFOs: AFO A, B, C and D were used to investigate the influence of three sources of error: first of all, the test-retest repeatability of the setup was assessed by using three repeated measures on the AFO performed by the same operator with the AFO remaining fastened inside the setup between test re-test trials, in order to exclude the AFO mounting process; then, the intra-tester variability, for evaluating the effect on the measures when the AFOs are removed and reinserted in the setup by the same operator on different days and the inter-tester variability, which required different measures on the same AFO by two different operators, with the removal of the AFO from the test rig between repeat tests. The calculation of the percentage differences in the three cases showed that the maximal error values are never higher than 2 % for the test-retest repeatability, 5.26 % for the intra-tester variability and 5.65 % for the inter-tester variability (table 3.3), (table 3.4), (table 3.5).

Table 3.3: AFOs test-retest repeatability, with measures expressed as absolute values and percentage difference from the mean.

AFO A								
Test	**PL [Nm/°]**	**PL [%]**	**PU [Nm/°]**	**PU [%]**	**DL [Nm/°]**	**DL [%]**	**DU [Nm/°]**	**DU[%]**
1st	2.96	0.56	3.17	0.01	2.66	0.78	2.63	0.68
2nd	2.97	0.56	3.16	0.21	2.64	0.01	2.60	0.59
3rd	2.99	0.62	3.18	0.20	2.62	0.77	2.61	0.09
Mean	2.97		3.17		2.64		2.62	
SD	0.02		0.01		0.02		0.02	
AFO B								
Test	**PL [Nm/°]**	**PL [%]**	**PU [Nm/°]**	**PU [%]**	**DL [Nm/°]**	**DL [%]**	**DU [Nm/°]**	**DU[%]**
1st	3.41	0.27	3.08	0.25	2.87	0.16	2.74	0.40
2nd	3.43	0.16	3.07	0.03	2.84	0.74	2.74	0.71
3rd	3.43	0.11	3.06	0.29	2.88	0.58	2.69	1.11
Mean	3.42		3.07		2.86		2.72	
SD	0.01		0.01		0.02		0.03	
AFO C								
Test	**PL [Nm/°]**	**PL [%]**	**PU [Nm/°]**	**PU [%]**	**DL [Nm/°]**	**DL [%]**	**DU [Nm/°]**	**DU[%]**
1st	3.57	0.96	3.50	1.26	2.93	1.33	2.82	1.58
2nd	3.54	0.26	3.48	0.74	2.88	0.21	2.77	0.17
3rd	3.49	1.22	3.38	2	2.86	1.12	2.73	1.41
Mean	3.53		3.45		2.89		2.77	
SD	0.04		0.06		0.04		0.04	
AFO D								
Test	**PL [Nm/°]**	**PL [%]**	**PU [Nm/°]**	**PU [%]**	**DL [Nm/°]**	**DL [%]**	**DU [Nm/°]**	**DU[%]**
1st	6.16	0.13	5.58	0.60	3.97	0.02	3.56	0.87
2nd	6.17	0.02	5.53	0.25	3.97	0.05	3.52	0.30
3rd	6.17	0.10	5.52	0.35	3.97	0.07	3.51	0.57
Mean	6.17		5.54		3.97		3.53	
SD	0.01		0.03		0.01		0.03	

Table 3.4: Intra-tester variability, with measures expressed as absolute values and percentage difference from the mean.

AFO A

Test	PL [Nm/°]	PL [%]	PU [Nm/°]	PU [%]	DL [Nm/°]	DL [%]	DU [Nm/°]	DU[%]
1st	2.96	0.61	3.17	4.20	2.66	1.81	2.63	3.96
2nd	2.92	0.61	3.45	4.20	2.56	1.81	2.43	3.96
Mean	2.94		3.31		2.61		2.53	
SD	0.03		0.20		0.07		0.14	

AFO B

Test	PL [Nm/°]	PL [%]	PU [Nm/°]	PU [%]	DL [Nm/°]	DL [%]	DU [Nm/°]	DU[%]
1st	3.41	1.30	3.08	2.83	2.87	1.16	2.74	0.51
2nd	3.33	1.30	2.91	2.83	2.93	1.16	2.76	0.51
Mean	3.37		2.99		2.90		2.75	
SD	0.06		0.12		0.05		0.02	

AFO C

Test	PL [Nm/°]	PL [%]	PU [Nm/°]	PU [%]	DL [Nm/°]	DL [%]	DU [Nm/°]	DU[%]
1st	3.57	5.26	3.50	3.42	2.93	3.87	2.82	0.21
2nd	3.96	5.26	3.74	3.42	2.71	3.87	2.80	0.21
Mean	3.76		3.62		2.82		2.81	
SD	0.28		0.18		0.15		0.01	

AFO D

Test	PL [Nm/°]	PL [%]	PU [Nm/°]	PU [%]	DL [Nm/°]	DL [%]	DU [Nm/°]	DU[%]
1st	6.16	0.43	5.58	3.33	3.97	1.59	3.56	3.98
2nd	6.21	0.43	5.96	3.33	3.84	1.59	3.85	3.98
Mean	6.19		5.77		3.91		3.71	
SD	0.04		0.27		0.09		0.21	

Table 3.5: Inter-tester variability, with measures expressed as absolute values and percentage difference from the mean.

AFO A

Test	PL [Nm/°]	PL [%]	PU [Nm/°]	PU [%]	DL [Nm/°]	DL [%]	DU [Nm/°]	DU[%]
1st	2.96	1.07	3.17	2.74	2.66	5.65	2.63	0.97
2nd	3.02	1.07	3.35	2.74	2.98	5.65	2.58	0.97
Mean	2.99		3.26		2.82		2.61	
SD	0.05		0.13		0.23		0.04	

AFO B

Test	PL [Nm/°]	PL [%]	PU [Nm/°]	PU [%]	DL [Nm/°]	DL [%]	DU [Nm/°]	DU[%]
1st	3.41	2.28	3.08	1.92	2.87	1.97	2.74	1.91
2nd	3.57	2.28	3.20	1.92	2.98	1.97	2.84	1.91
Mean	3.49		3.14		2.92		2.79	
SD	0.11		0.09		0.08		0.08	

AFO C

Test	PL [Nm/°]	PL [%]	PU [Nm/°]	PU [%]	DL [Nm/°]	DL [%]	DU [Nm/°]	DU[%]
1st	3.57	1.04	3.50	3.70	2.93	1.50	2.82	0.97
2nd	3.64	1.04	3.25	3.70	2.84	1.50	2.76	0.97
Mean	3.60		3.37		2.88		2.79	
SD	0.05		0.18		0.06		0.04	

AFO D

Test	PL [Nm/°]	PL [%]	PU [Nm/°]	PU [%]	DL [Nm/°]	DL [%]	DU [Nm/°]	DU[%]
1st	6.16	1.63	5.58	2.14	3.97	0.91	3.56	1.37
2nd	5.96	1.63	5.34	2.14	3.90	0.91	3.66	1.37
Mean	6.06		5.46		3.93		3.61	
SD	0.14		0.16		0.05		0.07	

After all the experiments were performed , in order to assess the reliability of the stiffness measures during the test-retest, intra-tester and inter-tester analyses, the Intraclass Correlation Coefficient (ICC) was calculated [123]. This represents a widely used index, especially in the clinical assessment, for evaluating the reliability of the analyses, which defines the extent to which measurements can be replicated. There are different forms of the ICC, depending on the distinct assumptions and situations, which can lead to different results with the same set of data.

In general, reliability represents the ratio between the true score variance and the total score variance, which is composed by the true score variance and the error variance. Sources of error can be systematic, due to constant errors and/or bias, or random, due to chance factors such as luck, alertness, biological variability etc. In our case, the calculation is done with the program called SPSS 24.0 by using a two-way mixed-effects model for all the three cases: this model considers the selected raters as the only raters of interest, since they are not randomly selected from a large population, and every single measurement is associated to every rater (no averaged values). In addition, the absolute agreement definition between raters provides a more stringent ICC, which is used when the systematic variability is relevant, thus to be inserted at the denominator of the ICC formula.

When using the absolute agreement definition, as in our case, the outcomes from a 2-way mixed-effects or 2-way random-effects models will result in the same ICC values, since they use the same formula [123]. This is important because considering a two-way random-effects model allows to generalize the reliability results to any tester who has the same characteristics as the selected testers for the study. Therefore, the difference between the two models is not based on the calculation itself but on the experimental design of the reliability study and the interpretation of the results.All these considerations are especially important when selecting the ICC for the quantification of the inter-tester variability; concerning the test-retest and intra-tester variability, an approach with a 2-way mixed model with absolute agreement is usually suggested, since it would not be correct to consider the measurements as randomized samples and with no agreement between repeated measurements [101].

In light of this information, the decision of using a two-way mixed-effects model for the calculation of the variability in the three cases was made. The outcomes of the ICC are expressed as follows: values lower than 0.5 are indicative of poor reliability, values between 0.5 and 0.75 indicate moderate reliability, values between 0.75 and 0.9 a good reliability, while values higher than 0.90 express a high reliability of the measures. Besides the ICC, two other indices were calculated: the Standard Error of Measurement (SEM) and the Smallest Detectable Difference (SDD). The SEM, which is expressed in absolute measures, gives an indication of the expected measurement error in a single individual score and is calculated by multiplying the standard deviation (SD) of the measures with the square root of (1-ICC). The SDD, instead, which is calculated as the SEM multiplied for 1.96 and the square root of 2, defines a threshold value of change in scores for the tester to be 95% confident that a true change, in terms of AFO stiffness in our case, beyond that of the measurement error had occurred [75].

The results of the ICC, SEM and SDD for the evaluation of the test-retest repeatability and intra-tester and inter-tester variability are reported in table 3.6. In particular the calculation of the ICC shows a high reliability of the setup with values always higher than 0.94. These values are confirmed with the calculation of the SEM which expresses relatively low values of measurement error. At last, the SDD was quantified, in order to provide the system discrimination.

Table 3.6: Calculation of ICC, SEM and SDD.

	PL			PU			DL			DU		
	ICC[%]	SEM [Nm/°]	SDD [Nm/°]	ICC[%]	SEM [Nm/°]	SDD [Nm/°]	ICC[%]	SEM [Nm/°]	SDD [Nm/°]	ICC[%]	SEM [Nm/°]	SDD [Nm/°]
Test-retest	1	0	0	1	0.25	0.69	1	0.06	0.16	0.99	0.09	0.24
Intra-tester	0.99	0.29	0.81	0.97	0.40	1.10	0.97	0.19	0.53	0.94	0.25	0.70
Inter-tester	0.99	0.19	0.54	0.98	0.29	0.80	0.94	0.25	0.69	0.98	0.12	0.32

These outcomes indicate that the experimental setup can be successfully applied for the quantification of the AFO stiffness around an axis aligned to the anatomical ankle joint during the second rocker of the gait in a reliable and non-destructive manner.

3.7 INVESTIGATION OF OTHER PARAMETERS

After the investigation on the experimental setup in providing reliable stiffness measures, the influence of other parameters is evaluated, such as the accuracy between different cycles during a single AFO experiment and the recovery time between two subsequent experiments.

3.7.1 Investigation of other parameters

As indicated in Section 3.6, the depicted values of ankle stiffness are averaged over the cycles performed during a single measurement. Therefore, an important factor to be investigated is the accuracy between the different cycles of the same measurement. As anticipated, due to the Mullins effect, the first cycle is rejected; the averaging calculation is applied from the 2nd till the last cycle. An example, obtained from the AFO D, is shown in figure 3.24.

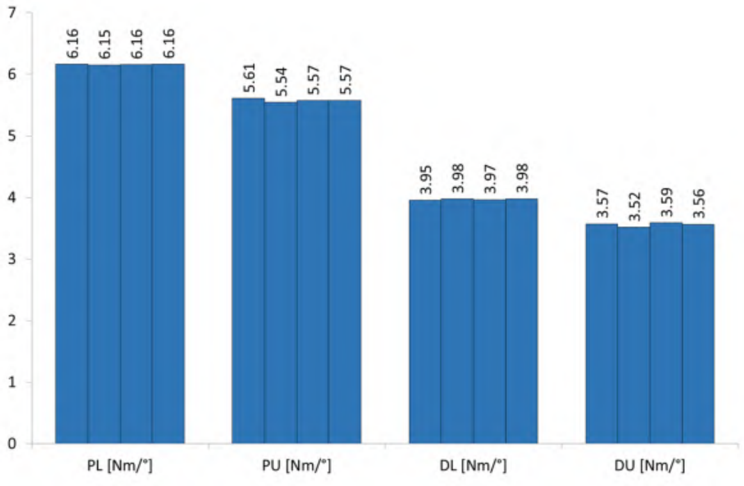

Figure 3.24: Accuracy between cycles: results in terms of stiffness on the AFO D.

In this case, if we calculate the error between the cycles for the AFO D, we obtain the following error percentages: 0.18 % in the PL, 1.2 % in the PU, 0.63 % in the DL and 1.97 % in the DU quadrants. In general, the error percentage never exceeds 3 % in the worst cases, which are typically found during the unloading phases, where the material's behavior is mostly nonlinear. However, since the error is rather small and negligible, one averaged value for each quadrant of the stiffness graph is calculated and considered.

3.7.2 Recovery time

The recovery time is the time needed for the AFO to recover its mechanical properties after an initial test; for example, if an AFO would be tested multiple times, the recovery time represents the amount of time that would be advisable to wait before retesting the device. This quantification was performed for the AFO E, fully 3D printed, which was tested four times: after an initial test, three other trials followed, with a variable waiting time between the different trials of respectively 1, 5 and 10 minutes (table 3.7).

Table 3.7: Stiffness values for the study of the recovery time, expressed as absolute values and percentage difference from the initial value.

AFO E								
Recovery time	**PL [Nm/°]**	**PL [%]**	**PU [Nm/°]**	**PU [%]**	**DL [Nm/°]**	**DL [%]**	**DU [Nm/°]**	**DU[%]**
initial	1.78		1.92		1.32		1.10	
1 min	1.78	0.62	1.97	2.82	1.31	0.75	1.15	4.81
5 min	1.75	0.90	1.87	2.61	1.38	4.23	1.14	3.27
10 min	1.74	1.86	1.91	0.57	1.35	2.04	1.16	5.63
Mean	1.76		1.91		1.34		1.14	
SD	0.02		0.04		0.03		0.03	

The results already show good percentages after 1 minute of recovery time, where the maximum error is 4.81 % in correspondence of the DU quadrant. After ten minutes, an error of 5.63 % is obtained in the same quadrant. These values are a little high compared to those obtained for the other AFOs in table 3.3 (test-retest results) and are probably caused by the greater non-linear behavior of the AFO E, which affected the measurement results in that region of the graph.

3.8 DISCUSSION AND CONCLUSIONS

This chapter presented the design of a new semi-automated experimental setup, created for the non-destructive evaluation of the stiffness of AFOs around an anatomically aligned ankle axis over a maximum range of motion of +/- 25 degrees (dorsiflexion/plantarflexion), during the second rocker of the stance phase of the gait. This setup will be further expanded in order to allow the full characterization of the 3D printed AFOs around three other axes of motion in the frontal and transverse planes and around the MTP joint (more details reported in Chapter 5).

This study focused on 3D printed orthoses, but potentially the test rig could be applied to any topology of AFO, since the experimental setup gives the possibility to accommodate a wide range of AFOs, which are secured in the test rig using a patient-specific leg model, made in MDF. The MDF leg model contains the location of the anatomical points defining the ankle flexion/extension axis used in the gait analysis (see Paragraph 3.2) and the rig applies moments around it to derive the AFO stiffness. The definition of the ankle flexion/extension axis and the relative anatomical points are derived from the kinematic model of the lower limb initially developed by Davis et al. [120], which is widely used for the gait analysis of cerebral palsy patients who represent a large group of AFO users. This model takes a macroscopic approach to modelling the lower limb which has limitations anatomically but remains valuable from a clinical perspective of measuring gait abnormalities and treatment planning/monitoring. The approach taken here is to adopt the axes of this 3D model in AFO definition, design and mechanical testing so to enable the clinicians, orthotists and design engineers to be able to discuss and understand the same expression/description of 3D movement.

During the positioning of the AFO in the test rig, the neutral angle (shown to be an important factor that influences patients' gait [75]) is also measured by using a digital goniometer. The five AFOs used previously were tested over their specific range of motion according to the data coming from the gait analysis to ensure the best approximation of the AFO stiffness felt by the considered subject during the second rocker of the gait, when the foot is completely in contact with the ground and the forward progression of the body is observed. The magnitude of these stiffness values is in line with the results obtained by other research groups ([113], [58]), which have also examined 3D printed AFOs. The highest stiffness values were found for the AFO D, which was worn by the patient with the highest mass compared to the other subjects analyzed; conversely, the smallest contributions were measured for the AFO E, which was the AFO worn by an unimpaired subject, who had no clinical need of using an AFO (figure 3.23).

In this dissertation, since the setup will be used by the other partners of the project (see paragraph 1.7.1), different factors were studied: the pure system test-retest repeatability and the intra-tester and inter-tester variability. For the system test-retest repeatability, the maximal percentage difference is never higher than 2%. Schrank et al. [113], evaluated the test-retest variability for 3D printed AFOs obtaining a maximal difference of 4.7%, but only considering two repetitions. Other studies ([75], [82]) assessed the test-retest variability by calculating the ICC on thermoplastic and/or carbon fiber AFOs, obtaining high results as in our study (table 3.6). Bregman et al. [75], which also examined four AFOs as in our study, reported high reliability in terms of the intra-tester and inter-tester variability, similar to the values we obtained. In addition, the calculation of the SEM revealed low values of measurement error associated to each variability index (table 3.6). Two operators were considered during the analysis of the inter-tester variability as done in another study [124]; this could be considered a limitation, therefore, a bigger number of operators will be included in the future for analyzing this parameter, i.e. when the new version of the experimental setup with four axes of motion will be completed.

Other parameters were also investigated: the accuracy between cycles showed a rather small error, which reached a maximal value of 3% in the worst cases, due to the nonlinear behavior of the AFOs in the unloading phases.

Concerning the study of the material recovery time, it was performed on the AFO E, owned by an unimpaired subject, which was included in the study because it was entirely 3D printed, allowing to exclusively examine the behavior of the 3D printable material used (PA 12). The test showed that after one minute was already possible to obtain good error percentages between two subsequent stiffness tests on the same AFO. Whilst the error in the DU quadrant is a little high compared to those obtained for the other AFOs in table 3.3 for the same quadrant, the presence of greater non-linear behavior for the AFO E was noted in this quadrant. Since different AFO designs can have an impact on the linearity, more tests on other AFOs are desirable.

As anticipated, the used ranges of motion were previously derived from the gait assessment on the patients performed in the clinical environment; in the future patients with higher ranges of motion might also be included in the process. All the stiffness plots showed the presence of hysteresis, due to the non-linear viscoelastic behavior of the material and to the friction present within the experimental setup. In contrast with other authors ([75], [76], [78], [79], [80], [81], [85], [94], [96], [93], [97], [113]) four different ankle stiffness values are considered for each zone of the angle vs. torque curve, as it can be observed that most patient-specific AFOs have a different behavior in plantarflexion compared to dorsiflexion due to their shape. The impact of the hysteresis could present a limitation. E.g. Hysteresis due to friction may lead to an overestimation of the measured AFO stiffness in the unloading phases, especially if high ranges of motion are used. Therefore modifications will be implemented in the new version of the experimental setup to lower this contribution, for example by modifying the actual clamping system and/or by improving the lubrication of the different components within the setup for allowing a smoother movement.

In this study, the effect of speed on the derived stiffness was not investigated as we used a constant speed of 1 °/s, in accordance with the values seen during gait; this was not permitted by the current instrumentation but modifications will be applied in order to better mimic the real life conditions in the future studies.

As anticipated, for the optimal fixation of the AFOs in the setup, MDF blocks containing the anatomical landmarks of the patients were used: they have rigid material properties, which are very different from the human tissue of the patients. They were chosen since the main goal of the current study was to find a methodology that allows to align the AFOs to the anatomical ankle joint of the patients and evaluate their mechanical behavior, that will be used for the validation of the finite element models of the devices, further described in Chapter 4. In addition, these stiffness values could also be directly used in rigid body kinematic models of the lower limb to predict the impact on the gait pattern of the patients and improve their prescription process. However, further studies, using cadaveric limbs, will be performed in the future to assess how the contact of the AFO with the human tissue influences the stiffness measures.

In conclusion, the outcomes obtained from the experimental tests, illustrated in this chapter, indicate that the experimental setup is able to quantify the ankle stiffness of AFOs over their specific ranges of motion and that can be used to gain better insight in the prescription process. Currently, the quantification of the stiffness required by each patient is not done in the clinical practice and the AFOs are only classified as flexible, rigid, semi-flexible/rigid based on the experience of the involved orthotists and doctors; therefore, we believe that, by including the quantification of the ankle stiffness in the clinical practice, a better prescription of the AFOs will be reached, minimizing the trial-error process used till now to obtain the final configuration of the AFOs used by the patients.

III

Finite element analysis of AFOs

Chapters

Chapter 4

Realization of the computational models

This chapter provides the description of the modelling strategy used for the creation of a standardized framework for the evaluation of the ankle stiffness and stress distribution of 3D printed AFOs. Four FE models allowed the quantification of the patient-specific devices over their specific range of motion during the second rocker of the gait. The validation of the FE models was performed by comparing the model outputs with the results obtained from the dedicated experimental test rig, described in Chapter 3. In particular, a detailed overview on the mesh creation, material model, boundary and loading conditions, is provided.

4.1 Introduction

As previously discussed in Chapter 1, the commonly used manufacturing process of AFOs is time consuming and requires the ability of skilled orthotists, in order to minimize the possible variations in terms of thickness and/or stiffness; these properties, which are highly important for the successful application of the devices, are challenging to control during the thermoforming production process. In addition, this way of manufacturing does not allow modifications of the design parameters before the realization of the devices, while it would be beneficial to quantify their impact in advance. In this scenario, different research groups have investigated the use of additive manufacturing technologies on healthy subjects and/or patients to study the

AFOs biomechanical contribution, driven by the idea that a higher control of the design characteristics would be possible ([57], [60], [61], [62],[63], [64]). 3D printing technologies can be complemented with the construction of computational models for the patient-specific AFOs, which require validation through dedicated experimental tests before being used: this would allow the prediction of the mechanical properties and potential stress concentrations before manufacturing the devices and thus prevent wasted production time and errors ([101], [106], [109], [110]). As illustrated in Chapter 2, this approach was used by different research groups for the evaluation of different types of 3D printed AFOs ([44], [112], [113], [115], [117]). However, none of the previous studies were simulating the devices during a continuous cycle of plantarflexion and dorsiflexion. Therefore, the possibility of virtually predicting the mechanical behavior of the AFOs for a complete range of motion, derived from the patients' gait assessment, could provide further information for the optimal realization of the devices.

In this context, the current chapter describes a new standardized framework for the creation of FE models of 3D printed patient-specific AFOs, in order to quantify the ankle stiffness and the stress distribution during the second rocker of the gait. More specifically, the aim was the validation of these models through the utilization of the dedicated in-house developed mechanical test rig, described in Chapter 3, that establishes the clinical AFO conditions replicated in the FE simulations. This represents an important step for the future application of the FE models in the prediction of the behavior of the AFOs in case of pathological conditions and in combination with optimization algorithm to speed up the design and realization of more effective 3D printed AFOs.

4.2 METHODS

This section describes the generation of the 3D shell (quadrilateral) mesh for the finite element models of two different AFO designs (realized by V!GO NV and 3D printed by Materialise NV), chosen in order to obtain reliable results in a reasonable amount of time compared to the other available element types, and the implementation of a parallel rheological framework for the definition of the material model for the PA 12; the material model is then combined with specific boundary and loading conditions, which replicate the conditions applied to the AFOs during the tests performed inside the experimental setup, described in Chapter 3.

4.2.1 Construction of the quadrilateral mesh

In this study, the mechanical properties of two different AFO designs were investigated: a full shell and a modular design (figure 4.1 A-B). The full shell

AFO consists of one part while the modular AFO is made of three parts: a foot and a calf part connected by two rods.

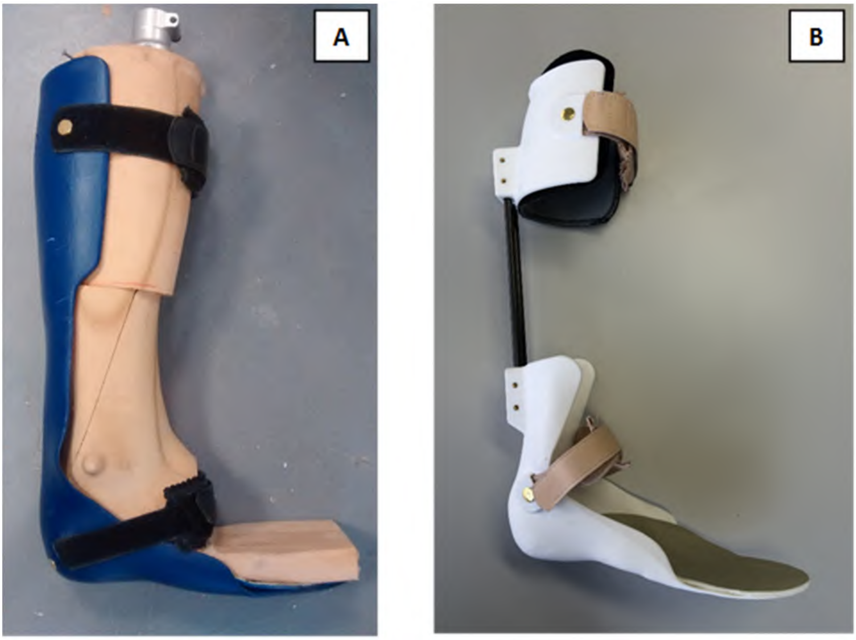

Figure 4.1: Examples of the used full shell (A) and modular (B) AFO designs. The full shell AFO is composed of one part while the modular design contains a foot and a calf part connected by two rods.

The virtual representation of the two AFO designs required different steps: the starting point was the creation of an algorithm for the conversion of the initial STL file format in a new regular mesh, made of 3D shell quadrilateral elements, in order to obtain reliable AFO results in a short amount of time (comparison between different analysis times based on the used element types and grids is shown in Section 4.3).
STL files, widely used for 3D printing, only provide a description of the surface geometry of a three-dimensional object, represented by an union of raw unstructured triangles (figure 4.2). If directly used for finite element simulations, they might lead to inaccurate and unstable results because of the irregular shape of the triangular mesh. In addition, no information about the thickness of the device would be taken into account. After improving the quality of the unstructured triangles contained in the mesh, STL files could also be used to create structured meshes (i.e. with solid elements); however it would not be possible to have the same flexibility and easiness as with the algorithm created in this project, for the realization of quadrilateral shell meshes.

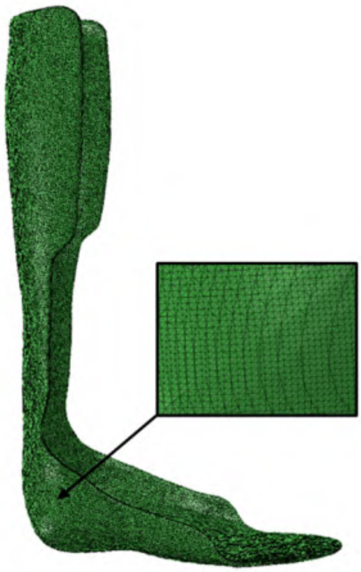

Figure 4.2: Example of an AFO in the STL file format.

The algorithm for the STL files conversion was written in the open-source software pyFormex: it enables separate consideration of the internal and the external surfaces of the selected AFO (figure 4.3 A). Before slicing to obtain different polylines (figure 4.3 B), the AFO is divided in three parts (calf, ankle, forefoot) as this subdivision permits to choose a different density of the polylines for each part; i.e. around the ankle zone a high number of polylines is used, which means that a high number of elements can be created in this area. This is done for enhancing the detection of the stress variations in the critical bending zone. The subdivision zones are selected by the user depending on the geometry of the considered AFO, while the rest of the algorithm is completely automated. Subsequently all the polylines are reconnected and a regular representation is obtained (figure 4.3 C). The final mesh of the device is obtained by averaging the internal and external meshes, in order to erase all the possible artifacts (figure 4.3 D). At this level, smoothing operations are applied for eliminating eventual sharp edges that might provoke unrealistic stress concentrations.
3D shell quadrilateral elements were used for the construction of the modular design AFO mesh which has a uniform thickness. For the full shell mesh, which has a non uniform thickness, an additional step was required: the thickness was calculated by considering the distance between the final quadrilateral mesh and the initial STL file, and subsequently provided for the numerical calculation. The final meshes for the two AFO designs ranged between 43000 and 65000 linear shell elements with reduced integration (S4R, as defined in the software Abaqus 2017) and are indicated in table 4.14.

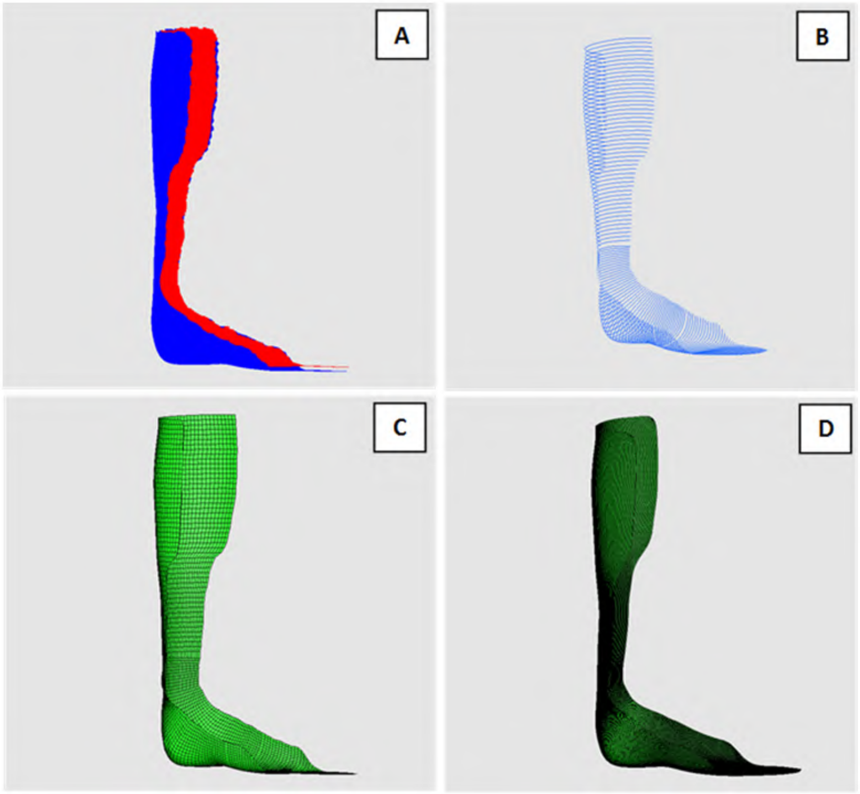

Figure 4.3: Example of the algorithm application on the full shell mesh: (A) separate consideration of internal and external mesh, (B) different slices of the geometry, (C) reconnection of the slices to obtain a quadrilateral mesh and (D) the final AFO mesh.

Shell elements are typically used for modelling structures where one dimension, the thickness, is notably smaller than the others [125]. This type of elements discretize the specific object by defining the geometry at a reference surface, while the thickness is provided through the definition of the section property. S4R are linear shell elements which account for finite membrane strains and arbitrarily large rotations, which make them useful for large-strain problems. These elements use a reduced integration, which means that they contain one integration point, in comparison to the full integration elements (S4), that use four integration points. In bending problems, fully integrated first order elements might suffer from a numerical issue called shear locking, which makes them excessively stiff, resulting in wrong results, due to the introduced artificial shear stresses. Using a reduced integration, instead, would be possible to deliver more accurate results and a significant reduction of the computational time of the analysis, especially for three dimensional problems [125]. S4 elements have another limitation: because of their mathematical formulation, they cannot be used for describing the behavior of hyperelastic materials; therefore they cannot be implemented for the prediction of the AFOs used in this study [125].

On the other side, when reduced integration first-order elements are employed, the hourglass control in the mesh setting is required. Hourglass is a mechanism that provokes an uncontrolled distortion of the elements when the stress at the integration point is equal to zero. To overcome this problem, a finer mesh may be required, in case of shell elements, or more elements through the thickness, if solid elements are used.

In this study, a mesh sensitivity analysis was performed over a range of 10 degrees in both dorsiflexion and plantarflexion (total range of 20 degrees), which revealed that with the used mesh numbers a converged solution was obtained. More details about using different mesh grids (20500 S4R elements till 102500 S4R elements), or different element types (S4R versus C3D8R) will be provided in Section 4.3.1.

4.2.2 Creation of the AFO computational models

For this study, four patients (both children and adults) were selected, which were affected by the following pathologies: trauma, neuro-muscular disorder and/or cerebral palsy. Consequently, four patient-specific finite element AFO models were created: one model with a full shell design and three models with the modular design. Each AFO has a different EU foot size, as specified in table 4.1 and they are all made for a right foot; their choice is based on whether they were (or not) subjected to modifications of the trimlines by the CPOs after their realization. Sometimes it can happen that the AFOs are further trimmed in order to provide a more comfortable fit to the patients; therefore, choosing AFOs with none or minimal changes ensures that the STL files used for the creation of the meshes are fully representative of the geometry of the 3D printed devices.

Table 4.1: Different AFOs EU foot size.

AFO	Foot size
A	40
B	35
C	37
D	38

For every modular AFO, the rods were made of carbon fiber reinforced polymer (CFRP) and their thickness was 6 mm. The foot and the calf parts of the AFOs were realized in PA 12. The full shell AFO, instead, was completely realized in PA 12. Since this polymer owns complex visco-elasto-plastic properties [67], the virtual implementation needed the utilization of a complex material model, called Parallel Rheological Framework (PRF) model: this model is based on the superposition of finite-strain viscoelastic and elastoplastic networks in parallel, thus to have an additive total stress response. More details will be provided in section 4.2.3.

The simulated movement of the AFOs can be considered as a static problem: the rotation of the AFO calf around the ankle joint is effected at a low velocity (1 °/s), as in the experimental tests described in Chapter 3, which implies that dynamic inertia effects can be neglected, since they don't play an important role. As a consequence, an implicit finite element solution technique was implemented in Abaqus/Standard 2017, in order to predict the behavior of the devices. All the related boundary and loading conditions will be further described in section 4.2.4.

4.2.3 Material model: the Parallel Rheological Framework

The AFOs, or parts of them, used in this PhD project, were 3D printed using PA 12, a polymer which exhibits a nonlinear response, that cannot be described by the traditional viscoelastic models (see Paragraph 1.6.1). Several tensile, compressive, shear and relaxation tests, carried out on samples of the material, were conducted for obtaining the material parameters used for the virtual implementation of the AFOs by Dr. N. Lammens (Department of Materials Science & Engineering – Ghent University) [67].

Since the material showed a combination of visco-elasto-plastic properties, it was necessary to implement a new constitutive model, called Parallel Rheological Framework (PRF) model, developed in the commercial finite element software Abaqus 2017 ([125],[126],[127]). The PRF model is intended for modeling polymers and elastomeric materials that show permanent set and a nonlinear viscous behavior, which makes it suitable for the PA 12. In particular, the framework is composed by multiple networks connected in parallel, as visible in figure 4.4.

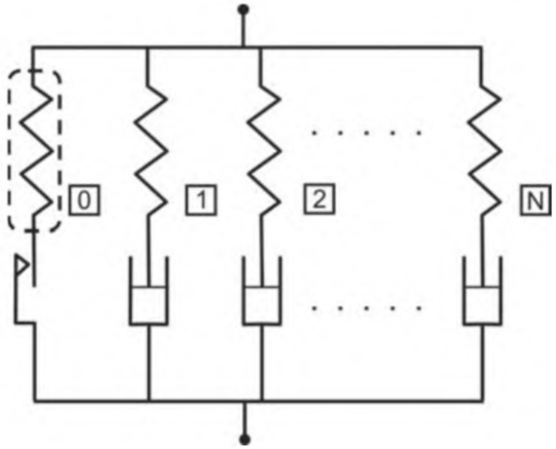

Figure 4.4: Schematic representation of the Parallel Rheological Framework (PRF).

The number of the viscoelastic networks, N, can be arbitrary, while only one equilibrium network can be considered, which can be purely elastic or elastoplastic (network 0). If the equilibrium network is not defined, the material will relax completely over time till reaching a stress value equal to zero; otherwise a residual value of stress will be reached. Including the plasticity within the equilibrium network allows for modeling the permanent set when the load is removed. It can also include Mullins parameters, which, as previously said, are used to describe a possible softening effect of the material; however, they were not included in our formulation. A brief description of the Mullins effect was introduced in Section 3.3.

Concerning the elastic part, it is described by an hyperelastic material model, which is valid for all the networks and scaled to each network by a specific stiffness ratio. The viscous part, instead, needs to be defined for each viscoelastic network.

The nonlinear viscous effects were modeled using the power law model formulation, while the plasticity was expressed with the stress values at the corresponding plastic strain (table 4.2, table 4.3 A). The elastic response was specified using hyperelastic neo-hookean material coefficients (table 4.3 B). All the used parameters are suitable for describing the behavior of the PA 12 during a static analysis and were extracted by the experiments performed by Lammens et al. [67]: in particular, the tensile tests on samples of the PA 12 showed how the material has an isotropic behavior in the elastic region, which means that the printing direction has no effect on the elastic material properties; however, while increasing the test speed an increase in the Young's modulus is also noticeable. The tensile tests curves obtained at the three different speeds (5, 50 and 500 mm/min), together with the relaxation data obtained at an initial stress of 10 MPa, were then used to obtain the parameters of the PRF model [67]. There is no speed associated with the relaxation data, which means that the viscous parameters are independent of speed. The software (Abaqus) will then use the viscous constants and the tensile curves at different strain rates to obtain the parameters for the strain rate indicated in the simulation. In our case we used a speed of 1 °/s in order to allow the validation of the finite element models of the patient-specific 3D printed AFOs with the results coming from the experimental setup, described in Chapter 3.

Therefore, the PRF model is suitable for representing the mechanical behavior of a 3D printed AFO during an entire loading-unloading cycle under static conditions; however, the used parameters are not able to predict the stiffness degradation over time due to fatigue, and they eventually need to be integrated with other parameters to predict this behavior.

The material properties of the CFRP rods, present in the modular AFOs design, were also obtained experimentally by Dr. N. Lammens (table 4.4).

Table 4.2: Nonlinear viscoelastic parameters for PA 12 [67].

Network	Stiffness ratio	q_0 [N/m2]	n	m	a	ε_0' [1/s]
1	0.162	2.52e+09	1.081	-0.026	0	1
2	0.184	29.236	3	-0.012	0	1

Table 4.3: A. Plastic parameters for PA 12. B. Hyperelastic parameters for PA 12 [67].

Plastic stress [MPa]	Plastic strain
17.644	0.0
34.096	0.005
1.0	0.150

C_{10} [MPa]	D_1 [1/MPa]
395.986	6.335 e-4

Table 4.4: Parameter for the carbon fiber reinforced polymer (CFRP) rods.

E_1 [GPa]	E_2 [GPa]	E_3 [GPa]	ν_{12}	ν_{13}	ν_{23}	G_{12} [GPa]	G_{13} [GPa]	G_{23} [GPa]
95	8	8	0.35	0.35	0.35	2	2	3

4.2.4 Boundary and loading conditions

The boundary and loading conditions used in the FE models were implemented for replicating the movements and constraints imposed by the experimental setup (figure 4.5), described in Chapter 3, specifically designed for the evaluation of the ankle stiffness of the AFOs during the second rocker of the stance phase of the gait.

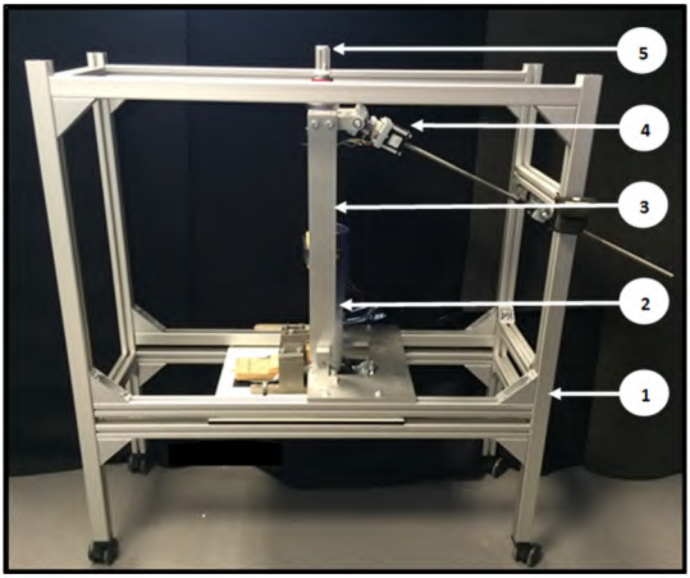

Figure 4.5: Overview of the experimental setup for testing the modular 3D printed AFOs: 1. External frame; 2. AFO; 3. U-shaped frame; 4.Linear motor; 5. Shank axis.

As previously explained, the fixation of the AFOs in the test rig is via a custom made clamping system which makes use of MDF blocks representing the patients' leg, which contain anatomical landmarks for allowing the alignment of the test rig axis to the anatomical ankle axis. These details are extremely important when defining the deflection axis in the computational environment, which has to correspond to the experimental one (figure 4.6 A-B). In fact, the STL files of the patients' leg, used for the experimental setup (see Paragraph 3.2), are imported in Abaqus and fitted to the specific AFO. In figure 4.6 A-B, the anatomical markers on a generic patient's leg are shown, which are used for identifying the location of the ankle and shank axes for the experimental and computational tests (see Paragraph 3.2). The ankle axis is indicated by the two small hemispheres at both ends of the axis (medial and lateral malleoli) on the MDF block (figure 4.6 B; item 3). The shank axis, instead, by the midpoint of the ankle axis and the intersection of the two lines from medial to lateral and posterior to anterior markers on the patient leg mould, just below the knee joint centre (these points being established by projections from the shank axis of the 3D scan of the leg in the AFO design software, used by V!GO NV) (figure 4.6 B; item 4). As previously explained in Chapter 3, these anatomical definitions are derived from the Plug-in-Gait kinematic model (VICON Motion Systems), which is a variant of the original model of the lower limb developed by Davis et al. [120] and has been widely used in clinical gait analysis for many years and continues to be seen as a reference standard. The goal of using these terms is to make a direct connection between the kinematics as defined and measured in the gait laboratory when walking both barefoot and with AFO, in mechanical testing of the AFO and in the computer simulations.

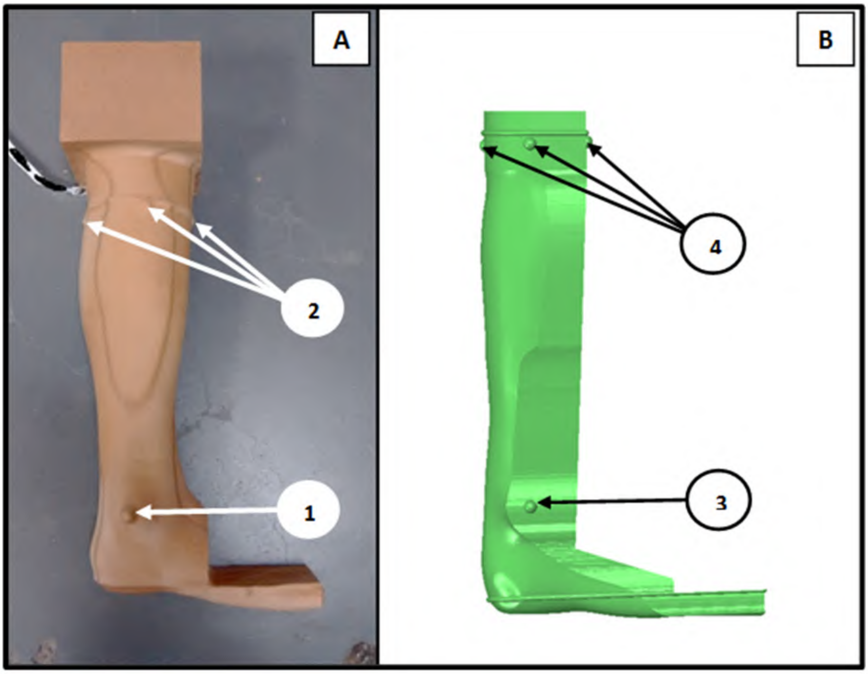

Figure 4.6: Patient leg intended for the experimental tests (A) and its virtual representation (B): the arrows indicate the anatomical landmarks for the identification of the ankle (1;3) and shank (2;4) axes, respectively in the experimental setup and in the finite element environment.

In the finite element environment, the coordinates of all the anatomical markers are included, in order to define the location and the orientation of the ankle and the shank axes, as used in the experimental setup. By using the coordinates of the lateral and medial malleoli, it is possible to calculate the location of their midpoint, which is called ankle reference point and represents the virtual ankle joint; while, by the intersection of the four landmarks at the calf section, the calf reference point is defined (figure 4.7). The location of the lateral and medial malleoli is also used for providing the orientation of the deflection during the plantarflexion/dorsiflexion movements around the virtual ankle joint, as in the experimental setting. The loads are applied as deflections in proximity of the virtual ankle joint and, for each AFO, are based on the previous patients' assessment in the gait lab, which enables to derive their specific range of motion (table 4.5).

Table 4.5: AFOs ranges of motion. Plantarflexion is indicated with negative angles and dorsiflexion with positive angles.

AFO	Plantarflexion [°]	Dorsiflexion [°]
A	-2	3
B	-6	3
C	-5	5
D	-8	8

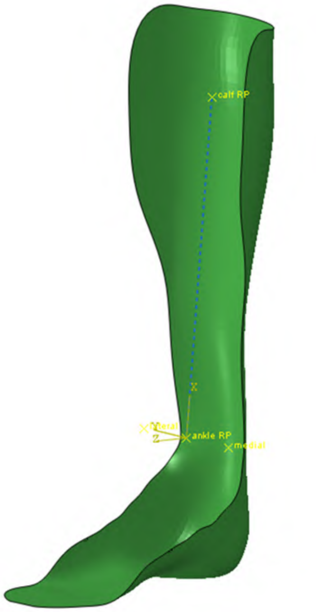

Figure 4.7: Virtual representation of an AFO, where the ankle and calf reference points are highlighted.

As visible from figure 4.7, the virtual ankle joint is connected to the calf reference point: this is effected by a "Slot + Revolute" connector, which allows the calf point to slide up and down along and to rotate around the shank axis with respect to the virtual ankle joint. The deflection is applied in proximity of the virtual ankle joint, which guides the movement of the calf reference point in the sagittal plane, mimicking the AFO behavior in the test rig, where the motor induces the movement of the U-shaped frame around the rotational axis of the setup. The calf reference point is then connected to the internal surface of the modular calf part or to the upper part of the shell design (figure 4.8B) in proximity of the calf straps; they are constrained to follow the movements of the reference point by a kinematic coupling, which induces the deformation on the device and represents the connection of the AFO to the leg of the patient. In case of the modular design, the kinematic coupling is also used to connect the rods to the solid blocks contained on the foot and calf parts: the goal is to mimic the connection used in the reality, where the rods are glued inside the blocks allowing no relative movement between them.

Knowing the location of the virtual ankle joint, allows the calculation of the moments acting on the device during the rotation. In this way it is possible to define the AFO stiffness, which is the moment around the ankle joint exerted by the AFO per degree of ankle joint rotation [75]. As explained in the previous chapters, the evaluation of the AFO ankle stiffness is performed using four values, corresponding to the four zones of the angle vs. torque graph: Plantarflexion Loading (PL), Plantarflexion Unloading (PU), Dorsiflexion Loading (DL) and Dorsiflexion Unloading (DU). For each of these zones, the stiffness value is quantified as the slope of the angle vs. torque curve in the specific quadrant.

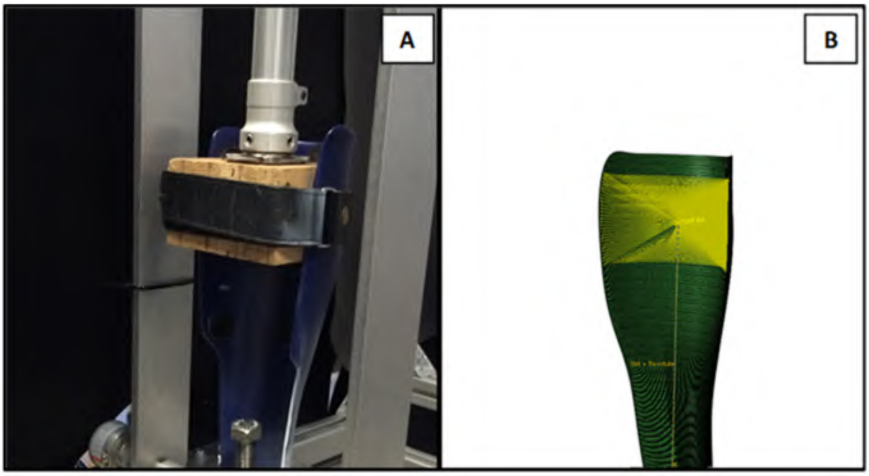

Figure 4.8: Full shell AFO constrained at the calf part in the experimental setup (A) and in the FE environment (B).

Other boundary conditions are applied to the foot region of the devices, always for replicating the same conditions as in the experimental tests (figure 4.9) and assumed to be close to the real situation; as a first approach, a virtual encastre constraint was employed for keeping the foot part of the AFOs fixed in all the directions till a certain height of their geometry, which corresponds to the height of the used MDF blocks (figure 4.10). In order to study their impact on the stiffness measures, a second approach included the direct presence of a virtual representation of the MDF blocks in the simulations. A surface to surface contact between the AFOs and the MDF blocks was then necessary, while the MDF blocks and the AFOs sole parts were fully constrained (figure 4.11, figure 4.12). A third approach, instead, uses the same boundary conditions on the AFO soles as in the second approach, but without including the virtual representation of the MDF blocks (figure 4.13).

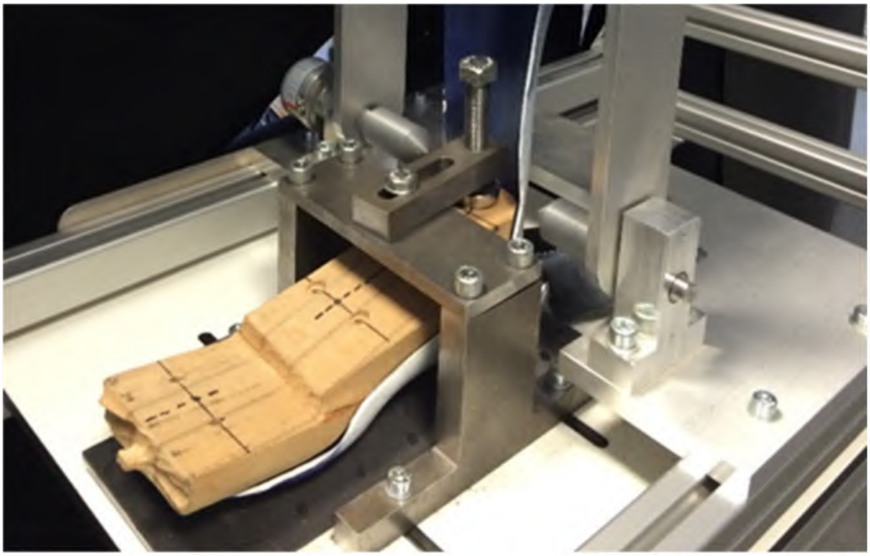

Figure 4.9: Full shell AFO constrained at the foot part in the experimental setup, by the use of the clamping system.

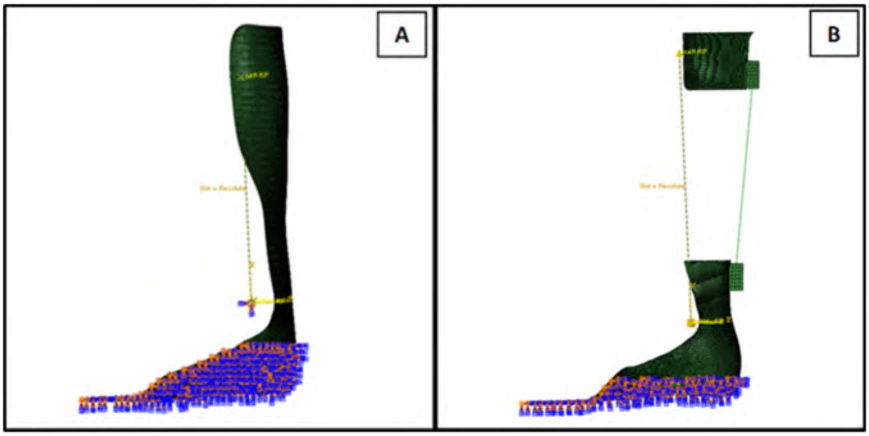

Figure 4.10: Encastre constraint applied at the foot part of the full shell (A) and the modular AFOs designs (B), during the first approach: the constraint on the AFO is applied according to the height of the MDF blocks used in the setup.

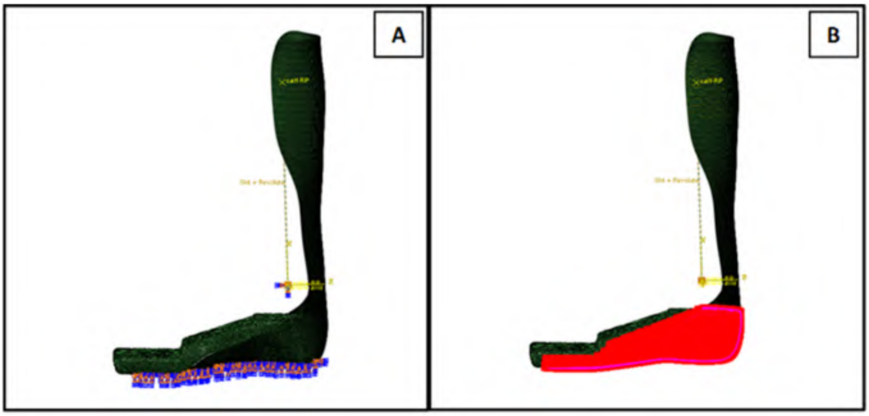

Figure 4.11: Full shell AFO design with the corresponding MDF block included in the simulation for the application of the second approach: encastre constraint (A) and surface to surface contact (B) applied between the AFO and the MDF block.

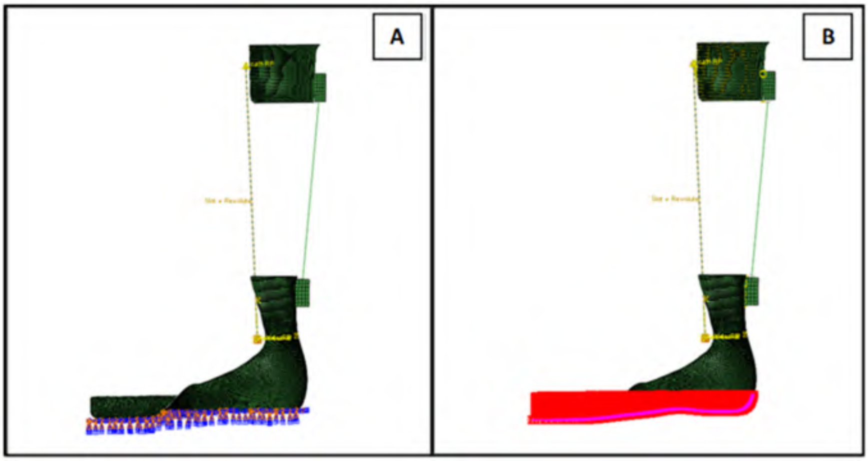

Figure 4.12: Modular AFO design with the corresponding MDF block included in the simulation, for the application of the second approach: encastre constraint (A) and surface to surface contact (B) applied between the AFO and the MDF block.

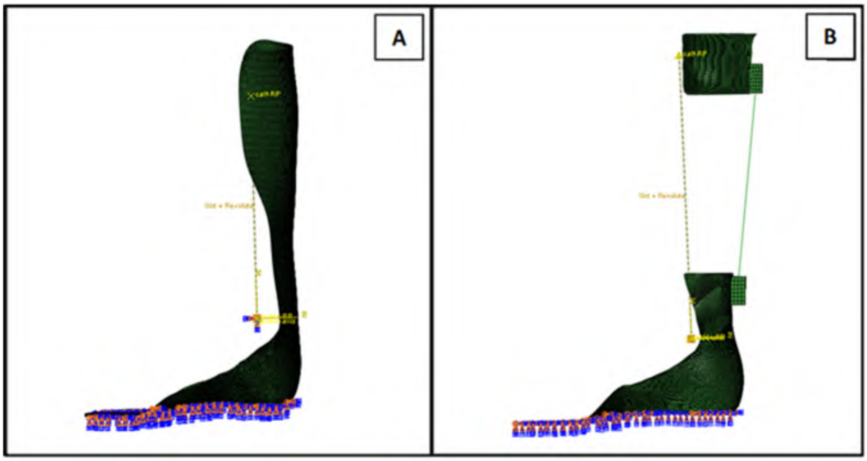

Figure 4.13: Full shell AFO design (A) and Modular AFO design (B) during the application of the third approach: the same boundary conditions on the AFO soles, as in the second approach, are used, but the MDF blocks are completely removed.

Concerning the application of the second approach, an encastre constraint was applied at the sole regions of all the AFOs (figure 4.11, (figure 4.12). When considering the MDF blocks, it is possible to see how the MDF block of the full shell AFO is relatively higher, in comparison to those used for the modular ones. Before the experiments, the MDF block for the full shell AFO was divided into three parts (low, middle and high), indicated in figure 4.14. The union of the low and the middle blocks was used during the experiments.

This height was also the one considered when the first approach was applied on this AFO ((figure 4.10). The high block, instead, was never used, but only reported for your knowledge.

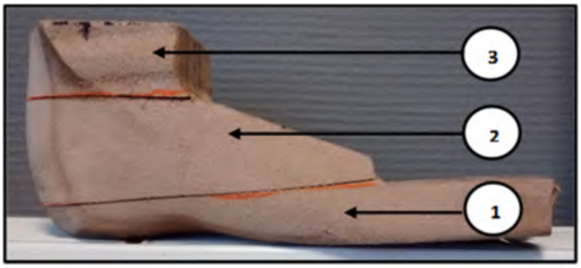

Figure 4.14: MDF block used for the full shell AFO design: it is composed of three parts called respectively low (1), middle (2) and high (3).

For the application of the second approach, it is important to define the master and the slave surfaces: since the MDF block is stiffer (E = 4 GPa and ν = 0.25) as compared to the AFO and we are interested in the influence of the contact on the AFO, the MDF block was chosen as the master surface while the AFO as the slave. To describe possible movements between the AFOs foot parts and the MDF blocks during their contact, interaction properties which describe the normal (hard contact) and tangential (friction coefficient = 0.8) behavior were also included.

As stated in Section 4.2.3, the PRF model is able to reproduce the hysteresis effects of the material given by the loading-unloading of the devices during the plantarflexion and dorsiflexion movements, which contribute to part of the total hysteresis. A second contribution, related to the energy dissipation, is induced by the interaction of the AFO with the test rig (i.e. the contact between the calf MDF blocks and the AFO) and between the components of the test rig itself (i.e. bearings on the shank axis). Mimicking these factors in a standardized manner is possible by specifying a friction coefficient for the connector along the sliding direction of the shank axis. Moreover, by specifying a damping coefficient for the connector allows representation of the forces resulting from the AFO straps around the calf part. This represents an artificial parameter used to describe the AFO conditions when the angular deflection is equal to zero; it is considered because the direct inclusion of the calf straps in the simulation would require specific material and contact properties, highly increasing the complexity of the model.

The values of the friction and damping coefficients, respectively equal to 0.3 and 30 N/mm/s, are chosen specifically and are the same for each AFO, in order to obtain a predictive and standardized FE framework applicable to each patient-specific AFO tested in the experimental setup. In fact, these parameters are calibrated on the AFOs considered in the current study and they can be extended to predict the behavior of other AFOs within the same range of stiffness.

A sensitivity study, performed on the AFO B, was realized to study the impact of friction and damping coefficients: it showed that, in case of an eventual extremely high friction coefficient equal to 1, it is still possible to obtain a maximum relative error of 7.82 % (table 4.6). In the same way, by using an extremely high damping coefficient, equal to 100 N/mm/s, also showed that an admissible relative error of 11.52 % can be obtained (table 4.7).

Table 4.6: Relative error between the computational and experimental ankle stiffness values of the AFO B when a friction value of 1 is used.

	PL	**DU**	**DL**	**DU**
Exp. [Nm/°]	3.42	3.08	3.15	2.97
Comp. [Nm/°]	3.51	3.09	3.41	3.03
Rel. error [%]	2.60	0.33	7.82	1.92

Table 4.7: Relative error between the computational and experimental ankle stiffness values of the AFO B when a damping coefficient of 100 N/mm/s is used.

	PL	**DU**	**DL**	**DU**
Exp. [Nm/°]	3.42	3.08	3.15	2.97
Comp. [Nm/°]	3.22	3.30	3.13	3.36
Rel. error [%]	6.35	6.68	0.48	11.52

In general, imposing friction and damping coefficients can have an impact on the resulting computational stiffness graphs of the AFOs. These friction-damping parts, which are indicated in (figure 4.15), are taken into account within the unloading parts when the stiffness values, obtained from the simulations, are calculated. Including these parts allows to obtain an optimal comparison, over the same range of motion, with the values obtained from the experimental graphs, which often present variable nonlinearities in unloading quadrants (figure 4.16).

Another approach could be to neglect the friction-damping parts and only consider the 75 % (or less) of both the computational and experimental curves but, since the extension of the nonlinearities is variable, and in some cases even for the entire unloading quadrants (figure 4.16), this operation might introduce higher errors when the computational and experimental curves are compared.

Concerning the experimental tests, because of the available equipment, the results were recorded with a sampling rate of 10 Hz at a velocity of 1 degree/s and then filtered with a 4th order low pass Butterworth filter with a cut-off frequency at 0.2 Hz. The outcomes in terms of moments and rotational angles are then used to calculate the ankle stiffness of each patient-specific AFO and compared with the experimental results.

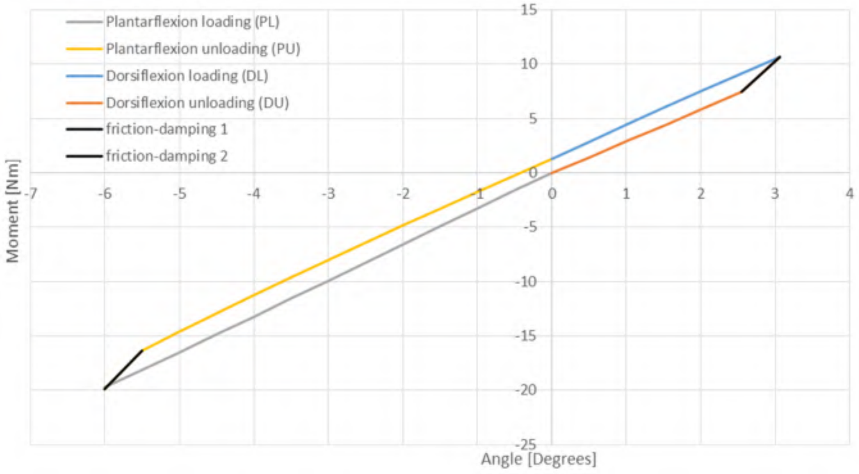

Figure 4.15: Example of an AFO stiffness graph derived from a simulation; the different parts are plantarflexion loading (PL), plantarflexion unloading (PU), dorsiflexion loading (DL), dorsiflexion unloading (DU), while, the parts due to the friction and damping effects are friction-damping 1 and 2.

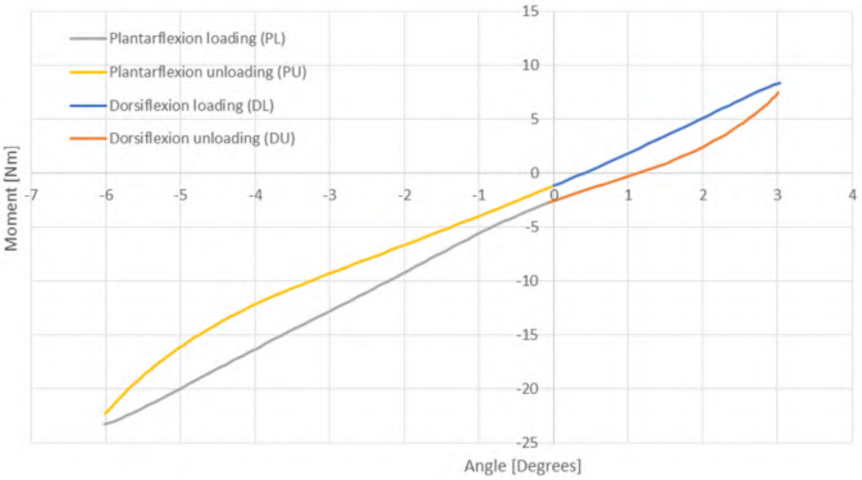

Figure 4.16: Example of an experimental AFO stiffness graph: it is possible to see how the nonlinearities affect the entire unloading quadrants.

4.3 RESULTS

This section contains the results obtained from the computational representation of the 3D printed AFOs. The overview starts from the results of the mesh sensitivity analysis which allowed to study how the number of elements in the mesh grid and the different element type influence the prediction of the ankle stiffness and the stress distribution. Afterwards, the comparison between the outcomes from the experimental setup and the simulations, when using the three boundary conditions approaches, is shown, in order to understand how using virtual MDF blocks could impact on the stiffness measures.

4.3.1 Mesh sensitivity analysis

A mesh sensitivity analysis was performed for assessing that a converged solution with the used mesh numbers (43000 – 65000 S4R elements) was obtained. The analysis was applied to the full shell AFO design for a range of 10 degrees in both dorsiflexion and plantarflexion (total range of 20 degrees). The study firstly focused on the impact of using quadrilateral shell meshes, realized with S4R elements, with a different number of the elements in the grid (values varying from 20500 S4R elements till 102500 S4R elements) and secondly on comparing different element types (quadrilateral shell elements S4R versus hexahedral solid elements C3D8R). In order to avoid hourglass problems, every hexahedral mesh was realized with 10 elements along the thickness (figure 4.17).

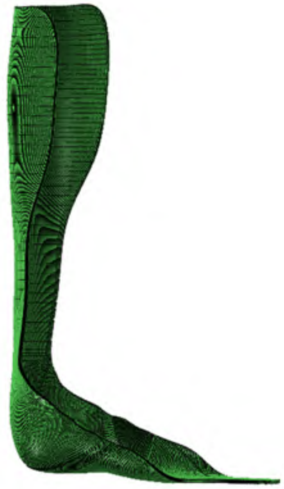

Figure 4.17: Example of full shell AFO realized with hexahedral C3D8R elements, used for the mesh sensitivity analysis.

The results in terms of a different number of the quadrilateral elements in the mesh grid are shown in figure 4.18: the stiffness graphs show that increasing the number of the elements has a rather small effect; the highest error is below 1 % in both dorsiflexion and plantarflexion. Small differences are also obtained when the maximal von Mises stress is considered, with percentages equal to 0.6 % in dorsiflexion and 1.5 % in plantarflexion (figure 4.19, figure 4.20).

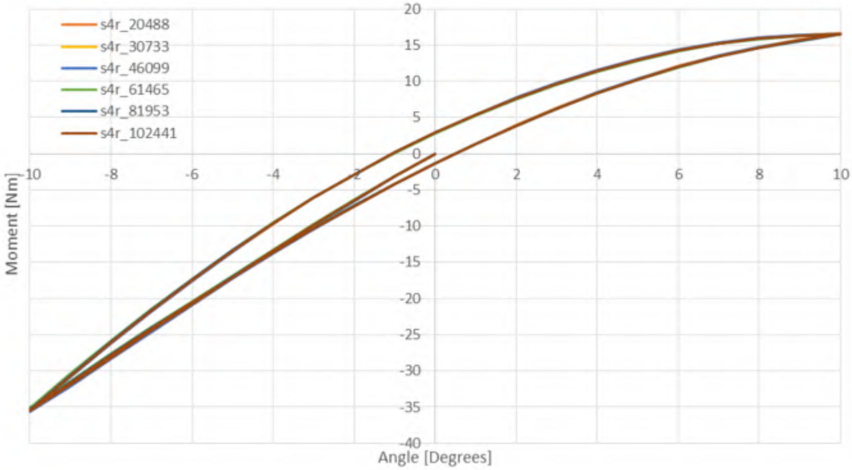

Figure 4.18: Comparison in terms of stiffness between quadrilateral AFO meshes with different element numbers in the grid.

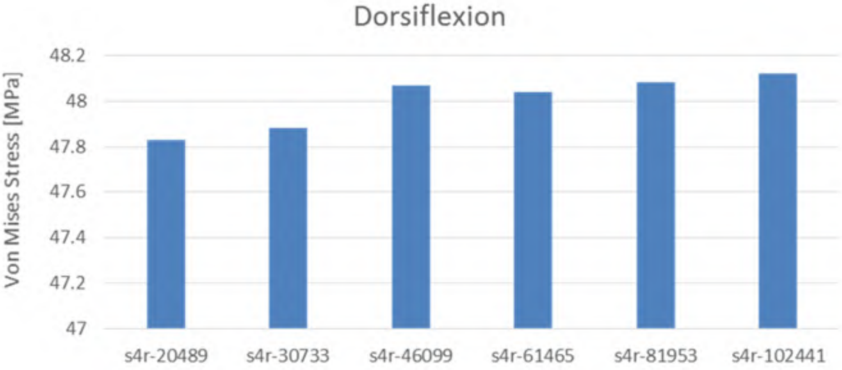

Figure 4.19: Comparison in terms of the von Mises stress between quadrilateral AFO meshes with different element numbers in the grid during dorsiflexion.

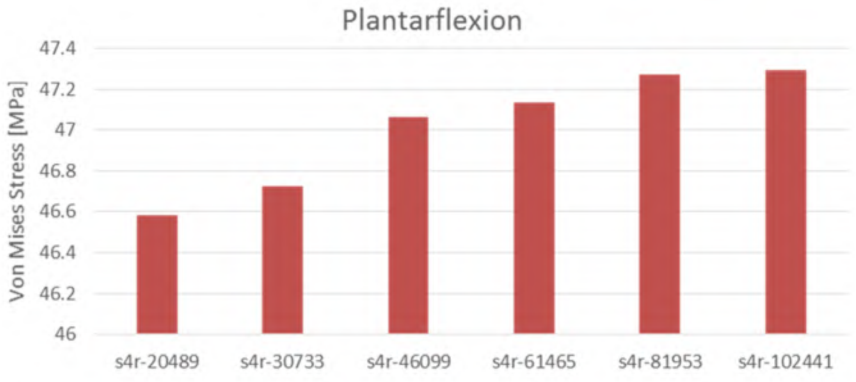

Figure 4.20: Comparison in terms of the von Mises stress between quadrilateral AFO meshes with different element numbers in the grid during plantarflexion.

When different element types (S4R and C3D8R) are compared, higher differences are found. In figure 4.21, it is possible to visualize the outcomes in terms of stiffness, which provide a maximal error of 3 %. The study of the von Mises stress, instead, shows the highest error percentages, which are equal to 0.9 % in dorsiflexion and 4.3 % in plantarflexion, both obtained in the worst case scenario (figure 4.22, figure 4.23).

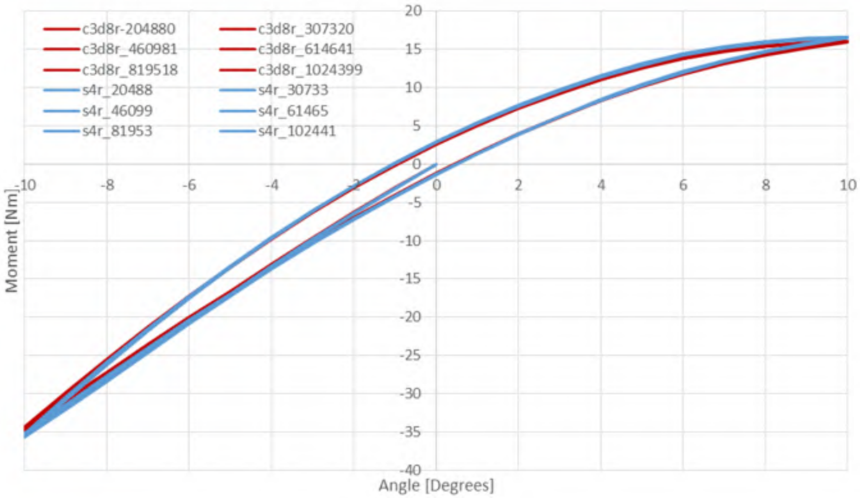

Figure 4.21: Comparison in terms of stiffness between quadrilateral (S4R) and hexahedral (C3D8R) AFO meshes with different element numbers in the grid.

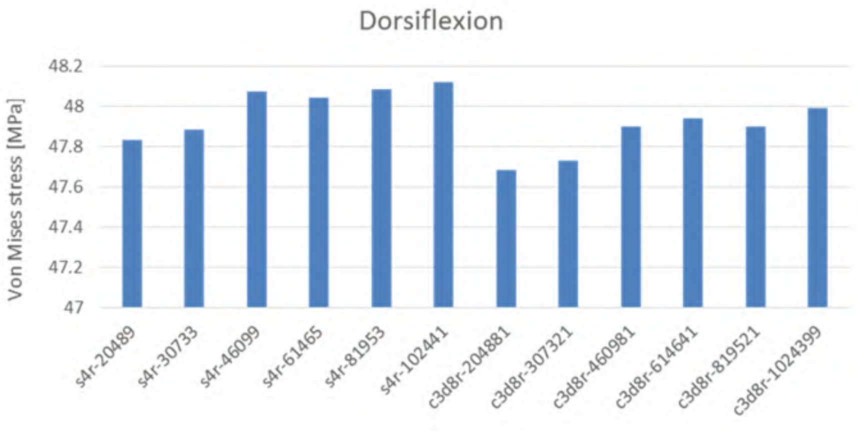

Figure 4.22: Comparison in terms of the von Mises stress between quadrilateral (S4R) and hexahedral (C3D8R) AFO meshes with different element numbers in the grid during dorsiflexion.

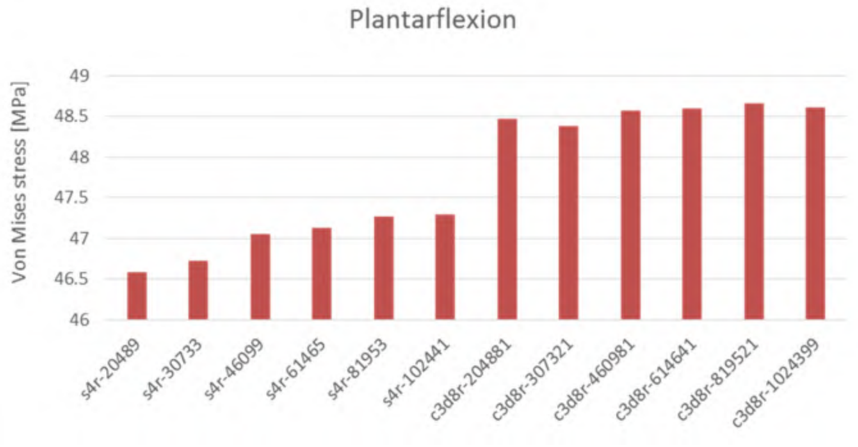

Figure 4.23: Comparison in terms of the von Mises stress between quadrilateral (S4R) and hexahedral (C3D8R) AFO meshes with different element numbers in the grid during plantarflexion.

The mesh sensitivity analysis reveals that the mesh numbers used for the realization of the FE models of the 3D printed AFOs are optimal for obtaining convergent solutions. In general, small differences are obtained when varying the number of the elements in the mesh grid, made with quadrilateral or hexahedral elements. The highest differences are obtained when evaluating the von Mises stress in plantarflexion between meshes realized with different element types (4.3 %), which is obtained for the worst case scenario. However, the obtained error can be considered acceptable and definitely promotes the use of the quadrilateral shell meshes. Their implementation will surely help reducing the computational time of the analysis, as highlighted in table 4.8, table 4.9, where the CPU time, when using S4R or C3D8R elements, is reported. It is possible to notice how, even when using the finest quadrilateral mesh, the duration of the analysis time is still satisfactory, while, in case of hexahedral meshes, it becomes not practical.

Table 4.8: CPU time needed when using quadrilateral (S4R) meshes with a different number of the elements in the grid.

Mesh type	CPU time
s4r 20489	10 min
s4r 30733	14 min
s4r 46099	20 min
s4r 61465	27 min
s4r 81953	35 min
s4r 102441	44 min

Table 4.9: CPU time needed when using hexahedral (C3D8R) meshes with a different number of the elements in the grid.

Mesh type	CPU time
c3d8r 204881	5.3 h
c3d8r 307321	8 h
c3d8r 460981	32 h
c3d8r 6164641	79 h
c3d8r 819521	144 h
c3d8r 1024399	200 + h

4.3.2 Validation

In this section, the comparison between the experimental and computational curves obtained for the four 3D printed AFOs, in case of the first boundary conditions approach, is shown.

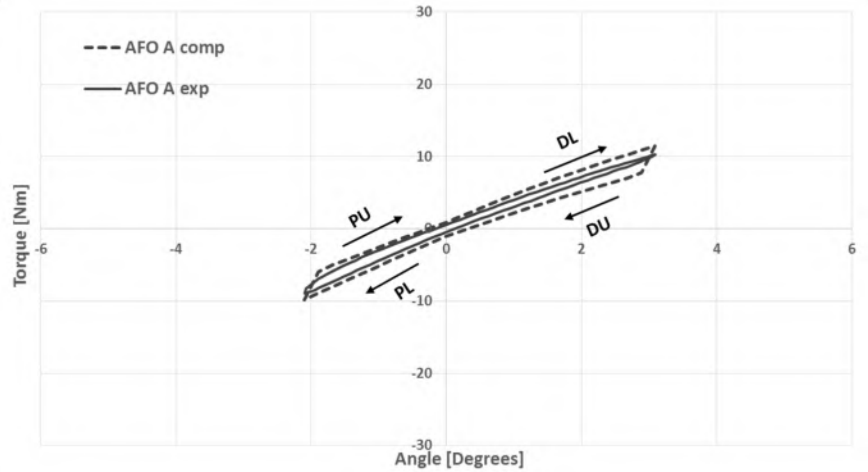

Figure 4.24: Comparison between the experimental (exp) and computational (comp) stiffness curves for the AFO A during Plantarflexion Loading (PL), Plantarflexion Unloading (PU), Dorsiflexion Loading (DL) and Dorsiflexion Unloading (DU).

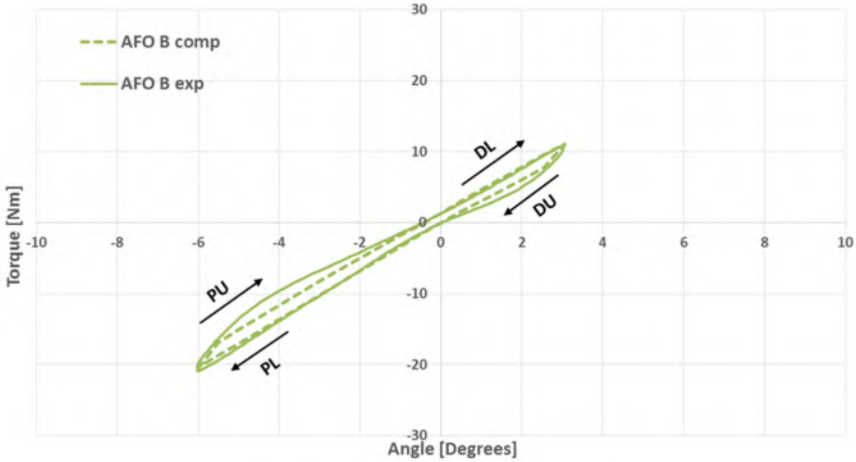

Figure 4.25: Comparison between the experimental (exp) and computational (comp) stiffness curves for the AFO B during Plantarflexion Loading (PL), Plantarflexion Unloading (PU), Dorsiflexion Loading (DL) and Dorsiflexion Unloading (DU).

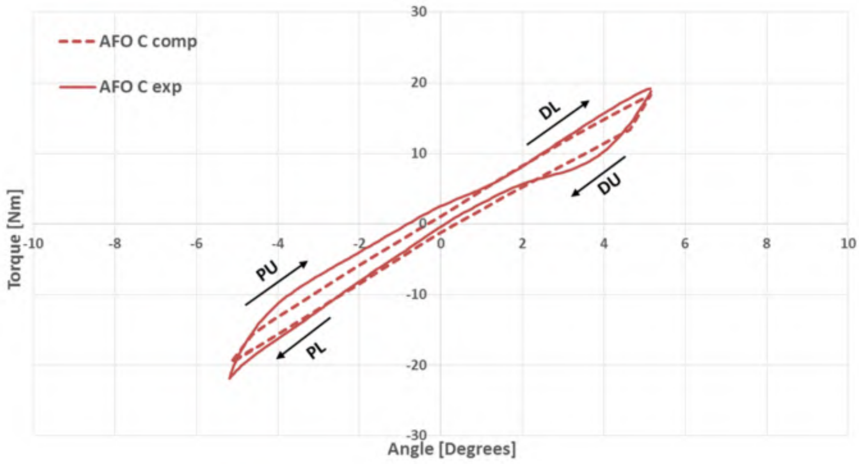

Figure 4.26: Comparison between the experimental (exp) and computational (comp) stiffness curves for the AFO C during Plantarflexion Loading (PL), Plantarflexion Unloading (PU), Dorsiflexion Loading (DL) and Dorsiflexion Unloading (DU).

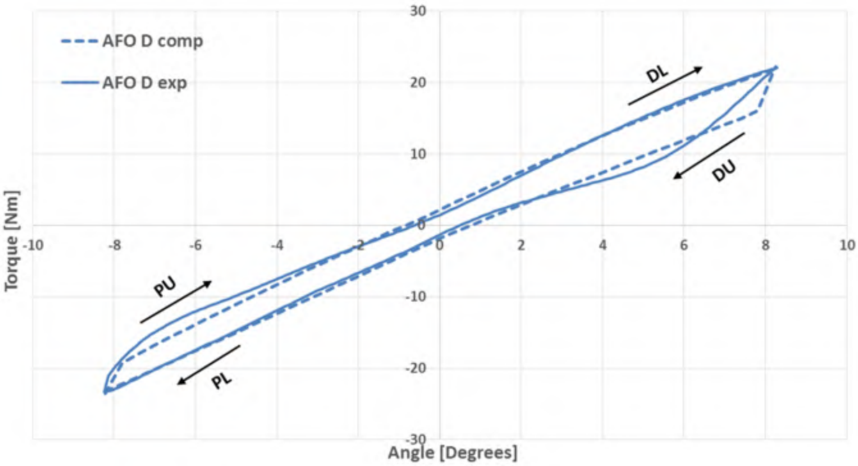

Figure 4.27: Comparison between the experimental (exp) and computational (comp) stiffness curves for the AFO D during Plantarflexion Loading (PL), Plantarflexion Unloading (PU), Dorsiflexion Loading (DL) and Dorsiflexion Unloading (DU).

Figure 4.24-figure 4.27 depict an overall good correlation for all the tested AFOs in their specific range of motion (table 4.5). All the curves show the presence of hysteresis and nonlinearities in the unloading phases. It is also possible to notice how all the devices behave differently in the plantarflexion and dorsiflexion quadrants, due to their shape. This is confirmed by the

analysis of the ankle stiffness values calculated for each quadrant of the graphs and summarized in table 4.10.

Table 4.10: Comparison between experimental and computational ankle stiffness results of the four AFOs during Plantarflexion Loading (PL), Plantarflexion Unloading (PU), Dorsiflexion Loading (DL) and Dorsiflexion Unloading (DU). The ranges of motion used for each AFO are contained in table 4.5.

	PL		PU		DL		DU	
AFO	**Exp.** [Nm/°]	**Comp.** [Nm/°]	**Exp.** [Nm/°]	**Comp.** [Nm/°]	**Exp.** [Nm/°]	**Comp.** [Nm/°]	**Exp.** [Nm/°]	**Comp.** [Nm/°]
A	4.00	3.95	4.00	4.40	3.23	3.35	3.48	3.47
B	3.42	3.40	3.08	3.34	3.15	3.21	2.97	3.28
C	3.94	3.60	3.69	3.68	3.21	3.42	3.01	3.32
D	2.69	2.62	2.42	2.68	2.64	2.50	2.41	2.38

AFO A seems to be the stiffest in plantarflexion whereas in dorsiflexion, AFO A, B and C have similar values. AFO D is the most flexible AFO in both dorsiflexion and plantarflexion. The visual agreement is confirmed by the data contained in table 4.11, which show the ability of the FE models to predict their mechanical behavior. This was achievable through the utilization of an advanced material model for the PA 12 in combination with the boundary conditions of the experimental setup, mimicking as closely as possible the behavior of the 3D printed AFOs without including the virtual representation of the MDF blocks.

Table 4.11: Absolute and relative errors for the ankle stiffness of the four patients AFOs during Plantarflexion Loading (PL), Plantarflexion Unloading (PU), Dorsiflexion Loading (DL) and Dorsiflexion Unloading (DU). The ranges of motion used for each AFO are contained in table 4.5.

	PL		PU		DL		DU	
AFO	**Abs. Err.** [Nm/°]	**Rel. Err.** [%]	**Abs. Err.** [Nm/°]	**Rel. Err.** [%]	**Abs. Err.** [Nm/°]	**Rel. Err.** [%]	**Abs. Err.** [Nm/°]	**Rel. Err.** [%]
A	0.05	1.34	0.40	9.88	0.12	3.84	0.02	0.47
B	0.02	0.61	0.26	8.58	0.07	2.11	0.31	10.30
C	0.33	8.45	0.01	0.36	0.21	6.61	0.31	10.38
D	0.10	2.31	0.26	10.66	0.14	5.42	0.03	1.33

4.3.3 Stress investigation

In addition to the calculation of the ankle stiffness for the four 3D printed AFOs, a stress investigation was performed. This allowed to study the values of stress reached by the patient-specific devices during their ranges of motion. Figure 4.28-figure 4.31 show the von Mises stress distribution for the four AFOs at the maximal dorsiflexion and plantarflexion. The full shell AFO is characterized by intermediate stress concentrations around the trimlines, while for the modular AFOs, the stress concentrations occur around the thicker blocks on the foot part that are connected to the CFRP rods.

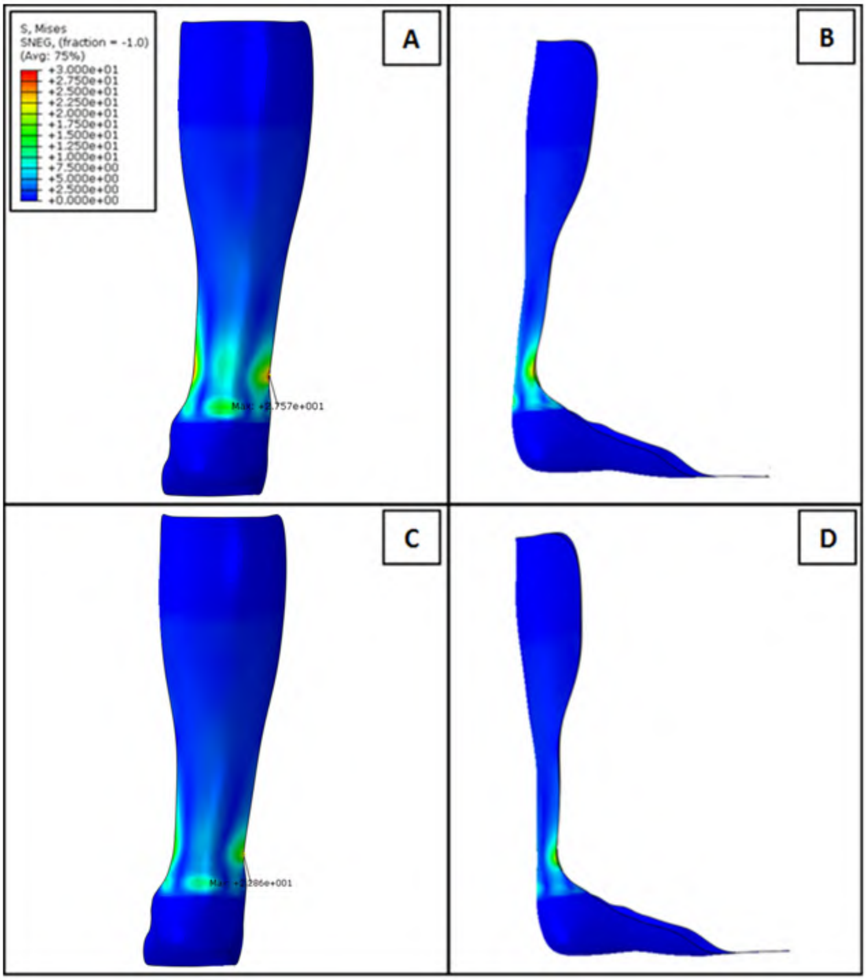

Figure 4.28: Back and side views of the von Mises stress distribution on the AFO A at the maximal dorsiflexion (A,B) and plantarflexion (C,D). The value of the highest stresses is also indicated: 27.57 MPa in dorsiflexion and 22.86 MPa in plantarflexion.

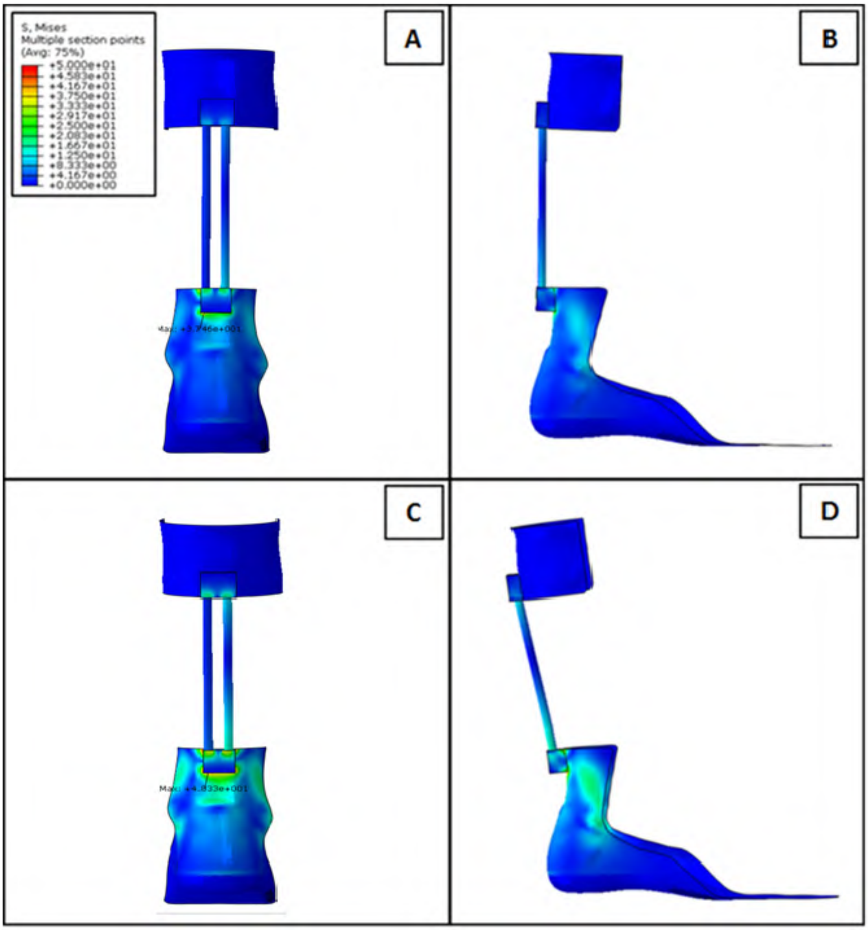

Figure 4.29: Back and side views of the von Mises stress distribution on the AFO B at the maximal dorsiflexion (A,B) and plantarflexion (C,D). The value of the highest stresses is also indicated: 37.46 MPa in dorsiflexion and 48.33 MPa in plantarflexion.

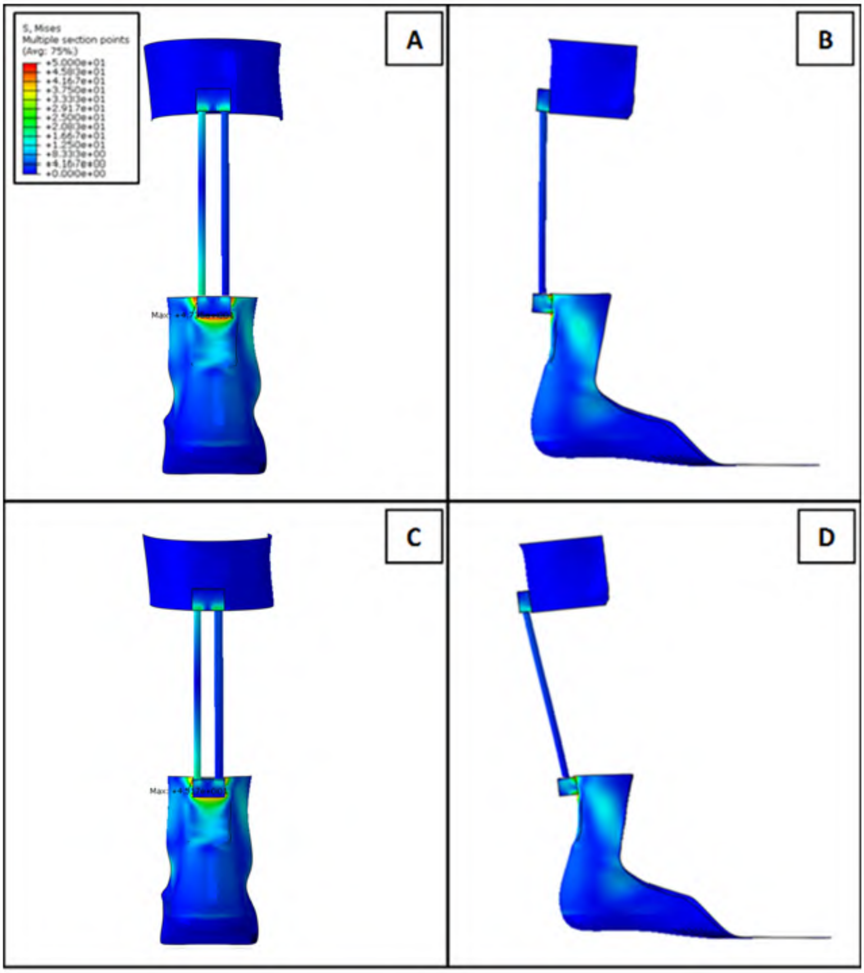

Figure 4.30: Back and side views of the von Mises stress distribution on the AFO C at the maximal dorsiflexion (A,B) and plantarflexion (C,D). The value of the highest stresses is also indicated: 47.35 MPa in dorsiflexion and 45.17 MPa in plantarflexion.

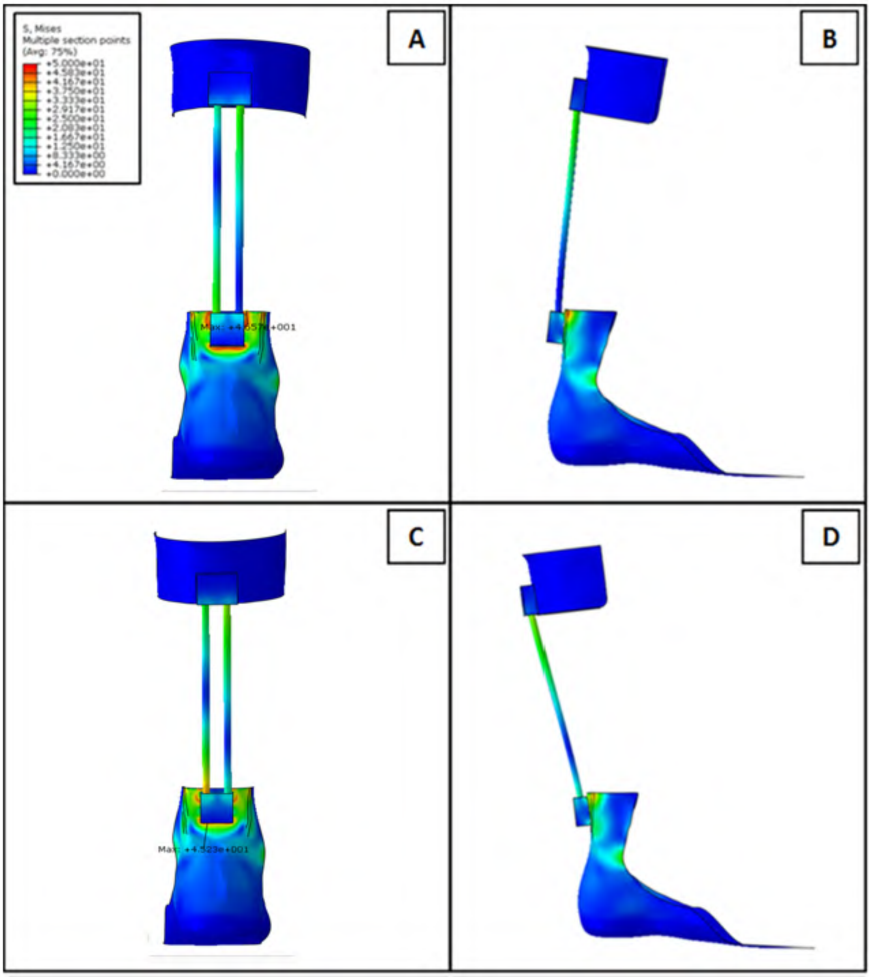

Figure 4.31: Back and side views of the von Mises stress distribution on the AFO D at the maximal dorsiflexion (A,B) and plantarflexion (C,D). The value of the highest stresses is also indicated: 46.57 MPa in dorsiflexion and 45.23 MPa in plantarflexion.

In dorsiflexion, the highest values of stress are reached by the AFO C (47.35 MPa) and D (46.57 MPa), while, in plantarflexion by the AFO B (48.33 MPa). Concerning the CFRP rods, which is stiffer (table 4.4) and has a failure stress value higher than PA 12 [128], the study of the stress in the fiber direction indicated lower values than the parts in PA 12. In general, the values shown by AFO B, C and D are higher than the ultimate strength value (equal to 34.096 MPa) indicated for PA 12 in table 4.3 A, which might cause the failure of the devices. Failure might also occur if inaccurate cutting and grinding of the rods is applied, which can result in alterations of their behavior [50].

4.3.4 Influence of the MDF blocks

The computational results used for the comparison with the experimental outcomes shown in section 4.3.2 consider a virtual representation of the devices when no contact with the MDF blocks is included. As explained in the boundary conditions section (4.2.4), this was defined as first approach, where the devices were totally encastred till the height of the MDF blocks used during the experimental tests. In this paragraph, instead, the second and third approach are applied, in order to show how the ankle stiffness of the four AFOs varies when a virtual representation of the MDF blocks is considered. Starting from the second approach, the comparison between the different AFO stiffness graphs is shown (figure 4.32-figure 4.35). Also in this case, it is possible to notice an overall good agreement, indicating adequate choice on how to mimic the real boundary conditions in the experimental setup.

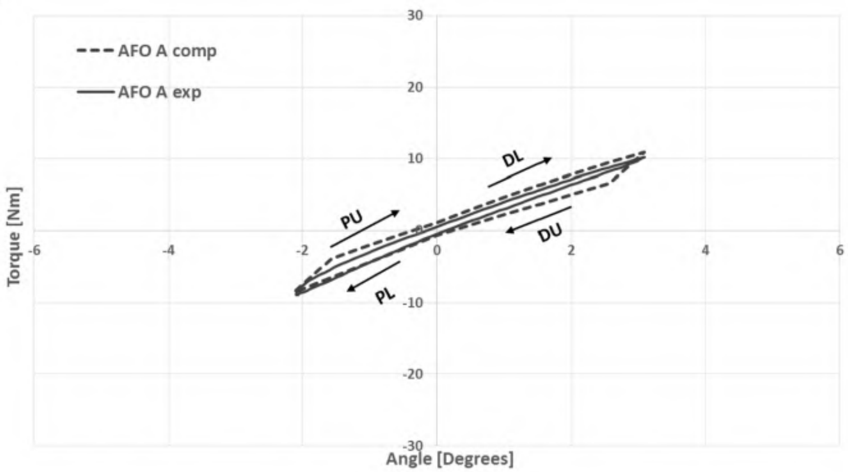

Figure 4.32: Comparison between the experimental (exp) and computational (comp) stiffness curves for the AFO A, when the virtual MDF block is included, during Plantarflexion Loading (PL), Plantarflexion Unloading (PU), Dorsiflexion Loading (DL) and Dorsiflexion Unloading (DU).

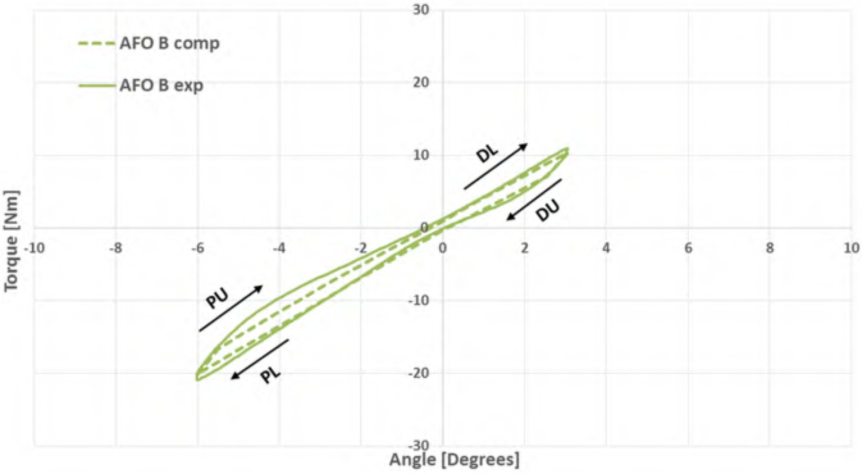

Figure 4.33: Comparison between the experimental (exp) and computational (comp) stiffness curves for the AFO B, when the virtual MDF block is included, during Plantarflexion Loading (PL), Plantarflexion Unloading (PU), Dorsiflexion Loading (DL) and Dorsiflexion Unloading (DU).

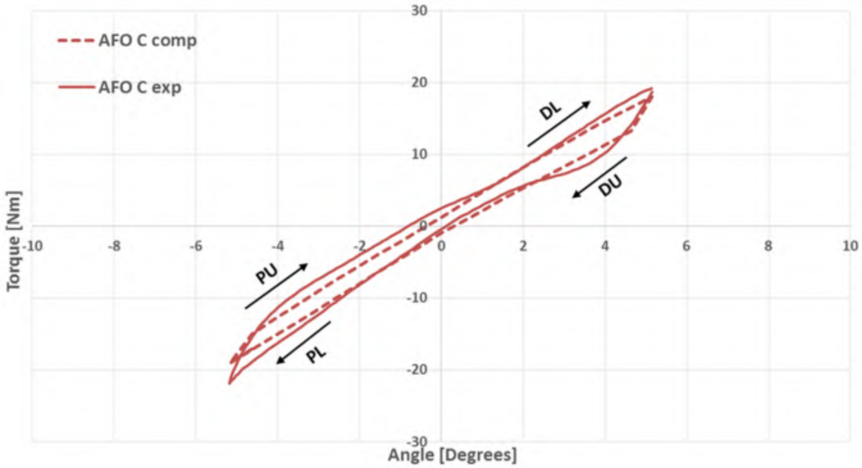

Figure 4.34: Comparison between the experimental (exp) and computational (comp) stiffness curves for the AFO C, when the virtual MDF block is included, during Plantarflexion Loading (PL), Plantarflexion Unloading (PU), Dorsiflexion Loading (DL) and Dorsiflexion Unloading (DU).

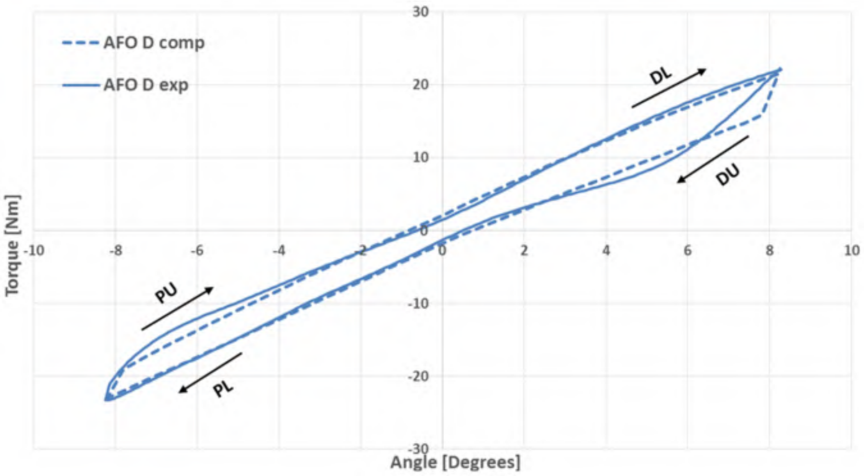

Figure 4.35: Comparison between the experimental (exp) and computational (comp) stiffness curves for the AFO D, when the virtual MDF block is included, during Plantarflexion Loading (PL), Plantarflexion Unloading (PU), Dorsiflexion Loading (DL) and Dorsiflexion Unloading (DU).

The graphical agreement is confirmed by the values contained in table 4.12 and table 4.13, which show percentage errors generally lower than 10 %, besides one case. In fact, for the AFO C in the PL quadrant, a percentage equal to 10.96 % was obtained, probably caused by the abnormal peak in the experimental curve, visible in figure 4.34.

Table 4.12: Comparison between experimental and computational ankle stiffness results of the four AFOs, when the virtual MDF blocks are used, during Plantarflexion Loading (PL), Plantarflexion Unloading (PU), Dorsiflexion Loading (DL) and Dorsiflexion Unloading (DU). The ranges of motion used for each AFO are contained in table 4.5.

	PL		PU		DL		DU	
AFO	**Exp. [Nm/°]**	**Comp. [Nm/°]**	**Exp. [Nm/°]**	**Comp. [Nm/°]**	**Exp. [Nm/°]**	**Comp. [Nm/°]**	**Exp. [Nm/°]**	**Comp. [Nm/°]**
A	4.00	3.66	4.00	4.16	3.23	3.18	3.48	3.36
B	3.42	3.28	3.08	3.22	3.15	3.09	2.97	3.14
C	3.94	3.50	3.69	3.55	3.21	3.35	3.01	3.24
D	2.69	2.60	2.42	2.64	2.64	2.46	2.41	2.34

The results in table 4.13 show that, by including the MDF blocks in the simulations, a decrease of the error percentages can be obtained, compared to the values summarized in table 4.11: this is especially visible for the AFO A in the PU quadrant, where the relative error drops from 9.88 % to 3.94%, for the AFO B in the PU and DU quadrants or the AFO C in the DU quadrant.

Table 4.13: Absolute and relative errors for the ankle stiffness of the four patients AFOs, when the virtual MDF blocks are used, during Plantarflexion Loading (PL), Plantarflexion Unloading (PU), Dorsiflexion Loading (DL) and Dorsiflexion Unloading (DU). The ranges of motion used for each AFO are contained intable 4.5.

	PL		PU		DL		DU	
AFO	**Abs. Err. [Nm/°]**	**Rel. Err. [%]**	**Abs. Err. [Nm/°]**	**Rel. Err. [%]**	**Abs. Err. [Nm/°]**	**Rel. Err. [%]**	**Abs. Err. [Nm/°]**	**Rel. Err. [%]**
A	0.34	8.54	0.16	3.94	0.05	1.54	0.13	3.67
B	0.14	4.02	0.14	4.66	0.06	1.84	0.17	5.61
C	0.44	10.96	0.14	3.52	0.13	4.47	0.22	7.75
D	0.09	3.26	0.22	8.92	0.18	6.86	0.07	2.95

In some case, an increase of the ankle stiffness values is encountered, i.e. for the AFO A and B in the PL quadrant; however, these errors are still below 10 % and thus negligible, respectively 8.54 % and 4.02 %.

The main difference in including the contact between the AFO and the virtual MDF blocks is that the elements on the back part of the AFO mesh are not totally constrained but they are enabled to move; this doesn't apply for those on the sole which are still completely constrained. The effect of this application is clearly visible during dorsiflexion where the AFO elements impact with the MDF block during the deflection and tend to decrease the error in the results; the same effect is not always visible for the results during plantarflexion loading, where the movement of the AFO, away from the MDF block, should introduce a gap, that increases with the rotation.

More specifically, if we consider the case of the AFO A (figure 4.36), by comparing the outcomes when the first and the second approach are applied, we can notice that the gap reached between the elements of the AFO in contact with MDF block at the maximal rotation in plantarflexion (figure 4.36, item F) is small (approximately equal to 0.1 mm) and that the correspondent values of stress and strain on the elements, which are totally constrained in the first approach, are also small (figure 4.36, item B-D). However, a certain difference is visible between the stiffness values calculated at the maximal plantarflexion by using the two different approaches, but, probably due to the small amplitude of the imposed patient-specific rotation (2 degrees), it is not possible to see high differences between the considered variables.

By considering the case of the AFO B (figure 4.37), the gap between the AFO and the MDF block at the maximal plantarflexion is also small (figure 4.37, item F), but more spread on the heel part of the AFO, which can explain the 3.5 % increase of the relative error in the plantarflexion loading quadrant and, at the same time, the 4 % decrease during the unloading phase, in comparison to the data obtained when the first approach was used (table 4.11).

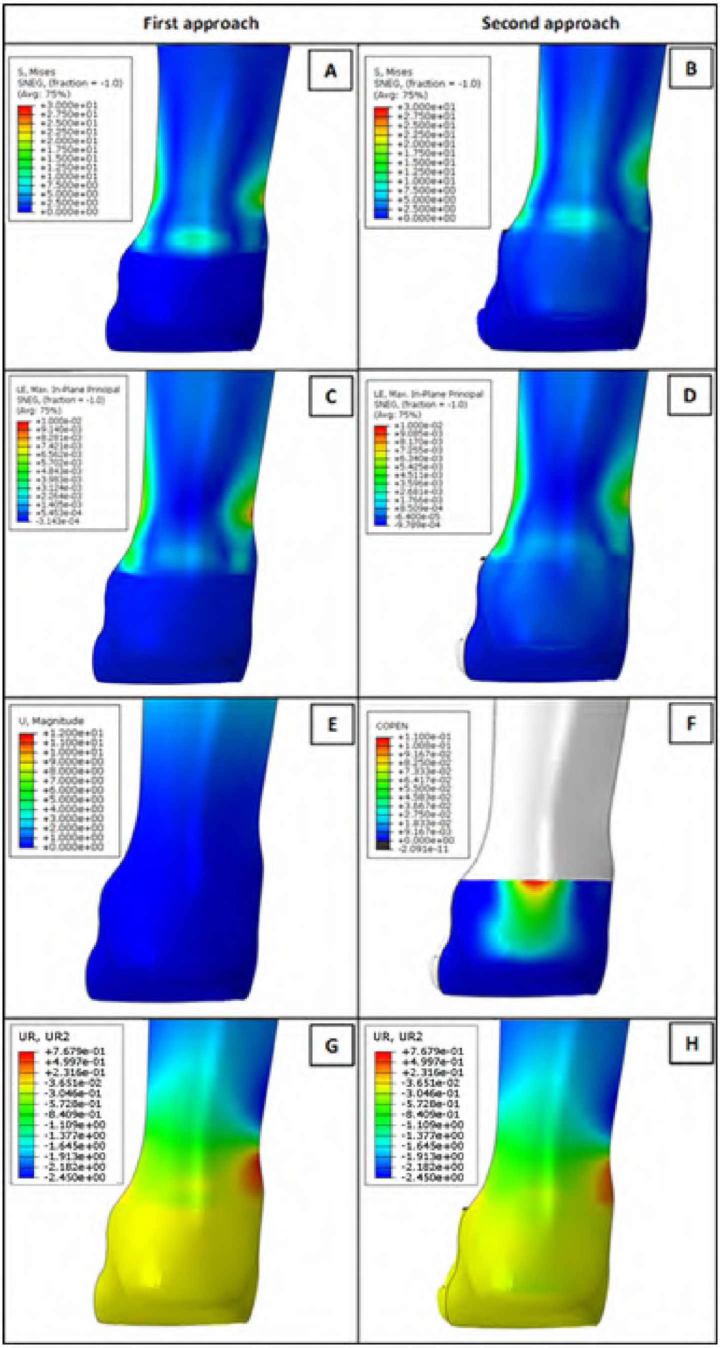

Figure 4.36: Comparison in terms of stress [MPa], strain [-], displacement [mm] and rotations [degrees] between the results obtained on the AFO A at the maximum plantarflexion when applying the first (A, C, E, G) and the second approach (B, D, F, H). The variable COPEN [mm], contained in the item F, represents the displacement of the elements of the AFO, which are initially in contact with the MDF block.

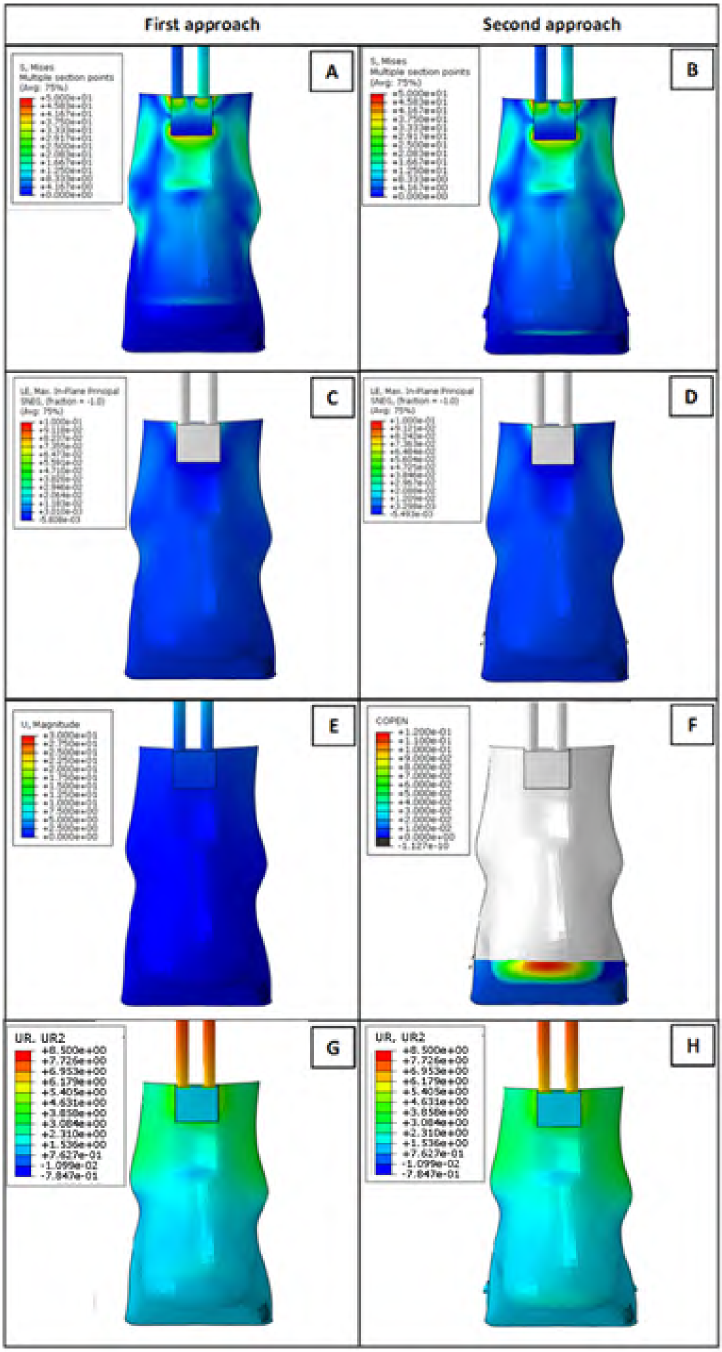

Figure 4.37: Comparison in terms of stress [MPa], strain [-], displacement [mm] and rotation [degrees] between the results obtained on the AFO B at the maximum plantarflexion when applying the first (A, C, E, G) and the second approach (B, D, F, H). The variable COPEN [mm], contained in the item F, represents the displacement of the elements of the AFO, which are initially in contact with the MDF block.

In general, virtually mimicking the contact of the AFO meshes with the MDF blocks, as in the second approach, permits to obtain lower errors than using a complete constraint on the sole regions of the AFOs, as in the first approach. However, the second approach would cause the decrease of the computational efficiency. In fact, the MDF blocks are meshed with solid linear tetrahedral (C3D4) elements and solving the contact problem between the AFO and the blocks require a higher CPU time which can even reach 12 hours in some cases, as experienced for the AFO D (table 4.14). This estimation could further increase if solid elements (i.e. C3D8R) would be used for the meshes of the AFOs.

Table 4.14: CPU time required for the virtual analysis when the contact between the AFOs and the MDF blocks was considered.

AFO	AFO mesh elements	MDF block mesh elements	CPU time
A	46099 S4R	291308	2 hours
B	64836 S4R	158549	3 hours
C	43636 S4R	151313	1 hour
D	44332 S4R	517095	12 hours

Concerning the third approach, the same boundary conditions used for the second approach are applied on the sole of the AFOs, but without a virtual representation of the MDF blocks. The results of this comparison are contained in table 4.15-table 4.16. It is possible to see how the relative error highly increases for the AFO A, while for the other AFOs the error values are still acceptable. This can be explained by visualizing the rotation that the AFO undergoes, i.e. at the maximal plantarflexion, which provokes lower values of torque, compared to the other two approaches (figure 4.38, item L, M, N). In particular, the absence of the block or constraints allows more rotation on the back part of the AFO, while in the first and second approach, the total constraint and the block limit the movement of the AFO; this is accentuated by the higher movement around the trimlines, in proximity of the ankle zone, which is not observed for the third approach.

Table 4.15: Comparison between experimental and computational ankle stiffness results of the four AFOs, when the third approach is applied, during Plantarflexion Loading (PL), Plantarflexion Unloading (PU), Dorsiflexion Loading (DL) and Dorsiflexion Unloading (DU). The ranges of motion used for each AFO are contained in table 4.5.

	PL		**PU**		**DL**		**DU**	
AFO	**Exp. [Nm/°]**	**Comp. [Nm/°]**	**Exp. [Nm/°]**	**Comp. [Nm/°]**	**Exp. [Nm/°]**	**Comp. [Nm/°]**	**Exp. [Nm/°]**	**Comp. [Nm/°]**
A	4.00	2.73	4.00	3.19	3.23	2.26	3.48	2.48
B	3.42	3.27	3.08	3.19	3.15	3.04	2.97	3.09
C	3.94	3.48	3.69	3.53	3.21	3.30	3.01	3.19
D	2.69	2.59	2.42	2.62	2.64	2.44	2.41	2.33

Table 4.16: Absolute and relative errors for the ankle stiffness of the four patients AFOs, when the third approach is applied, during Plantarflexion Loading (PL), Plantarflexion Unloading (PU), Dorsiflexion Loading (DL) and Dorsiflexion Unloading (DU). The ranges of motion used for each AFO are contained in table 4.5.

	PL		**PU**		**DL**		**DU**	
AFO	**Abs. Err. [Nm/°]**	**Rel. Err. [%]**	**Abs. Err. [Nm/°]**	**Rel. Err. [%]**	**Abs. Err. [Nm/°]**	**Rel. Err. [%]**	**Abs. Err. [Nm/°]**	**Rel. Err. [%]**
A	1.28	31.94	0.81	20.23	0.96	29.90	1.01	28.27
B	0.16	4.58	0.12	3.87	0.11	3.52	0.12	4.13
C	0.45	11.51	0.16	4.42	0.09	2.65	0.19	6.22
D	0.10	3.69	0.20	8.21	0.20	7.39	0.08	3.27

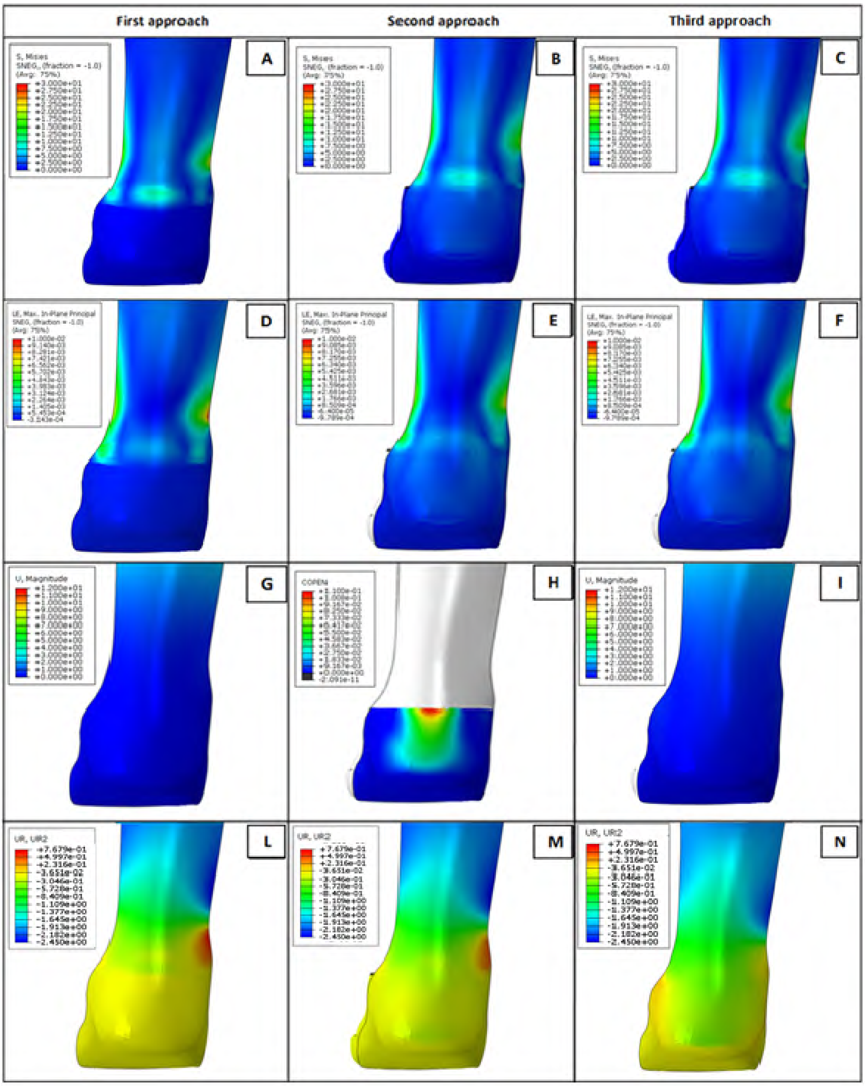

Figure 4.38: Comparison in terms of stress [MPa], strain [-], displacement [mm] and rotation [degrees] between the results obtained from the AFO A at the maximum plantarflexion when applying the first (A, D, G, L), the second (B, E, H, M) and the third approach (C, F, I, N). The variable COPEN [mm], contained in the item F, represents the displacement of the elements of the AFO, which are initially in contact with the MDF block.

In order to provide a complete overview on the results obtained from the application of the three boundary conditions approaches on the four AFOs, figure 4.39-figure 4.42 are provided.

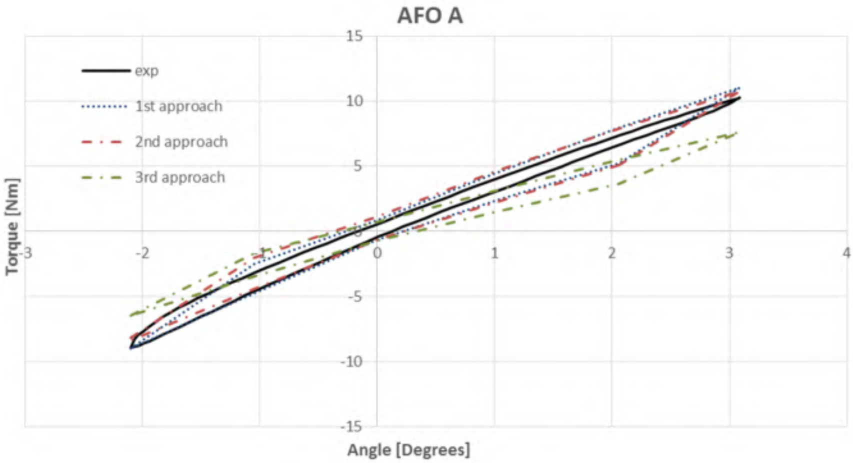

Figure 4.39: Stiffness curves obtained from the application of the three boundary conditions approaches on the AFO A: black solid line for the experimental curve; blue round dot curve for the first approach, red square dot curve for the second approach and green dash dot curve for the third approach.

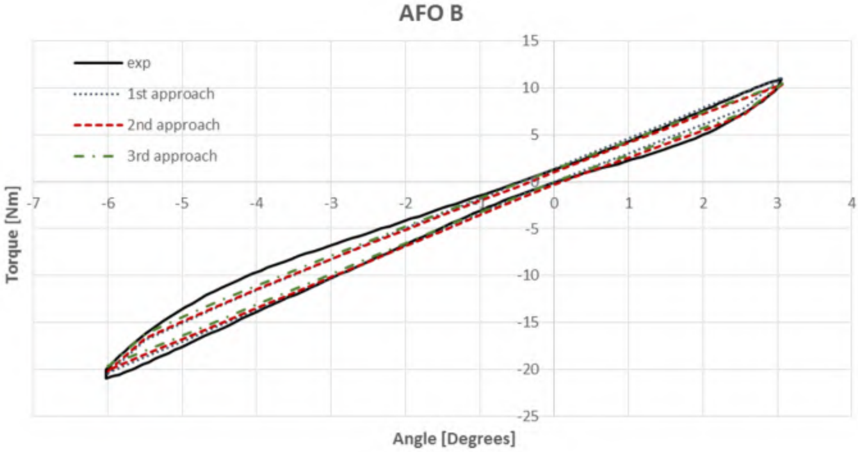

Figure 4.40: Stiffness curves obtained from the application of the three boundary conditions approaches on the AFO B: black solid line for the experimental curve; blue round dot curve for the first approach, red square dot curve for the second approach and green dash dot curve for the third approach.

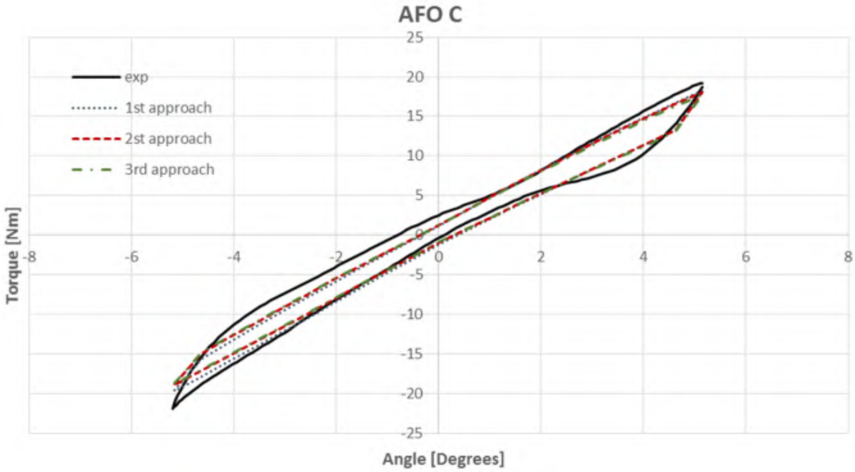

Figure 4.41: Stiffness curves obtained from the application of the three boundary conditions approaches on the AFO C: black solid line for the experimental curve; blue round dot curve for the first approach, red square dot curve for the second approach and green dash dot curve for the third approach.

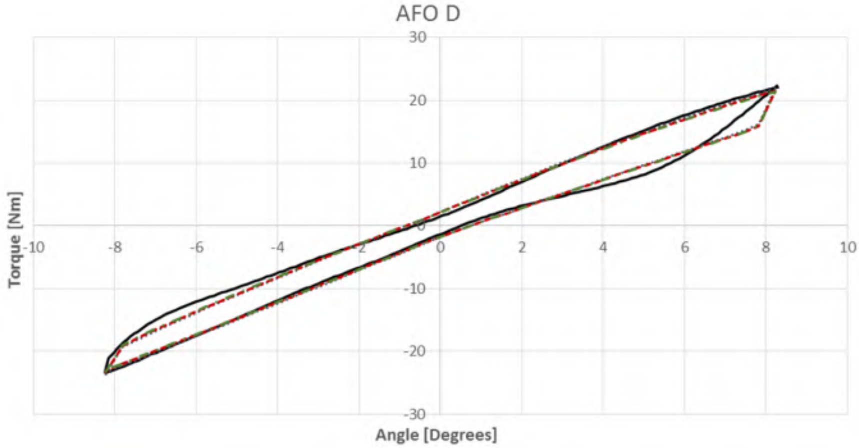

Figure 4.42: Stiffness curves obtained from the application of the three boundary conditions approaches on the AFO D: black solid line for the experimental curve; blue round dot curve for the first approach, red square dot curve for the second approach and green dash dot curve for the third approach.

4.4 DISCUSSION AND CONCLUSIONS

This chapter presented the creation of a standardized framework where, four finite element models of patient-specific 3D printed AFOs were developed for the evaluation of their ankle stiffness and the stress distribution during the second rocker of stance phase of the gait. The comparison with the results coming from the experimental setup, described in Chapter 3, allowed the validation of the computational models. The rationale behind this is to further create a scientifically robust method to design and manufacture AFOs with specific mechanical properties in a reliable and repetitive way, applicable under several working conditions. The finite element models, in fact, can be used in combination with optimization algorithms in order to speed up the design and realization of more effective 3D printed AFOs.

The developed modelling strategy gives a good indication of the AFO ankle stiffness and stress distribution. Dedicated algorithms, which provide high flexibility for the mesh creation, were developed in pyFormex to convert STL files, describing the AFO geometry and used for 3D printing, into high quality finite element models. Solving the numerical problem with Abaqus would require an acceptable time if quadrilateral shell elements and a total encastre constraint on the AFOs sole region (first approach) are used (table 4.8-table 4.9). The computational time increases if a virtual representation of the MDF blocks (second approach) would be included (table 4.14), but at the same time this allows to obtain lower values of error during the validation process (table 4.13).

In general, the FE models showed a good overall agreement with the experimental data, whether the first, the second or the third approach were used (figure 4.39-figure 4.42). Four different ankle stiffness values are used for each quadrant of the angle vs. torque graph, as most of the patient-specific AFOs show a different behavior in plantarflexion compared to dorsiflexion, due to their shape. The magnitude of these stiffness values is in line with the results obtained from other research groups ([113], [58]), which have also investigated 3D printed AFOs. AFO A seems to be the stiffest in plantarflexion whereas in dorsiflexion, AFO A, B and C have similar values. AFO D is the most flexible AFO in both dorsiflexion and plantarflexion.

The visual agreement is confirmed by the calculation of the error percentages (table 4.11, table 4.13, table 4.16), which show the ability of the FE models to predict the AFOs mechanical behavior. This was achievable through the utilization of advanced material properties for the PA 12 in combination with the boundary conditions used in the experimental setup, expressed by three different approaches, in order to mimic as closely and efficiently as possible the behavior of the 3D printed AFOs. High differences were only found for the AFO A when the third approach was used (table 4.16), which make us think that its application would not be appropriated when high MDF blocks are used. For this reasons, expressing the AFOs boundary conditions as a total constraint without the inclusion of the MDF blocks could be a good compromise in order to obtain indicative stiffness results with an acceptable relative error in a short analysis time. The computational time would eventually increase if 3D solid elements would be used for the realization of the meshes of the devices, as highlighted from the results of the mesh sensitivity analysis shown in table 4.8, table 4.9. For the same reasons, quadratic elements were also excluded, since they would have a huge impact on the time efficiency.

If using the second approach when high ranges of motion are imposed, a modification of the boundary conditions might be needed: currently they require the fully fixation of the MDF block and AFO sole parts, but, for high ranges of motion, a certain lifting of the AFO sole might be experienced when testing the device in the reality. This could require a different application of the virtual boundary conditions, for example by imposing a certain pressure on the upper surface of the MDF block to constrain the AFO on the ground, while allowing more degrees of freedom to the AFO sole. At the same time this requires that new contact properties need to be defined in order to calibrate the interaction between the AFO and the ground, increasing the complexity of the models. In addition the calibration would require the execution of dedicated experimental tests but this falls outside the scope of this work.

All the stiffness plots showed the presence of hysteresis: the hysteresis area represents the dissipated energy as heat during the deformation (loading) and the recovery phases (unloading). This is dependent upon the strain rate employed to deform the devices [121] constructed from PA 12, which has visco-elasto-plastic properties [67], and by the friction present between the AFO and the test rig and between the components of the test rig itself, which need to be considered when the finite element analysis is executed. For this reason both friction and damping coefficients were used. As the focus of the current study was to derive the ankle stiffness values, friction was not calculated experimentally but chosen by curve fitting, based on the experimental data. Its contribution could be lowered by further modifications to the design of the experimental setup, i.e. by modifying the clamping system or increasing the lubrication between the different components of the setup, which have been considered during the development of the new version of the experimental setup (see Chapter 5).

The damping coefficient instead is an artificial parameter, which has no testing equivalent, used to represent the action of the calf straps on the AFO when the angular deflection, applied by the linear motor, is equal to zero. The calf straps, in fact, exert a certain force on the AFO, which needs to be considered in the computational model. Since their direct inclusion in the computational environment would highly increase the model complexity (material properties, contact properties etc.), this artificial parameter was chosen in order to represent their constant action. If not included, the angle vs torque graph would have a triangular profile (since the force acting on the AFO would be equal to zero when there is no deflection), while by expressing it, a regular width of the graph is maintained.

By using one friction and damping coefficient for all the AFOs under investigation allow standardization and calibration of the computational framework, where the prediction is only depending on the shape and geometry of the patient-specific devices. This permits to extend the application of the framework to the prediction of the behavior of other AFOs. A sensitivity study, performed on the AFO B, showed that, in case of an eventual high friction coefficient equal to 1, it is still possible to obtain a maximum relative error of 7.82 % (table 4.6). In the same way, by using a high damping coefficient, equal to 100 N/mm/s, also showed that an admissible relative error of 11.52 % can be obtained (table 4.7). In general, the presence of hysteresis due to friction and the nonlinear behavior of the devices affects most of the ankle stiffness values in the unloading phases, which might cause overestimations of the calculated stiffness values. By decreasing the friction effect present in the experimental setup, would be possible to decrease the hysteresis area.

In figure 4.28-figure 4.31, the von Mises stress distribution for the four AFOs is depicted. For the AFO A, which has a full shell design, the highest stresses are concentrated around the trimlines around the ankle joint, while for the modular AFOs, the highest stresses are concentrated around the thicker blocks on the foot part that are connected to the CFRP rods. Since this is a preliminary analysis, further tests are needed to confirm if these stress values will cause the failure of the devices [50]. For evaluating the stress on the rods made in CFRP, which is stiffer (table 4.4) and has a failure stress higher than PA 12 [128], the stress in the fiber direction was studied. This showed stress values lower than the parts in PA 12. Deckers et al. [50] also showed that failure might occur if inaccurate cutting and grinding of the rods is applied, which can alter their behavior.

The FE analysis performed in this study takes into account only one loading cycle for each patient-specific AFO. The material model, in fact, is able to mimic the behavior of the devices during a static analysis, but it is not designed to predict the response of the devices during fatigue. However, the information coming from the computational models is useful to identify the zones of the devices subjected to the highest stress values; if distributed values higher than 25 MPa (fatigue threshold identified within the project framework by tests on samples of PA 12) are encountered on the AFO geometry, they might cause failure of the devices, but, below this value, no fatigue issues

were observed. Therefore, this threshold value can be used as a limit to be considered during the design process of the devices in combination with the optimization algorithms.
In order to further enhance the accuracy of the model (i.e. the nonlinearities during unloading), the straps used to fix the patients' leg on the AFO could have been modeled; as anticipated, this would increase the complexity of the model (i.e. material model for the straps, contact properties between AFO and straps etc.) and further decrease the (time) efficiency. In addition, the use of dynamic friction and damping coefficients would decrease the percentage errors but, at the same time, make the framework less predictive and standardized if one would calibrate these values for each AFO individually.
Because of the available instrumentation within the experimental setup, it was only possible to perform tests at a speed of 1 °/s: this could be considered a limitation since, in the gait lab, patients even reach velocities in the range of 50 °/s – 100 °/s while walking; however, by visualizing the results of tensile tests (figure 4.43), carried out from samples of PA 12 and used to derive the parameters used for the material computational model [67], some assumptions can be made. In fact, it's noticeable how increasing the testing speed from 5 mm/min to 500 mm/min resulted in an increase of the Young's modulus of about 8 %.

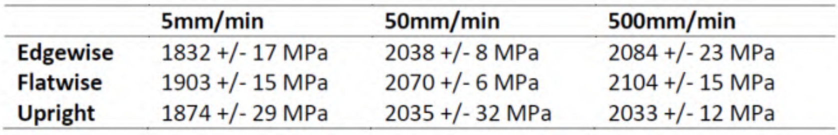

	5mm/min	50mm/min	500mm/min
Edgewise	1832 +/- 17 MPa	2038 +/- 8 MPa	2084 +/- 23 MPa
Flatwise	1903 +/- 15 MPa	2070 +/- 6 MPa	2104 +/- 15 MPa
Upright	1874 +/- 29 MPa	2035 +/- 32 MPa	2033 +/- 12 MPa

Figure 4.43: Young's modulus derived from tensile tests on samples of PA 12 using different testing speeds (adapted from [67]).

This consideration can be assumed, as first approximation, to be similar to an increase of the AFO testing speed from 1 °/s to 100 °/s; for example, taking into account an AFO with a stiffness value of 3 Nm/°, this would eventually imply an increase in stiffness of 0.24 Nm/°. Therefore, this small contribution can be taken into account when the AFO stiffness is prescribed for the patients during the clinical assessment, as not a single value but a range of stiffness values would be indicated, since the patients use adaptive movement strategies to the AFO usage [64]. However, in the future, the use of a new equipment will allow the comparison for speed values closer to those seen during gait.
As anticipated, the computational models, described in this chapter, allowed the representation of the mechanical behavior of the 3D printed AFOs during the second rocker of the gait by quantifying their ankle stiffness and stress

distribution. No virtual representation of the patient leg was included and therefore it was not possible to quantify the impact of the contact between the AFO and the patient leg on the stiffness measures. Its inclusion would have allowed to have results closer to reality, but at the same time it highly increases the complexity of the model since the material and contact properties of each part need to be considered and this falls out of the scope of the thesis. The goal, in fact, was to create a computational framework to have a pure indication of the mechanical behavior of the devices, which can be used in the design process and that can be extended to represent other conditions. In addition, the obtained outcomes could also be used for the realization of rigid body kinematics simulations of the lower limb of the patients and predict how the gait pattern changes in case of using a specific stiffness value. Nevertheless the virtual representation of the leg of the patients will be taken into account in the future studies.

In conclusion, this chapter permitted to highlight how the use of advanced computer modelling algorithms together with 3D printing techniques constitutes a strong combination acting to improve the design process of the AFOs and represents a big step for the future prediction of the AFOs behavior in case of other pathological conditions.

IV

Conclusions and future work

Chapters

CHAPTER 5

CONCLUSIONS AND FUTURE WORK

5.1 GENERAL DISCUSSION

The continuous application of additive manufacturing technologies in many sectors, such as the biomedical, automotive and aeronautical sector, is showing the validity of these techniques in helping the improvement of the manufacturing processes in terms of time and production efficiency, due to their ease of use, flexibility and affordable price. They guarantee consistency of shape and dimension, which are previously established in a STL file, where the geometry of the 3D object is created. Their combination with the finite element modelling techniques could supply a stronger tool, since they showed the ability of predicting the behavior of patient-specific devices by the simulation of various loading and boundary conditions. In fact, finite element methods are continuously being employed for investigations in terms of feasibility and durability, by using highly advanced algorithms. In this scenario, the initial STL file of the object could be used, after some refinement, as an input for the finite element analysis as it perfectly reproduces the geometry of the devices. This approach was applied for the study of the 3D printed AFOs used in this dissertation, which is referred to the work executed (see Section 1.8) within a multidisciplinary research environment where different industrial and academic partners cooperated in order to design and manufacture a new prototype of 3D printed AFO (see Section 1.7), in substitution to the AFOs manufactured using conventional methods.

In particular, the acquisition of the initial STL files of the devices allowed the creation of four patient-specific finite element models, which were part of a standardized framework (see Chapter 4) used for the evaluation of the stiffness of the AFOs around the ankle joint and their stress distribution. The validation of the models was obtained through the outcomes obtained from a dedicated experimental setup (see Chapter 3), which confirmed the strong potential of the computational models for AFO design. Therefore, an applicable strategy was created for the optimal evaluation of the mechanical properties of the 3D printed AFOs prior to their realization in order to improve, in combination with optimization algorithms, their manufacturing process and to provide further means for facilitating their clinical prescription.

Part I of this thesis contributed to provide a general introduction on the field of application, with a brief description of the neurological and musculoskeletal disorders, such as the drop foot, which can require the utilization of AFOs for restoring a more natural gait pattern for the patients. In order to provide the proper stability, limb control and support, it is important that the AFOs are accurately manufactured for achieving the required functions without causing failure and discomfort to the patients.
These important aspects are all depending on the design and the manufacturing process of the devices: currently the most common procedure is thermoforming, which allows the creation of custom-molded thermoplastic AFOs, as described in Section 1.5. This process is time consuming and requires the ability of skilled craftsmen, which directly manufacture the devices, mostly through manual operations. Therefore, obtaining the final product requires the application of several adjustments, which do not always guarantee the control on the mechanical properties of the devices, such as thickness or stiffness. In addition, these processes do not allow the prediction of the mechanical properties of the devices before their physical realization. Therefore, the application of 3D printing technologies could be the solution for the problems encountered in the realization of these patient-specific devices; many studies already showed how the obtained performance are comparable to those of the AFOs manufactured with the traditional methods. At the same time, the use of 3D printing technologies has the potential to significantly decrease the manufacturing timelines and to improve the work efficiency. In this context a multidisciplinary research environment was created to apply the recent discoveries and developments in terms of additive manufacturing materials for the creation of a customized and usable prototype of 3D printed AFO (see Section 1.7).
This prototype should be applicable to patients of all the ages and supply significant improvements to their gait pattern, by providing a certain level of comfort and the required amount of stiffness, information prescribed by medical specialists after the gait assessment and clinical evaluation of the patient. Durability of the AFO is also an important parameter: it was estimated to be 2 years in a child and 5 years in an adult, which correspond

to 3 million of walking cycles in an adult. Therefore, the collaboration of different industrial and academic partners within the research environment allowed the creation of a different workflow where information coming from different sources, such as the gait, design, computational and experimental environment, are shared and integrated for the realization of more effective 3D printed devices.
More in detail, the AFO stiffness quantified around the ankle joint represents the main focus of this dissertation, identified within the research project and in literature as the key parameter that determines how much support the AFO is able to provide to the patients, and that might be used in the clinical setting to improve their prescription process or as an input for rigid body kinematic models to predict the impact on the patient walking pattern. Currently, the quantification of the ankle stiffness is not included in the AFO prescription process, where the devices are only defined as rigid, flexible and/or semi-rigid/flexible based on the experience of the clinical staff. By including a quantification of such a parameter will be helpful for improving the entire prescription process, which is now a trial-error process, that continues till the final configuration of the AFO is established, involving an increase of the costs and time needed.

In Chapter 2, an overview of the methods used for evaluating the performance of the AFOs described in literature is provided. A total of 46 articles was analyzed and subdivided into three classes, whether they used experimental or computational methods or a combination of both. Most of the studies regarding the experimental evaluation focused on the creation of manual and automated test rigs which allowed the assessment of the stiffness of the AFOs in the sagittal plane during the second rocker of gait, when the foot of the patient is in complete contact with the ground and the forward progression of the leg is observed. In general, a more complete approach would be reached if the AFOs were quantified in the three planes of motion (sagittal, frontal and transverse) ([94], [95], [96]), since it was identified that the ankle joint has different axes of motion (see section 1.2.2). Only a research group [75] determined the stiffness of the devices around the metatarsal-phalangeal (MTP) joint, which could be important for studying the propulsion effect of the AFO, during the push off phase of the gait (figure 1.17).
Many research studies involve the use of a surrogate limb table 2.1, since it can facilitate the fixation of the foot part of the AFO to the ground and provide the specific loading to the calf part. However, in many cases, the fixation of the AFOs was destructive ([78], [85],[86], [87],[90], [96],[97]), which made the devices not usable anymore. Two studies ([82], [93]), directly used the limb of the patients in their setups, without being functional analyses, which could be important for quantifying the impact of the human leg on

the stiffness measures.

Using a manual or an automated test rig have an impact on the final outcome: in fact, the use of a manual steering implies that many important parameters such as the speed and/or acceleration are not controllable, potentially affecting the behavior of the devices, i.e. if they are cyclically tested. Two studies ([93],[78]) tested AFOs using different speed values declaring that the stiffness of the devices was not affected, which seems unlikely due to the viscoelastic behavior of the materials employed for their realization.

Another important parameter, which was not always addressed, is the reliability of the setups, which plays a big role in the final outcome (table 2.1), especially if many partners, as in the current research environment, are required to use the setup: the test-retest repeatability, the intra-tester and inter-tester variability provide useful information to assess the validity of the obtained results. Other parameters, such as the alignment of the AFO to the anatomical ankle joint should never be neglected, as it helps to better mimic the real life conditions and to obtain reliable measures that can be used for validation purposes in the finite element environment, as done in this dissertation. Only two studies assessed the importance of the alignment: Takahashi and Stanhope [91], who evaluated how providing a load with a different orientation could influence the stiffness values and Gao et al. [83], who considered the impact of the alignment of the AFO with respect to the motor shaft.

Overall, the conduction of experimental tests on AFOs is time consuming and the construction of dedicated experimental setups is a complex and expensive operation. In their place, computational analyses could be used for the prediction of important parameters of the AFOs in a faster manner (table 2.2). The main difficulty consists in finding the appropriate boundary and loading conditions that reflect the real life situations adequately. In addition, the choice of a proper material model, that accurately describes the material used, is critical.

In general, most of the simulations in table 2.2 focused on the evaluation of the AFOs in the sagittal plane, usually providing a full constraint of the AFO sole and a load at the calf region or, vice versa, a full constraint at the calf region and a load applied at the metatarsal head region. None of the studies was representing the viscoelastic properties of the materials, which need to be considered for a full description of the material behavior, especially under cyclic loading.

Three studies ([101],[106],[107]) included a virtual representation of the patient limb in the simulations: this requires a significant increase in the modeling difficulty and the simulation time since other parameters, such as the material properties of the foot, leg, and contact properties, need to be considered. At the same time this would allow to include the forces and torques

exerted by the different parts on the AFO and study other pathologic conditions more specifically.
When talking about computational models, a mesh sensitivity analysis should always be included ([111],[119]), as it allows to assess that the obtained results are independent of the mesh size and density. Such a study was included in Chapter 4 of this dissertation in order to find the best procedure that allows to evaluate the mechanical behavior of the AFOs in a short amount of time. In order to prove they can assess reliable information, computational models need to be validated with experimental tests table 2.3; however, some of the analyzed studies require further refinements/evaluations for obtaining optimal results ([118], [119]).
Based on the analyzed studies, coupling advanced finite element models, constructed with accurate material properties and appropriate boundary/loading conditions, with experimental techniques would therefore represent the best adoptable strategy for the quantification of the AFOs mechanical properties, allowing the optimization of their manufacturing process before their physical realization, by coupling the validated finite element models with optimization algorithms, and to gain a better insight in the prescription process. All these aspects, from the experimental and computational point of view, provided the basis for the strategies adopted and described in the chapters of this dissertation.

Part II presents the design and development of the semi-automated experimental setup used for the quantification of the ankle stiffness of the 3D printed AFOs in the sagittal plane during the second rocker of gait over a maximum range of motion of +/- 25 degrees (dorsiflexion/plantarflexion). This permitted the mechanical characterization of the devices around an axis aligned to the anatomical ankle joint, which location was extracted from the gait assessment of the different patients.
This study mainly focused on 3D printed orthoses, but potentially the test rig could be applied to any topology of AFO, since the experimental setup gives the possibility to accommodate a wide range of AFOs, which are secured in the test rig using a patient-specific leg model, made in MDF. The MDF leg model contains the location of the anatomical points defining the ankle flexion/extension axis used in the gait analysis (see Paragraph 3.2) and the rig applies moments around it to derive the AFO stiffness. The definition of the ankle flexion/extension axis and the relative anatomical points are derived from the kinematic model of the lower limb initially developed by Davis et al. [120], which is widely used for the gait analysis of cerebral palsy patients who represent a large group of AFO users. This model takes a macroscopic approach to modelling the lower limb which has limitations anatomically but remains valuable from a clinical perspective of measuring gait abnormalities and treatment planning/monitoring. The approach taken here was to adopt

the axes of this 3D model in AFO definition, design and mechanical testing so to enable the clinicians, orthotists and design engineers to be able to discuss and understand the same expression/description of 3D movement.
Assessing the reliability of the setup under several working conditions (test-retest repeatability, intra-tester and inter-tester variability plus the comparison with the results coming from a second experimental machine) permitted to prove its applicability and validity in the current work and for future purposes, since other partners within the research environment are required to use it. Therefore the experimental setup, described in Chapter 3, allows to obtain reliable measures of the AFO stiffness around the ankle joint in the sagittal plane and in a non-destructive manner; this setup will be further expanded in order to obtain a full characterization of the ankle mechanical properties of the AFOs in the three planes of motion (frontal, sagittal and transverse planes) plus around the MTP joint, which can permit to better study the impact of the neutral angle on the propulsion effect of the AFOs. Therefore, it will be the first experimental setup ever produced that will allow such an AFO quantification and further details will be given later in section 5.3.
As anticipated, the AFOs were tested over specific ranges of motion, previously derived from the gait assessment of the subjects; all the stiffness plots showed the presence of hysteresis, due to the non-linear viscoelastic behavior of the material and to the friction present within the experimental setup. In contrast with other authors ([75], [76], [78], [79], [80], [81], [85], [94], [96], [93], [97], [113]) four different ankle stiffness values are considered for each zone of the angle vs. torque curve, as it can be observed that most patient-specific AFOs have a different behavior in plantarflexion compared to dorsiflexion due to their shape.

The adopted experimental approach enabled to obtain suitable measures for the comparison and relative validation of the finite element models of the AFOs, described in Part III, which are contained in a standardized framework for the evaluation of the mechanical properties of the patient-specific 3D printed AFOs in terms of ankle stiffness and stress distribution during the second rocker of the gait. The purpose of the framework is to further create a scientifically robust method to design and manufacture AFOs with specific mechanical properties in a reliable and repetitive way, applicable and extendable to several working conditions. The finite element models, therefore, can be used in combination with optimization algorithms in order to speed up the design and realization of more effective 3D printed AFOs.
Dedicated algorithms, which provide high flexibility for the mesh creation, were developed in pyFormex to convert STL files, describing the AFO geometry and used for 3D printing, into high quality finite element models. In general, they showed a good overall agreement with the experimental

data, whether the first, the second or the third approach were used (figure 4.39-figure 4.42). Four different ankle stiffness values are used for each quadrant of the angle vs. torque graph, as most of the patient-specific AFOs show a different behavior in plantarflexion compared to dorsiflexion, due to their shape. The magnitude of these stiffness values is in line with the results obtained from other research groups ([113], [58]), which have also investigated 3D printed AFOs. The visual agreement is confirmed by the calculation of the error percentages (table 4.11, table 4.13, table 4.16), which show the ability of the FE models to predict the AFOs mechanical behavior. This was achievable through the utilization of an advanced material model, the PRF model, for describing the properties of PA 12, which was never used before in literature for the 3D printed AFOs, in combination with the boundary conditions used in the experimental setup, expressed by three different approaches, in order to mimic as closely and efficiently as possible the behavior of the 3D printed AFOs. In the first approach a total encastre of the AFO geometry was applied as the height of the MDF blocks employed in the experimental tests, in the second approach a the total fixation of the AFO soles was applied with the direct inclusion of a virtual representation of the MDF blocks, while in the third approach the same boundary conditions of the second approach were used, but without including the virtual MDF blocks. The best adoptable approach in terms of computational efficiency could be considered the first one, as good percentage errors between the simulation and experimental results were obtained in a reduced amount of time. The second approach also provided good results, but the inclusion of the virtual MDF blocks significantly increased the simulation time. The third approach, instead, showed high percentage errors for the AFO A, which was the only AFO that included a high MDF block. Concerning the simulation time, it would eventually increase if 3D solid elements would be used for the realization of the meshes of the devices, as highlighted from the results of the mesh sensitivity analysis shown in table 4.8, table 4.9. For the same reasons, quadratic elements were excluded from the analysis, since they would have a huge impact on the time efficiency.

5.2 LIMITATIONS

The combination of finite element methods with experimental techniques presented in this thesis allowed the creation of a computational framework for the mechanical evaluation of patient-specific 3D printed AFOs. This framework offers a methodology, which could be extended to the evaluation of the AFOs under other working conditions, for example for the simulation of other pathologic conditions or over higher ranges of motion.

Some limitations were present in the study: because of the available instrumentation, the experimental setup could only perform tests on the AFOs at a speed of 1 °/s. Although this enabled to neglect the inertial effects acting on the AFOs, using higher velocities close to those seen during gait, might result in a better representation of the behavior of the devices. In the gait lab, in fact, patients also reach speeds in the range of 50 °/s – 100 °/s. However, by visualizing the results of tensile tests (figure 4.43), carried out from samples of PA 12 and used to derive the parameters of the material computational model [67], some assumptions can be taken.

From these outcomes, it's noticeable how increasing the testing speed from 5 mm/min to 500 mm/min resulted in an increase of the Young's modulus of about 8 %. This consideration can be assumed, as first approximation, to be similar to an increase of the AFO testing speed from 1 °/s to 100 °/s, which by considering for example an AFO with a stiffness value of 3 Nm/°, would imply an increase in stiffness of 0.24 Nm/°. This small contribution can therefore be taken into account when the AFO stiffness would be prescribed for the patients during the clinical assessment, as not a single value but a range of stiffness values would be indicated, since the patients use adaptive movement strategies to the AFO usage [64].

As explained in Chapter 3, the fixation of the devices to the experimental setup was directly performed through the use of MDF blocks, which were initially used for the realization of the AFOs. However, during the experimental tests it was experienced that they were not always perfectly matching with their specific AFOs and some manual refinement was needed. In addition, since the MDF blocks have stiffer properties, in comparison to the human leg, which possesses viscoelastic properties, it might result in higher contact forces between the AFOs and the blocks. Therefore, the development of a surrogate limb system with properties closer to the reality would be desirable.

A representation of the patient leg was also not included in the computational environment: including such a virtual part would imply to highly increase the complexity of the model since the material and contact properties for each component of the leg would need to be specified, decreasing the time efficiency. On the other side, this would have allowed to quantify the impact of the contact between the AFO and the leg on the stiffness measures and better mimic the situation experienced by the patients in reality; although this falls out of the scope of the current study, these aspects will be taken into account for future analyses.

In general, the experimental curves shown in this thesis were averaged over cycles and because of the Mullins effect, which causes the softening of the AFOs, the first cycle is always excluded from further use, since it shows different properties than the other cycles. This was decided due to the fact that the AFOs are tested in the setup over several cycles and, also in the reality, they should be ideally employed for millions of cycles. Eventually, the mathematical formulation of the PRF material model used to virtually predict the behavior of the AFOs, would permit to include the parameters that describe the Mullins effect, but they were not considered.

A limitation of the PRF model was that it allowed to perform static simulations, but, since it doesn't own parameters that describe the stiffness degradation over time, it was not appropriate for predicting the failure of the devices due to fatigue; however, the information coming from these analyses can be used for identifying the zones with the highest stresses acting on the devices; if these values are distributed over the geometry and higher than 25 MPa (stress limit identified within the project framework by tests on samples of PA 12), a fatigue failure of the devices might be expected and should be taken into account as a threshold value during the design process of the devices.

Common damping and friction coefficients for all the patient-specific AFOs allowed to have a standardized and calibrated framework, where prediction is only depending on the shape and geometry of the devices: while the damping is an artificial coefficient, used to represent the action of the straps at the calf region when the angle rotation is equal to zero, friction was chosen by curve fitting; ideally, experimental tests should be performed to measure the friction for every AFO but this will decrease the applicability and extension of the method to other AFOs.

Hysteresis was noticed in all the obtained experimental curves, which may lead to an overestimation of the measured AFO stiffness in the unloading phases, especially if high ranges of motion are used. Therefore, modifications will be implemented in the new version of the experimental setup to lower this contribution, for example by modifying the clamping system and/or by improving the lubrication of the different components within the setup for allowing smoother movements. On the computational side, hysteresis could be better represented if the influence of other components, i.e. the straps of the AFOs, would be included, but, at the same time, this would provoke the increase of the complexity of the model strategy and the decrease of the simulation time efficiency.

Concerning the inter-tester repeatability of the experimental tests, it was assessed by using two operators: this might be considered as a limitation and therefore, a bigger number of operators will be included for performing the same analysis on the new version of the experimental setup.

Another aspect, which was not assessed in the experimental setting, was the effect of temperature: a study from Cano et al. [129] highlighted how the Young's modulus of PA 12 considerably decreases when increasing the temperature at which the samples of the material are tested (-50 °C, 23 °C and 50 °C). This is caused by the approaching to the glass transition temperature of the material (Tg = 55 °C), which has an influence on its properties. Therefore, in order to assess this effect on the AFOs, a dummy leg where the temperature on the AFOs is monitored should be incorporated, as high temperatures can be reached during walking or other activities of the patients.

5.3 FUTURE DEVELOPMENTS

5.3.1 Experimental methods

The core of this study was the creation of a numerical framework for the assessment of the mechanical properties of the patient-specific 3D printed AFOs in the sagittal plane during the second rocker of the gait. In order to obtain a more complete overview of their behavior, as highlighted in the literature review contained in Chapter 2, further steps are already in process. In fact, the experimental setup is undergoing several extensions, which include the possibility of testing the devices around other axes of motion, such as the frontal and the transversal planes, as it was seen in literature that considering the ankle joint as an hinge represents an oversimplification ([6]). In addition, the performance of the AFOs around the MTP joint will be also quantified, which can help to better study the contribution of the devices in terms of propulsion during the push-off phase of the gait.
More in detail, through the collaboration with the gait lab partner, it was possible to establish the ranges of motion to be represented in the setup: in the frontal and transverse planes a rotation around the ankle joint of -15/15 degrees is considered, while, a flexion of 30 degrees is applied around the MTP joint, plus the rotation around the ankle joint in the sagittal plane, as the previous version of the test rig. This results in the creation of a new testing machine, containing features and allowing possibilities that were never permitted by only one testing rig previously built or reported in literature.
In figure 5.1 the detailed design of the new version of the experimental setup is presented. It is currently being built at V!GO NV, one of the industrial partners involved in the project (see paragraph 1.7.1), and no verification or validation has already been done.

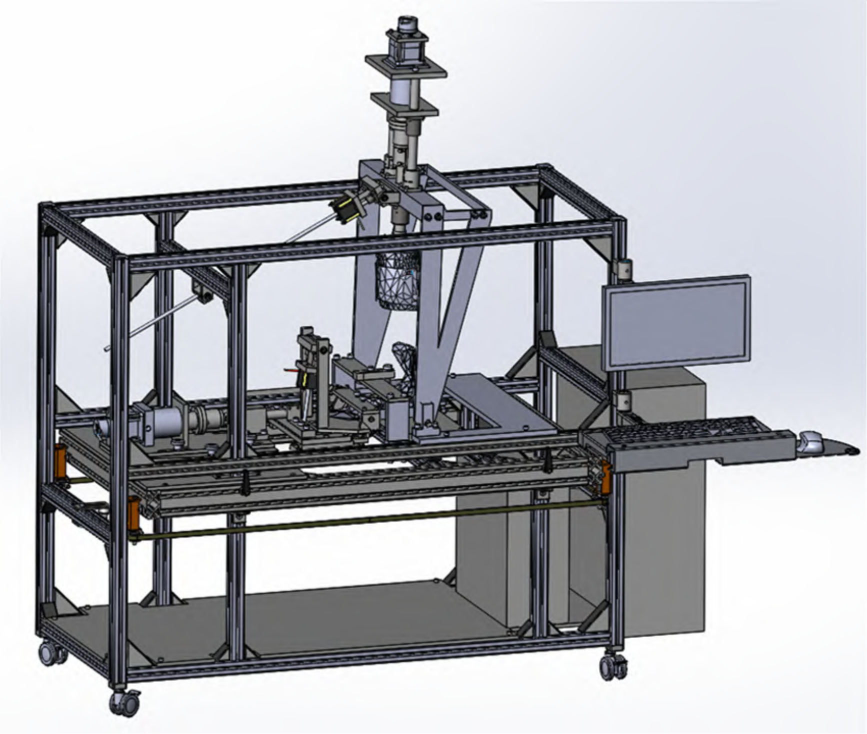

Figure 5.1: Detailed design of the new expanded experimental setup, which will allow to test the 3D printed AFOs around several axes of motion.

It represents a transportable platform, which allows the acquisition of more information about the mechanical behavior of the devices, with the possibility of reproducing more movements at the same time. This will surely permit to better mimic the conditions of the patients walking in the reality. Through this design, a new fixation system will be also included for the AFOs, since they would need to be clamped in proximity of the MTP joint too; further actions are also being taken for reducing the friction effects seen in the previous version. At the same time, the extension of the experimental setup includes a new electrical equipment for recording the angle vs. torque curves around the different axes of motion, which might help to reach values of speed as seen in the reality.
After the implementation of these new components, further design actions might also be applied in order to simulate all the three phases of the gait.
Always on the experimental side, other steps could also be taken: for example, when the test rig was initially designed, it included the possibility of testing the impact of the shoe together with the AFO; although it was not done during this work, it could be interesting to quantify if they influence the mechanical properties of the devices.

Moreover, the effect of the viscoelastic properties of the human leg and temperature on the stiffness measures could also be evaluated: in the reality the AFOs stay continuously in contact with the leg of the patients, which might affect their behavior, during the several motion activities. A new surrogate limb system, that incorporates viscoelastic properties as the human leg and allows the temperature analysis, could be developed and used to quantify the AFOs properties in the future.

5.3.2 Computational methods

From the computational point of view, the expansion of the experimental setup to the other axes of motion will provide further data usable for the validation of new finite element models that will be created for accurately replicating the new working conditions. An example of this can be seen in figure 5.2, where the movement of a 3D printed AFO around the anatomical MTP joint is imposed. The next step would also be to investigate other pathologic situations i.e. by including the pressure generated by the patients during the gait assessments for studying their impact on the devices in terms of stress/strain and stiffness.

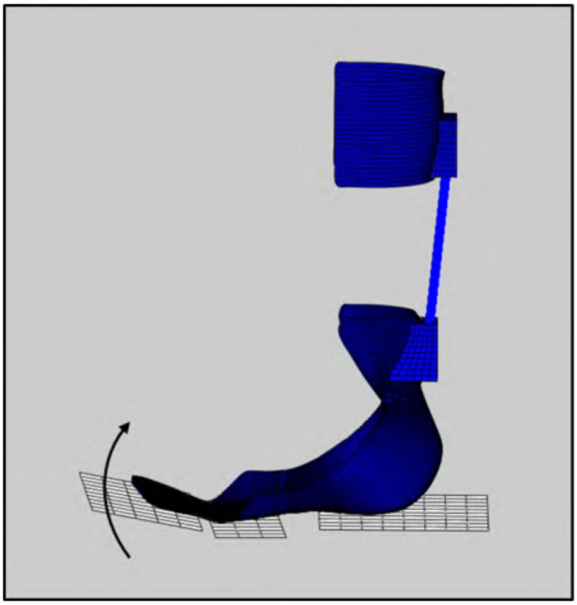

Figure 5.2: Virtual representation of a modular 3D printed AFO when a rotation around the MTP joint is imposed.

In addition, a detailed model of the entire leg system could also be included with specific material properties for muscles, skin, ligaments and tendons, or a more simplified model with viscoelastic properties that could resemble the human leg. This might result in a better representation of the reality, where the forces directly generated by the different components would be included or the contact between the AFO and the human leg is represented, in order to permit an optimal comparison with the data coming from the gait analysis. In particular, it would allow to model the AFOs with different local values of thickness, thus to improve the comfort felt by the patients. In figure 5.3 it is possible to see an example of this virtual representation.

Figure 5.3: Virtual representation of a modular 3D printed AFO together with an entire leg.

5.4 CONCLUSIONS

This PhD project presented the creation of a novel numerical framework where the combination of experimental and computational methods allowed the mechanical evaluation of several patient-specific 3D printed ankle foot orthoses in the sagittal plane during the second rocker of the gait. The experimental methods required the construction of a semi-automated experimental setup, which permitted the quantification of the stiffness of the 3D printed devices around an axis aligned to the anatomical ankle joint over a patient-specific range of motion; the location of the anatomical ankle joint and the different ranges of motion were directly obtained from the gait assessment of the patients. The experimental boundary and loading conditions were then replicated in the finite element environment where the different patient-specific models were validated.

The results obtained in this PhD project have contributed to increase the general understanding of the mechanical behavior of the 3D printed AFOs and showed the big potential of the finite element models; they could be extended to the analysis of other different pathologic conditions of the patients and at the same time be applied to the prediction of the behavior of the devices before their physical realization, in order to optimize their manufacturing process and clinical application. The numerical framework, in fact, is meant to be used in combination with optimization algorithms for allowing, together with the inputs coming from the gait lab environment, to design and develop more effective 3D printed AFOs.

BIBLIOGRAPHY

[1] C. VanPutte, J. Reagan and A. Russo, 'Seeley's essentials of anatomy and physiology, 9th edition.', M. H. Education., Ed., pp. 57–78, 2015.

[2] J. Loudon, 'Biomechanics and pathomechanics of the patellofemoral joint.' *Int J Sports Phys Ther*, vol. 11(6), pp. 820–830, 2016.

[3] C. Brocket and G. Chapman, 'Biomechanics of the ankle.' *Orthopaedics and Traum*, vol. 30(3), pp. 232–238, 2016.

[4] P. Golano, M. Dalmau-Pastor, J. Vega and J. Batista, 'Anatomy of the ankle', *Journal of Engineering in Medicine*, Jan.2014.

[5] J. Michael, A. Golshani, S. Gargac and T. Goswami, 'Biomechanics of the ankle joint and clinical outcomes of total ankle replacement', *Journal of the mechanical behavior of biomedical materials I*, vol. 1(4), pp. 276–94, Oct. 2008.

[6] A. Leardini, J. O'Connor and S. Giannini, 'Biomechanics of the natural, arthritic, and replaced human ankle joint', *J Foot Ankle Res*, vol. 7:8, 2014.

[7] K. Young, J. Wise, P. DeSaix, D. Kruse, B. Poe, E. Johnson, J. Johnson, O. Korol, J. Betts and M. Womble, 'Anatomy physiology', Jan. 2013.

[8] A. Kelikian, 'Sarrafian's anatomy of the foot and ankle: Descriptive, topographical, functional, 3rd edition.', W. Kluwer, Ed., Jun. 2011.

[9] A. Leardini, J. O'Connor, F. Catani and S. Giannini, 'Kinematics of the human ankle complex in passive flexion: A single degree of freedom system.' *J Biomech*, vol. 32, pp. 111–118, 1999.

[10] A. Leardini, R. Stagni and J. O'Connor, 'Mobility of the subtalar joint in the intact ankle complex.' *J Biomech*, vol. 34(6), pp. 805–809, 2001.

[11] F. Corazza, R. Stagni, V. Parenti-Castelli and A. Leardini, 'Articular contact at the tibiotalar joint in passive flexion.' *J Biomech*, vol. 38(6), pp. 1205–1212, 2005.

[12] R. Stagni, A. Leardini and A. Ensini, 'Ligament fibre recruitment at the human ankle joint complex in passive flexion.' *J Biomech*, vol. 37(12), pp. 1823–1829, 2004.

[13] R. Mann, 'Biomechanics of the foot.' *In: Atlas of Orthotics, American Academy of Orthopaedic Suergons. C.V. Mosby Company, St.Louis, Missouri*, pp. 112–125, 1985.

[14] R. Morrissy, 'Dynamics of the foot and gait, 3rd edition', *In: Lovell and Winter's Pediatric Orthopedics, vol. 1. Lippincott, Philadelphia*, vol. 1, 1990.

[15] S. Standring, 'Gray's anatomy: The anatomical basis of clinical practice, 41st edition', Elsevier, Ed., 2016.

[16] A. Lundberg, O. Svensson, G. Nemeth and al., 'The axis of rotation of the ankle joint', *J Bone Joint Surg Br*, vol. 71(1):94, 1989.

[17] C. Barnett and J. Napier, 'The axis of rotation at the ankle joint in man: Its influence upon the form of the talus and the mobility of the fibula', *Journal of Anatomy*, vol. 86, pp. 1–9, 1952.

[18] J. Hicks, 'The mechanics of the foot', *Journal of Anatomy*, vol. 87(4), pp. 345–357, 1953.

[19] S. Grimston, B. Nigg, D. Hanley and J. Engsberg, 'Differences in ankle joint complex range of motion as a function of age', *Foot Ankle Int*, vol. 14(4), pp. 215–22, 1993.

[20] R. Stauffer, E. Chao and R. Brewster, 'Force and motion analysis of the normal, diseased and prosthetic ankle joint', *Clin Orthop*, 127:189, 1977.

[21] V. Valderrabano, B. Hintermann, M. Horisberger and T. Fung, 'Ligamentous posttraumatic ankle osteoarthritis', *Am J Sports Med*, vol. 34(4), pp. 612–20, 2006.

[22] J. Close, 'Some applications of the functional anatomy of the ankle joint', *J Bone Joint Surg Am*, vol. 38-A(4), pp. 761–81, 1956.

[23] J. Close and V. Inman, 'The action of the ankle joint. report to the advisory committee on artificial limbs, national research council', *Berkeley, CA: Prosthetic Devices Research Project, Institute of Engineering Research, University of California*, vol. Serie II, No.22, 1951.

[24] A. Lundberg, I. Goldie, B. Kalin and al., 'Kinematics of the ankle/foot complex. plantar flexion and dorsi-flexion', *Foot Ankle*, vol. 9(4):194, 1989.

[25] J. Rose and J. Gamble, 'Human walking, 3rd edition', P. : L. W. Wilkins, Ed., 2006.

[26] M. Nordin and V. Frankel, 'Basic biomechanics of the musculoskeletal system, 3rd edition.', L. W. Wilkins, Ed., 2001.

[27] Z. Abu-Faraj, G. Harris, P. Smith and S. Hassani, 'Human gait and clinical movement analysis', *Wiley Encyclopedia of Electrical and Electronics Engineering, 2nd Edition. John Wiley Sons, Inc.*, 2015.

[28] F. Stevens, N. Weerkamp and J. Cals, 'Foot drop', *BMJ*, vol. 8, pp. 158–169, 2015.

[29] J. Burridge, D. Wood, P. Taylor and D. McLellan, 'Indices to describe different muscle activation patterns, identified during treadmill walking, in people with spastic drop-foot', *Med Eng Phys*, vol. 23(6), pp. 427–34, 2001.

[30] J. Perry and J. Burnfield, 'Gait analysis: Normal and pathological function', *SLACK Inc.*, 1992.

[31] M. Whittle, 'Gait analysis: An introduction, 4th edition', *Elsevier*, 2007.

[32] J. Stewart, 'Foot drop: Where, why and what to do?', *Practical Neurology*, 350:h1736, 2008.

[33] S. Daniels, J. Feinberg, J. Carrino, A. Behzadi and D. Sneag, 'Mri of foot drop: How we do it', *Radiology*, vol. 289(1), pp. 9–24, 2018.

[34] K. Szigeti and J. Lupski, 'Charcot-marie-tooth disease', *Eur J Hum Genet*, vol. 17(6), pp. 703–10, 2009.

[35] A. Danielsson and K. Sunnerhagen, 'Energy expenditure in stroke subjects walking with a carbon composite ankle foot orthosis.' *J Rehabil Med*, vol. 36, pp. 165–168, 2004.

[36] R. Waters and S. Mulroy, 'The energy expenditure of normal and pathologic gait.' *Gait Posture*, vol. 8, pp. 207–231, 1999.

[37] A. Dubin, 'Gait: The role of the ankle and foot in walking', *Med Clin North Am.*, vol. 98(2), pp. 205–11, 2014.

[38] T. Kobayashi, M. Singer, M. Orendurff, F. Gao, W. Daly and K. Foreman, 'The effect of changing plantarflexion resistive moment of an articulated ankle–foot orthosis on ankle and knee joint angles and moments while walking in patients post stroke', *Clinical Biomechanics*, vol. 30(8), pp. 775–80, 2015.

[39] E. Russell Esposito, R. Blanck, N. Harper, J. Hsu and J. Wilken, 'How does ankle-foot orthosis stiffness affect gait in patients with lower limb salvage?', *Clin. Orthop. Relat. Res.*, vol. 472(10), pp. 3026–3035, 2014.

[40] A. Ries, T. Novachek and M. Schwartz, '. the efficacy of ankle-foot orthoses on improving the gait of children with diplegic cerebral palsy: A multiple outcome analysis', *PMR Journal*, vol. 7(9), pp. 922–9, 2015.

[41] E. Schrank and S. Stanhope, 'Dimensional accuracy of ankle-foot orthoses constructed by rapid customization', *J Rehabil Res Dev*, vol. 48, pp. 31–42, 2011.

[42] J. Perry, 'Gait analysis: Normal and pathological function', S. Inc., Ed., 1969.

[43] R. Ross, R. Greig and P. Convery, 'Comparison of bending stiffness of six different colours of copolymer polypropylene', *J Prosthetic Orthot Int*, vol. 23(1), pp. 63–71, Apr. 1999.

[44] D. Zou, T. He, M. Dailey, K. Smith, M. Silva, D. Sinacore, M. Mueller and M. Hastings, 'Experimental and computational analysis of composite ankle-foot orthosis', *Journal of Rehabilitation Research Development*, vol. 51(10), pp. 1525–36, 2014.

[45] S. Rethlefsen, R. Kay, S. Dennis, M. Forstein and V. Tolo, 'The effects of fixed and articulated ankle-foot orthoses on gait patterns of subjects with cerebral palsy.' *J Pediatr Orthop.*, vol. 19, pp. 470–474, 1999.

[46] C. Buckon, S. Thomas, S. Jakobson-Huston, M. Sussman and M. Aiona, 'Comparison of three ankle-foot orthosis configurations for children with spastic hemiplegia.' *Dev Med Child Neurol*, vol. 43(6), pp. 371–378, 2001.

[47] B. Balaban, E. Yasar, U. Dal, K. Yazicioglu, H. Mohur and T. Kalyon, 'The effect of hinged ankle-foot orthosis on gait and energy expenditure in spastic hemiplegic cerebral palsy.' *Disability Rehabil*, vol. 29(2), pp. 139–144, 2007.

[48] S. Radtka, S. Skinner, D. Dixon and M. Johanson, 'A comparison of gait with solid, dynamic, and no ankle-foot orthoses in children with spastic cerebral palsy.' *Phys Ther*, vol. 77(4), pp. 395–409, 1997.

[49] S. Westberry, J. Davids, J. Shaver, S. Tanner, D. Blackhurst and R. Davis, 'Impact of ankle-foot orthoses on static foot alignment in children with cerebral palsy.' *J Bone Joint Surg*, vol. 89(4), pp. 806–813, 2007.

[50] J. Deckers, M. Vermandel, R. Willemsen, J. Geldhof, E. Vasiliauskaite and F. Forward M.and Plasschaert, 'Design and clinical evaluation of additive manufactured ankle foot orthoses', *PMI 2016 conference*, pp. 72–76, 2016.

[51] B. Rogozinski, J. Davids, G. Jameson, S. Mulroy and D. Blackhurst, 'The efficacy of the floor-reaction ankle-foot orthosis in children with cerebral palsy.' *J Bone Joint Surg Am*, vol. 10, pp. 2440–7, 2009.

[52] I. American Board for Certification in Orthotics Prosthetics Pedorthics, 'Practice analysis of certified practitioners in the disciplines of orthotics and prosthetics', 2015.

[53] Y. Kerkum, A. Buizer, J. van den Noort, J. Becher, J. Harlaar and M. Brehm, 'The effects of varying ankle foot orthosis stiffness on gait in children with spastic cerebral palsy who walk with excessive knee flexion', *PLoS ONE*, vol. 10(11)), e0142878, 2015.

[54] E. Esposito, R. Blanck, N. Harper, J. Hsu and J. Wilken, 'How does ankle-foot orthosis stiffness affect gait in patients with lower limb salvage?', *Clinical Orthopaedics and Related Research*, vol. 472(10), pp. 3026–35, 2014.

[55] D. Bregman, J. Harlaar, C. Meskers and V. de Groot, 'Spring-like ankle foot orthoses reduce the energy cost of walking by taking over ankle work', *Gait Posture*, vol. 35(1), pp. 148–53, 2011.

[56] M. Alam, I. Choudhury, A. Mamat and S. Hussain, 'Computer aided design and fabrication of a custom articulated ankle foot orthosis', *Journal of Mechanics in Medicine and Biology*, vol. 15(4), p. 1 550 058, 2015.

[57] C. Mavroidis, R. Ranky, M. Sivak, B. Patritti, J. DiPisa, A. Caddle, K. Gilhooly, L. Govoni, S. Sivak, M. Lancia, R. Drillio and P. Bonato, 'Patient specific ankle-foot orthoses using rapid prototyping', *Journal of Neuro Engineering and Rehabilitation*, vol. 8:1, 2011.

[58] H. Choi, K. Peters, M. MacConnel, K. Ly, E. Eckert and K. Steele, 'Impact of ankle foot orthosis stiffness on achilles tendon and gastrocnemius function during unimpaired gait', *J Biomech*, vol. 64, pp. 145–152, 2017.

[59] S. Telfer, J. Pallari, J. Munguia, K. Dalgarno, M. McGeough and J. Woodburn, 'Embracing additive manufacture: Implications for foot and ankle orthosis design', *BMC Musculoskelet Disord*, vol. 13(1), p. 84, 2012.

[60] Y. Cha, K. Lee, H. Ryu, I. Joo, A. Seo, D. Kim and S. Kim, 'Ankle-foot orthosis made by 3d printing technique and automated design software', *Applied Bionics and Biomechanics*, 2017.

[61] V. Creylman, L. Muraru, J. Pallari, H. Vertommen and L. Peeraer, 'Gait assessment during the initial fitting of customized selective laser sintering ankle foot orthoses in subjects with drop foot', *Prosthetics and Orthotics International*, vol. 37(2), pp. 132–38, 2013.

[62] N. Harper, E. Russell, J. Wilken and R. Neptune, ‘Selective laser sintered versus carbon fiber passive-dynamic ankle-foot orthoses: A comparison of patient walking performance’, *Journal of Biomechanical Engineering*, vol. 136(9), 091001 (A), 2014.

[63] ——, ‘The influence of ankle-foot orthosis stiffness on walking performance in individuals with lower-limb impairments’, *Clinical Biomechanics*, vol. 29(8), 877–84 (B), 2014.

[64] E. Arch and S. Stanhope, ‘Passive-dynamic ankle–foot orthoses substitute for ankle strength while causing adaptive gait strategies: A feasibility study’, *Annals of Biomedical Engineering*, vol. 43(2), pp. 442–50, 2014.

[65] I. Gibson, D. Rosen and B. Stucker, ‘Additive manufacturing technologies: 3d printing, rapid prototyping and direct digital manufacturing, 2nd edition’, Springer, Ed., 2015.

[66] N. Hopkinson, R. Hague and P. Dickens, ‘Rapid manufacturing: An industrial revolution for the digital age’, J. W. Sons, Ed., 2006.

[67] N. Lammens, M. Kerseman, I. De Baere and W. Van Paepegem, ‘On the visco-elasto-plastic response of additively manufactured polyamide-12 (pa-12) through selective laser sintering’, *Polymer Testing*, vol. 57, pp. 149–55, 2017.

[68] T. Starr, T. Gornet and J. Usher, ‘The effect of process conditions on mechanical properties of laser-sintered nylon’, *Rapid Prototyping Journal*, vol. 17(6), pp. 418–23, 2011.

[69] B. Caulfield, P. McHugh and S. Lohfeld, ‘Dependence of mechanical properties of polyamide components on build parameters in the sls process’, *Journal of Materials Processing Technology*, vol. 182(1-3), pp. 477–88, 2007.

[70] U. Ajoku, N. Saleh, N. Hopkinson, R. Hague and P. Erasenthiran, ‘Investigating mechanical anisotropy and end-of-vector effect in laser-sintered nylon parts’, *Proceedings of the Institution of Mechanical Engineers Part B-Journal of Engineering Manufacture*, vol. 220(7), pp. 1077–86, 2006.

[71] W. Cooke, R. Tomlinson, R. Burguete, D. Johns and G. Vanard, ‘Anisotropy, homogeneity and ageing in an sls polymer’, *Rapid Prototyping Journal*, vol. 17(4), pp. 269–79, 2011.

[72] A. Salazar, A. Rico, J. Rodriguez and F. Martin de la Escaler Cutilla, ‘Monotonic loading and fatigue response of a bio-based polyamide pa11 and a petrol-based polyamide pa12 manufactured by selective laser sintering’, *European Polymer Journal*, vol. 59, pp. 36–45, 2014.

[73] B. Van Hooreweder, D. Moens, R. Boonen and P. Sas, 'On the difference in material structure and fatigue properties of nylon specimens produced by injection molding and selective laser sintering', *Polymer Testing*, vol. 32(5), pp. 972–81, 2013.

[74] J. Munguia and K. Dalgarno, 'Fatigue behaviour of laser-sintered pa12 specimens under four-point rotating bending', *Rapid Prototyping Journal*, vol. 20(4), pp. 291–300, 2014.

[75] D. Bregman, A. Rozumalski, D. Koops, V. Groot, M. Schwartz and J. Harlaar, 'A new method for evaluating ankle foot orthosis characteristics: Bruce', *Gait Posture*, vol. 30(2), pp. 144–149, 2009.

[76] P. Cappa, F. Patane and M. Piero, 'A novel device to evaluate the stiffness of ankle foot orthosis devices', *J Biomech Eng*, vol. 125, pp. 913–7, 2003.

[77] T. Kobayashi, A. Leung and S. Hutchins, 'Techniques to measure rigidity of ankle-foot orthoses: A review', *J Rehabil Res Dev*, vol. 48, pp. 565–576, 2011.

[78] T. Novacheck, C. Beattie, A. Rozumalski, G. Gent and G. Kroll, 'Quantifying the spring-like properties of ankle-foot orthoses (afos)', *Prosthet Orthot Int*, vol. 19, pp. 98–103, 2007.

[79] K. Katdare, 'The non-linear stiffness of ankle-foot orthoses: Measurement and prediction [dissertation]', *Minneapolis: The Biomedical Engineering Graduate Program, University of Minnesota*, 1999.

[80] M. Nagaya, 'Shoehorn-type ankle-foot orthoses: Prediction of flexibility.' *Arch Phys Med Rehabil.*, vol. 78(1), pp. 82–84, 1997.

[81] T. Kobayashi, A. Leung, Y. Akazawa, H. Naito, M. Tanaka and S. Hutchins, 'Design of an automated device to measure sagittal plane stiffness of an articulated ankle-foot orthosis', *Prosthet Orthot Int*, vol. 34, pp. 439–448, 2010.

[82] T. Kobayashi, A. Leung and S. Hutchins, 'Design of a manual device to measure ankle joint stiffness and range of motion', *Prosthet Orthot Int*, vol. 35(4), pp. 478–481, 2011.

[83] F. Gao, W. Carlton and S. Kapp, 'Effects of joint alignment and type on mechanical properties of thermoplastic articulated afo', *Prosthet Orthot Int*, vol. 35, pp. 181–189, 2011.

[84] R. Singerman, D. Hoy and J. Mansour, 'Design changes in ankle-foot orthoses intended to alter stiffness also alter orthosis kinematics', *J Prosthet Orthot*, vol. 11(3), pp. 48–55, 1999.

[85] T. Sumiya, Y. Suzuki and T. Kasahara, 'Stiffness control in posterior-type plastic ankle-foot orthoses: Effect of ankle trimline. part 1: A device for measuring ankle moment', *Prosthet Orthot Int*, vol. 20(2), pp. 129–31, 1996.

[86] ——, 'Stiffness control in posterior-type plastic ankle-foot orthoses: Effect of ankle trimline. part 2: Orthosis characteristics and orthosis/patient matching', *Prosthet Orthot Int*, vol. 20(2), pp. 132–37, 1996.

[87] W. DeToro, 'Plantarflexion resistance of selected ankle-foot orthoses: A pilot study of commonly prescribed prefabricated and custom-molded alternatives', *J Prosthet Orthot*, vol. 13(2), pp. 39–44, 2001.

[88] Y. Lee, K. Choi, K. Cho, Y. Choi, H. Lim and B. Kim, 'Plastic ankle foot orthosis for hemiplegics and structural analysis', *Key Engineering Materials*, 326-328:855-858, 2006.

[89] T. Lunsford, T. Ramm and J. Miller, 'Viscoelastic properties of plastic afos', *J Prosthet Orthot*, vol. 6(1), pp. 3–9, 1994.

[90] R. Major, P. Hewart and A. MacDonald, 'A new structural concept in moulded fixed ankle foot orthoses and comparison of the bending stiffness of four constructions', *Prosthet Orthot Int*, vol. 28(1), pp. 44–48, 2003.

[91] K. Takahashi and S. Stanhope, 'Estimates of stiffness for ankle-foot orthoses are sensitive to loading conditions', *J Prosthet Orthot*, vol. 22(4), pp. 211–219, 2010.

[92] S. Ringleb, T. Armstrong, L. Berglund, H. Kitaoka and K. Kaufman, 'Stiffness of the arizona ankle-foot orthosis before and after modification for gait analysis', *J Prosthet Orthot*, vol. 21(4), pp. 204–7, 2009.

[93] S. Yamamoto, M. Ebina, M. Iwasaki, S. Kubo, H. Kawai and T. Hayashi, 'Comparative study of mechanical characteristics of plastic afos', *J Prosthet Orthot*, vol. 5(2), pp. 59–64, 1993.

[94] P. Cappa, F. Patane and R. Di, 'A continuous loading apparatus for measuring three dimensional stiffness of ankle-foot orthoses', *J Biomech Eng*, vol. 127, pp. 1025–9, 2005.

[95] S. Bielby, T. Warrick, D. Benson, R. Brooks, E. Skewes and E. Alvarez, 'Trimline severity significantly affects rotational stiffness of ankle-foot orthosis', *J Prosthet Orthot*, vol. 22(4), p. 204, 2010.

[96] B. Klasson, P. Convery and S. Raschke, 'Test apparatus for the measurement of the flexibility of ankle-foot orthoses in planes other than the loaded plane', *Prosthet Orthot Int*, vol. 22(1), pp. 45–53, 1998.

[97] A. Polliack, C. Swanson, S. Landsberger and D. McNea, 'Development of a testing apparatus for structural stiffness evaluation of ankle-foot orthoses', *JPO*, vol. 13(3), pp. 74–82, 2001.

[98] H. Lai, C. Yu, H. Kao, W. Chen, C. Chou and C. Cheng, 'Ankle-foot simulator development for testing ankle-foot orthoses', *Medical Engineering Physics*, vol. 32, pp. 623–629, 2010.

[99] C. Sheehan and E. Figgins, 'A comparison of mechanical properties between different percentage layups of a single-style carbon fibre ankle oot orthosis', *Prosthet Orthot Int*, vol. 41(4), pp. 364–372, 2016.

[100] T. Chu and R. Feng, 'Determination of stress distribution in various ankle-foot orthoses: Experimental stress analysis', *J Prosthet Orthot*, vol. 10(1), pp. 11–16, 1998.

[101] T. Chu and N. Reddy, 'Stress distribution in the ankle-foot orthosis used to correct pathological gait', *Journal of Rehabilitation Research Development*, vol. 32(4), pp. 349–60, 1995.

[102] E. Papi, J. Maclean, R. Bowers and S. Solomonidis, 'Determination of loads carried by polypropylene ankle-foot orthoses: A preliminary study', *Proc Inst Mech Eng H*, vol. 229), pp. 40–51, 2015.

[103] G. Tanino, Y. Tomita and S. Mizuno, 'Development of an ankle torque measurement system for measuring ankle torque during walking', *J Phys Ther Sci*, vol. 27(5), pp. 1477–1480, 2015.

[104] M. Nowak, K. Abu-Hasaballah and P. Cooper, 'Design enhancement of a solid ankle-foot orthosis: Real-time contact pressures evaluation', *J Rehabil Res Dev*, vol. 37, pp. 272–281, 2000.

[105] G. Gomes and al., 'Structural reinforcements on afo's: A study using computer-aided design and finite element method', *IEEE 5th Portuguese Meeting on Bioengineering (ENBENG)*, pp. 1–4, 2017.

[106] N. Jamshidi, H. Hanife, M. Rostami, S. Najarian, M. Menhaj, M. Saadatnia and F. Salami, 'Modelling the interaction of ankle-foot orthosis and foot by finite element methods to design an optimized sole in steppage gait', *Journal of Medical Engineering Technology*, vol. 34(2), pp. 116–23, 2010.

[107] R. Uning, N. Abu Osman and R. Abdul Rahim, '3d finite element analysis of ankle-foot orthosis on patients with unilateral foot drop: A preliminary study', *In: 4th Kuala Lumpur international conference on biomedical engineering, Malaysia, IFMBE proceedings. Berlin: Springer*, vol. 21, pp. 366–369, 2008.

[108] M. Badescu, C. Purcar and D. Badescu, 'Ankle foot orthoses with wire insertions', *Applied Mechanics and Materials*, vol. 371, pp. 554–558, 2013.

[109] Y. Lee, Y. Choi, H. Kim, H. Lee and L. Cho, 'A study on the structural stress analysis of plastic ankle foot orthosis (afo) under dorsiflexion and plantarflexion conditions', *International Journal of Modern Physics*, vol. B, pp. 204 559–64, 2006.

[110] S. Syngellakis, M. Arnold and H. Rassoulian, 'Assessment of non-linear behavior of plastic ankle foot orthoses by the finite element method', *Proceedings of the Institution of Mechanical Engineers - Part H*, vol. 214(5), pp. 527–39, 2000.

[111] S. Syngellakis and M. Arnold, 'Modelling considerations in finite element analyses of ankle foot orthoses', *WIT Transactions on Ecology and the Environment*, vol. 160, pp. 183–194, 2012.

[112] M. Faustini, R. Neptune, R. Crawford and S. Stanhope, 'Manufacture of passive dynamic ankle–foot orthoses using selective laser sintering', *IEEE TRANSACTIONS ON BIOMEDICAL ENGINEERING 2008*, vol. 55(2), pp. 784–90, 2008.

[113] E. Schrank, L. Hitch, K. Wallace, R. Moore and S. Stanhope, 'Assessment of a virtual functional prototyping process for the rapid manufacture of passive-dynamic ankle-foot orthoses', *J Biomech Eng*, vol. 135(10), pp. 101 011–7, 2013.

[114] R. Chen, L. Chen, B. Tai, Y. Wang, A. Shih and J. Wensman, 'Additive manufacturing of personalized ankle-foot orthosis', *Proceedings of NAMRI/SME*, vol. 42, pp. 381–389, 2009.

[115] G. Bellavita, M. Cocconcelli, D. Castagnetti and R. Rubini, 'Development and validation of a numerical model for the optimization of a brace for lower limb', *In: Silva L. (EDS) Materials Design and Applications. Advanced Structured Materials; Springer*, vol. 65, pp. 144–149, 2009.

[116] K. Krukonis, K. Daunoravičienė, J. Griskevicius and A. Kilikevičius, 'Method for ankle foot orthotics' mechanical assessment: A pilot study', *MECHANIKA*, vol. 23(5), pp. 723–727, 2017.

[117] B. Stier, J. Simon and S. Reese, 'Numerical and experimental investigation of the structural behavior of a carbon fiber reinforced ankle-foot orthosis', *Medical Engineering Physics*, vol. 37(5), pp. 505–11, 2015.

[118] D. Leone, S. Diemente and M. Lopez-Isa, 'Structural stability prediction for thermoplastic ankle-foot orthoses', *Proceedings of the 1991 IEEE 17th Annual Northeast Bioengineering Conference*, vol. 1991231-2, 1991.

[119] A. Amerinatanzi, H. Zamanian, N. Moghaddam, H. Ibrahim, M. Hefzy and M. Elahinia, ‘On the advantages of superelastic niti in ankle foot orthoses’, *In Proceedings of the ASME 2016 SMASIS2016, Stowe, VT, USA*, 2016.

[120] R. Davis, S. Õunpuu, D. Tyburski and J. Gage, ‘A gait analysis data collection and reduction technique’, *Human Movement Science*, vol. 10(5), pp. 575–587, 1991.

[121] N. Özkaya and M. Nordin, ‘Fundamentals of biomechanics: Equilibrium, motion, and deformation.’, N. Y. Springer, Ed., 1999.

[122] S. Cantournet, R. Desmorat and J. Besson, ‘Mullins effect and cyclic stress softening of filled elastomers by internal sliding and friction thermodynamics model’, *International Journal of Solids and Structures*, vol. 46(11-12), pp. 2255–2264, 2009.

[123] T. Koo and M. Li, ‘A guideline of selecting and reporting intraclass correlation coefficients for reliability research’, *Journal of Chiropractic Medicine*, vol. 15(2), pp. 155–163, 2016.

[124] M. Roebroeck, J. Harlaar and G. Lankhorst, ‘The application of generalizability theory to reliability assessment: An illustration using isometric force measurements.’ *Phys Ther*, vol. 73, pp. 386–95, 1993.

[125] Simulia, *Abaqus documentation 6.14*, Online multimedia.

[126] J. Hurtado, I. Lapczyk and S. Govindarajan, ‘Parallel rheological framework to model non-linear viscoelasticity, permanent set and mullins effect in elastomers’, *Constitutive Models for Rubber VIII*, vol. 95-100, 2013.

[127] I. Lapczyk and J. Hurtado, ‘A viscoelastic-elastoplastic finite strain framework for modeling polymers’, *Proceedings of the ASME International Mechanical Engineering Congress and Exposition 2014, Montreal*, 2014.

[128] N. Lammens, ‘Optimization of optical fiber coating and interrogator geometry for embedding in composite laminates [dissertation]’, *Gent (BE): Gent University*, 2015.

[129] A. Cano, A. Salazar and J. Rodriguez, ‘Effect of temperature on the fracture behavior of polyamide 12 and glass-filled polyamide 12 processed by selective laser sintering’, *Eng Fract Mech*, vol. 203, pp. 66–80, 2018.